Robert P. Uhlig

An experimental validation of Lorentz force eddy current testing

An experimental validation of Lorentz force eddy current testing

Robert P. Uhlig

Universitätsverlag Ilmenau
2014

Impressum

Bibliografische Information der Deutschen Nationalbibliothek
Die Deutsche Nationalbibliothek verzeichnet diese Publikation in der Deutschen Nationalbibliografie; detaillierte bibliografische Angaben sind im Internet über http://dnb.d-nb.de abrufbar.

Die dieser Publikation zugrunde liegende Arbeit hat der Fakultät für Maschinenbau der Technischen Universität Ilmenau im Jahr 2013 unter dem Titel „Identification of Material Defects in Metallic Materials Using Lorentz Force Eddy Current Testing" als Dissertation vorgelegen und ist online mit der URN urn:nbn:de:gbv:ilm1-2013000023 erschienen.

Technische Universität Ilmenau/Universitätsbibliothek
Universitätsverlag Ilmenau
Postfach 10 05 65
98684 Ilmenau
www.tu-ilmenau.de/universitaetsverlag

Herstellung und Auslieferung
Verlagshaus Monsenstein und Vannerdat OHG
Am Hawerkamp 31
48155 Münster
www.mv-verlag.de

ISBN 978-3-86360-087-7 (Druckausgabe)
URN urn:nbn:de:gbv:ilm1-2014100022

Titelfoto: Veit Henkel | Fakultät für Maschinenbau, TU Ilmenau

Abstract

The adoption of metallic materials in industry and building construction is of enormous importance. A precise inspection of the used metals is necessary due to the fact that the material is often exploited to the breaking point. To make sure, that a component is without defects and will withstand the applied loads, usually a 100% check-up is performed. Therefore, several nondestructive material testing techniques are available. The applicability is often limited or expansive.

The dissertation at hand deals with the description of the nondestructive material testing technique named "Lorentz force eddy current testing" and the experimental functionality proof. The contactless measurement technique has been recently developed at the Ilmenau University of Technology and has been evolved in the framework of the Research Training Group 1567. This work summarizes the results of the basic research without the claim of direct applications in industry.

The technique "Lorentz force eddy current testing" provides deeper penetration depths due to the use of direct magnetic fields compared to classical eddy current testing under same working conditions that use alternating magnetic fields . This enables the detection of deep lying defects inside of an electrically conducting not ferromagnetic material. In the dissertation is shown how to detect defects reliable (detection), where the defect is (localization) and prepares for reconstruction techniques (inverse problem) by providing the solution of the direct problem.

To describe the direct problem it is necessary to describe the behavior of a moved solid state body in the vicinity of a direct magnetic field first. Using a conceptually simple prototype model some limits of the measurement technique are presented and the basic physical principle is explained.

In order to prove the functionality of the measurement technique experimental data for specimens with artificial defects are presented. The determination of limits and the analysis of the measurement signal of the used experimental setup are performed. Suggestions for further improvement are given.

Zusammenfassung

Der Einsatz von metallischen Werkstoffen ist in Industrie und Baugewerbe von enormer Bedeutung. Die immer stärkere Ausnutzung bis zur Grenze der Belastbarkeit eines Materials macht eine genaue Untersuchung des eingesetzten Metalls erforderlich. Um sicherzustellen, dass ein Bauteil fehlerfrei ist und den geforderten Belastungen standhalten wird, ist meist eine 100 %ige Überprüfung notwendig. Dazu steht eine Auswahl an zerstörungsfreien Werkstoffprüfverfahren zur Verfügung. Die Anwendbarkeit ist oft begrenzt oder kostspielig.

Die vorliegende Dissertation befasst sich mit der Beschreibung des zerstörungsfreien Werkstoffprüfverfahrens mit dem Namen „Lorentzkraft-Wirbelstromprüfung“ und dem experimentellen Funktionsnachweis. Das kontaktlose Messverfahren wurde vor Kurzem an der Technischen Universität Ilmenau erfunden und im Rahmen des Graduiertenkollegs 1567 weiter entwickelt. Die vorliegende Arbeit fasst die Ergebnisse der Grundlagenforschung im Bereich experimenteller zerstörungsfreier Werkstoffprüfung mittels Lorentzkraft-Wirbelstromprüfung zusammen, ohne den Anspruch zu erheben, unmittelbar industrielle Anwendungen zu ermöglichen.

Das vorgestellte Verfahren „Lorentzkraft-Wirbelstromprüfung“ bietet durch die Nutzung von magnetischen Gleichfeldern höhere Eindringtiefen als klassische Wirbelstrommessverfahren unter gleichen Einsatzbedingungen, die magnetische Wechselfelder einsetzen. Dies ermöglicht die Detektion von tiefliegenden Defekten innerhalb eines elektrisch leitfähigen nichtferromagnetischen Werkstoffes. Es wird gezeigt, wie Defekte sicher mit der Lorentzkraft-Wirbelstromprüfung erkannt werden (Detektion), wo sie sich befinden (Lokalisation) und bereitet mit der Beschreibung des direkten Problems die Rekonstruktion vor (inverses Problem).

Zur Beschreibung des direkten Problems ist es notwendig, zunächst das Verhalten eines bewegten Festkörpers ohne Defekt in Wechselwirkung mit einem Magnetfeld zu beschreiben. Die Einführung eines relativ simplen Prototypmodels soll Grenzen des Verfahrens aufzeigen und gleichzeitig die grundlegenden Gesetzmäßigkeiten erklären.

Als Funktionsnachweis werden experimentelle Daten für künstliche Defekte vorgestellt. Eine Beschreibung der Grenzen des Messverfahrens und eine Analyse des Messsignals werden am genutzten Versuchsaufbau durchgeführt und Vorschläge zur Erweiterung des Messbereichs gegeben.

Acknowledgement

The work evolved during my scientific employment at the Ilmenau University of Technology. The topic is placed in the framework of the research training group 1567 “Lorentz force velocimetry and Lorentz force eddy current testing”. Therefore, I gratefully acknowledge the financial support from the German Research Foundation (Deutsche Forschungsgemeinschaft). Administratively I have been working at the Institute of Information Technology and therein the Department of Advanced Electromagnetics. Without the help of a lot of people this work would not be done within the requested time.

First, I thank Prof. Zimmermann for the suggestion of applying for the vacant position in the research training group and for the supervision of my work even though I have not been working for his department. The open-minded discussions and the offered help in technical and administrative issues have been valuable and helped to keep track on the research. Furthermore, I thank Prof. Töpfer for the support and help within the Faculty of Electrical Engineering. Prof. Thess has been a great supervisor and teacher who gave important suggestions and ideas which have led to several publications. Prof. Fröhlich, Prof. Haueisen, Prof. Grabow and Prof. Dresig I thank for the fruitful and inspiring technical discussions.

My sincere thanks to Dr. Brauer for the project leadership, the inspiring discussions on technical and administrative problems and the supervision of my work including the correction of my written words. Furthermore, I thank Dr. Ziolkowski whos constructive criticism motivated me to work harder at any time and Dr. Behn who gave me good advices in both, mechanics and teaching. I thank Dr. Fiedler and Dr. Gerlach for the technical support while oscillation measurements.

I am thankful for the discussions and the overall very good cooperation with Mladen Zec and Sebastian Biller. Additionally, I would like to express my thanks to Michael Gramß who helped with his conductivity measurement device and Daniel Strohmeier for his ideas in signal processing. I thank Thomas Szalai for his permanent availability to discuss any technical issues.

Furthermore, I thank Diana Butters for her support and organization skills what saved me a lot of time and the staff of the mechanical work shop for their

patience and precise work which has been delivered fast at any time. I would like to thank my students and assistant researchers for their contributions, so work could be delegated.

Finally, I address my sincere thanks to my parents Iwona and Wolfgang who always supported me in what I am doing and my wife Qin who practiced self-denial while I have been working.

Preface

Dear reader:

The present work evolved during my scientific employment at Ilmenau University of Technology from 2010 to 2012 in the framework of the Research Training Group "Lorentz force velocimetry and Lorentz force eddy current testing" (GK 1567). The Research Training Group has been investigating basically two main topics: (i) velocity measurement of fluids using Lorentz force and (ii) nondestructive testing of nonmagnetic materials using Lorentz force.

The basic principle of using Lorentz force measurements to determine material properties has been invented by the staff members of Ilmenau University of Technology. The Research Training Group has been a result of the invention in order to have the capabilities to provide the basic research. Basic research contains mathematical and numerical modeling and model experiments in order to validate the models. That is why the groups have been set up with experimental and numerical tasks. All connected groups have been working very closely together to make sure that models and experiments fit as well as possible with each other.

Many of my experimental results have been used to validate the numerical model that has been developed by Dipl.-Ing. Mladen Zec. Nevertheless, the results of the experimental validation give a good view on the challenges which one needs to face when applying Lorentz force eddy current testing. I want to point out that in some figures I do not want to obey the numerical results. The reader might get interested in Mr Zec' work as well and wants to read more about the numerical model after he saw the very good agreement between the experiments and the numerical model. Many of the shown results have been published together.

My main intention with this thesis is to provide a methodical approach to prove the functionality of the new nondestructive testing technique "Lorentz force eddy current testing". Therefore, I provide an analytical model to improve the understanding of the basic principle of Lorentz force eddy current testing.

Furthermore, I validate the basic dependencies of the Lorentz force on variable system parameters for specimen without and with defects. I point out the limits of the measurement technique and give ideas how to overcome them.

Sincerely,

R. P. Uhlig

Nomenclature

Symbol	Description	Unit
Variables		
Latin symbols		
$\vec{B}$	magnetic flux density	T
$\vec{B}_0$	primary magnetic flux density	T
$\vec{E}$	electrical field strength	V/m
$\vec{F}$	external force	N
$\vec{F}_g$	gravitational force	N
$\vec{F}_{LF}$	Lorentz force	N
$\vec{Z}$	constraining force	N
A	cross-sectional area	m^2
C	integration constant	$*$
D	thickness of the specimen	m
E	Young's modulus	N/m^4
I	current	A
I_z	area moment of inertia (z-axis)	m^4
L	characteristic length, length	m
M	mass	kg
R	radius of a pipe	m
R_{mag} ...	radius of a spherical magnet	m
R_m	magnetic Reynolds number	$-$
S	sensitivity	N/m
U	voltage	V
V	volume	m^3
$\vec{b}$	secondary magnetic flux density	T
$\vec{e}$	unit vector	$-$
$\vec{f}_{LF}$	Lorentz force density	N/m^3

$\vec{j}$	eddy current density	A/m^2
$\vec{m}$	magnetic dipole moment	Am^2
$\vec{r}$	field point	m
a	starting point of interval	$*$
b	ending point of interval	$*$
c	spring constant	N/m
f	frequency	Hz
f_{corr}	corresponding frequency	Hz
f_{pp}	halt frequency	Hz
f_{tooth} ...	tooth engagement frequency	Hz
$2\,h$	height of the ideal defect	m
k	damping constant	Ns/m
i	counting variable, gear ratio	$-$
j	counting variable	$-$
n_1	number of turns, input gear	Hz
n_2	number of turns, output gear	Hz
q	constant mass per unit length of a beam	kg/m
r_{pinion} ..	pinion radius	mm
s	alignment offset in y-direction	m
t	time	s
t_{anl}	analytically obtained time	s
t_{exp}	experimentally obtained time	s
t_{react}	reaction time in time measurement	s
u	uncertainty in conductivity measurement	S/m
$u_1(x,t)$.	longitudinal deflection	m
$u_3(x,t)$.	transversal deflection	m
v	velocity	m/s
v_0	equilibrium velocity	m/s
w	characteristic velocity	m/s
x	coordinate in direction of x-axis	m
y	coordinate in direction of y-axis	m
z	coordinate in direction of z-axis	m
z_{pinion} ..	number of teeth at pinion	$-$

Greek Symbols

Δx	deflection	m
$\Delta\tau$	falling time difference	–
$\Delta\xi$	path expansion	–
$\Theta(a,\, b)$.	Heaviside function	–
α	nondimensional forcing parameter	–
α_{cal}	calibration constant	S/m
β	nondimensional defect height	–
δ	wall thickness	m
δy	lateral displacement (y-direction)	m
δz	lift-off distance (z-direction)	m
δ_{msd}	motional skin depth (DC magnetic fields)	m
δ_{skin}	skin depth (AC magnetic fields)	m
μ_r	relative permeability	–
ρ	density, radial direction	$\mathrm{kg/m^3}$, –
σ	specific electrical conductivity	S/m
σ_{off}	calibration offset	S/m
τ	nondimensional time parameter	–
$\tau*$	specific nondimensional time	–
ξ	nondimensional position coordinate	–
ξ_0	nondimensional starting position	–

Constants

e	Euler's constant	–
g	gravitational constant	$\mathrm{m/s^2}$
μ_0	absolute permeability	Vs/Am

Contents

1 Motivation and Problem Definition

Quality control is the key for lasting progress in technology. The need of materials with a high load-to-mass ratio in aircraft, car and construction industry has resulted in an increasing demand on high quality materials. Whereas classical methods determine the quality and reliability of the used materials by samples and statistic approaches [1], the boosted demands on the materials force the manufacturers to ensure the needed material quality for every single piece of produced goods.

Nondestructive Testing (NDT) and Evaluation (NDE) of potentially heavily loaded materials have become important in order to save costs and to provide reliable quality control. Material failures lead often to dramatic consequences for the product and its user [2]. Quite often the loss of functionality of technological products causes human casualties. Improving the quality and range of testing techniques helps to fulfill the rising demands in security and in effective application.

A second aspect is the evaluation of material properties during their functional use. In this case the materials cannot be removed and have to be checked at their location. The demand on testing techniques that are applicable during the operation of the specimens is continuously growing since this approach saves a lot of money (assembly time). A very popular example is the inspection of rails [3]. Most interesting are the so-called head cracks which are caused by the high load and the high speed of nowadays traffic and the involved fatigue.

Within the last sixty years the number of available techniques has been grown to more than one hundred [4]. The main markets for nondestructive testing devices are medical care, automotive, nuclear, petrochemical and aircraft industry [5, 6].

Even though many techniques are applied, the results are not comprehensively satisfying. In many of these applications classical nondestructive testing techniques suffer from their physical limits. These limits can be determined with the focus on the defect as defect size, defect geometry and depth of the defect, or with the focus on the application in terms of frequency, usability, size of the testing device and the needs in training the operator. Another important factor is the shape of the specimen which usually differs quite a lot from a tube or a plate (cf. Fig. 1.1).

The main four nondestructive testing techniques are radiography, eddy current testing, ultrasonics and thermography. Especially eddy current testing has a wide range of application due to the low demands for the measurement environment. The probes can be mounted with and without contact and the measurement process is (usually) not dangerous for the operator.

As an alternative for the eddy current testing, a new electromagnetic nondestructive testing technique has been developed at the Ilmenau University of Technology [8]. The main advantage of the so-called Lorentz force eddy current testing is supposed to be the greater penetration depth of the magnetic field which should lead consequently to the detection of deep lying defects within not ferromagnetic electrically conducting materials. Independently from this goal the Lorentz force eddy current testing can serve as an alternative nondestructive testing and evaluation technique. As will be shown, the main advantage is the support of much higher testing speeds and penetration depths at a given spatial resolution.

Whenever a new measurement technique has been introduced, a methodical proof of functionality has to be given. Therefore, analytical investigations on academic prototype models improve the understanding of the underlying physics. Usually, the analytical model serves as a benchmark model for the possibility of the realization of a new idea. The following extensive study of the proposed new technique includes numerical and experimental work. In the thesis at hand, the focus is

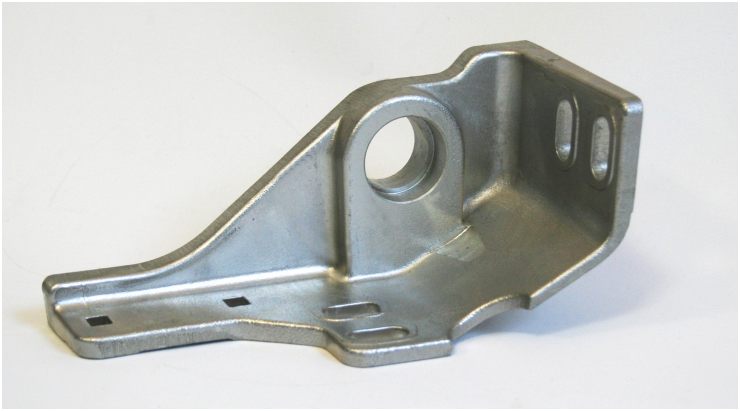

(a)

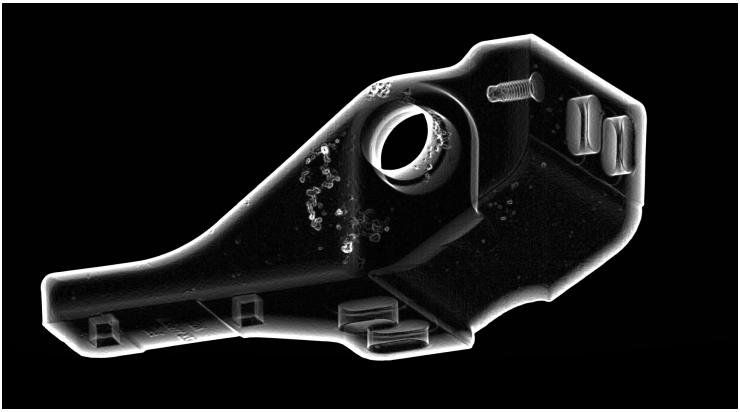

(b)

Figure 1.1: Aluminum casting containing subsurface defects:
(a) Photography,
(b) X-ray, where cavities are observed.
Courtesy of *NTB GmbH*,
`www.ntbxray.com` [7].

clearly on the analytical description and the experimental investigation of a model experiment that serves for the validation of numerical results of [9].

Therefore, a prototype model will be extensively discussed and a measurement setup will be introduced. This setup serves the investigation of the Lorentz force eddy current testing problem within a wide range of adjustable parameters. The functionality of the measurement technique will be proven and the limits of the used measurement setup will be shown. Furthermore, the methodology of commissioning a functional measurement setup within unknown environments will be given.

In a nutshell, the goal of the PhD thesis at hand can be described as follows: (i) Provide an analytical model of the new material testing technique, (ii) prove that the detection of defects is possible to a greater depth than with classical eddy current testing at same working conditions, (iii) provide data for the direct problem of localization and reconstruction of defects using Lorentz force eddy current testing. Thus, the first solution of inverse problems, such as defect identification can be obtained.

The thesis is outlined as follows: In Ch. 2 a short summary of the nowadays available nondestructive testing techniques is given. The basic principles are explained and the current limits are presented. In the next Ch. 3, a conceptually simple model of the Lorentz force eddy current testing is discussed. As will be demonstrated, it is amenable to rigorous analytical treatment and provides a number of unexpected phenomena which are useful for further development of Lorentz force eddy current testing. Although the presented model has no direct practical application, the author believes it is helpful in elucidating the basic laws of Lorentz force eddy current testing and in understanding more complex situations such as will be discussed in Ch. 6. Chapter 4 introduces the measurement apparatus and Ch. 5 the data processing in order to give the reader the possibility to reproduce the presented results. Additionally, in Sec. 6.5 is explained how to exploit Lorentz force eddy current testing to measure the electrical conductivity of materi-

als simultaneously. At the end, in Ch. 7 the results are summarized, conclusions are drawn and an outlook is given.

2 State-of-the-Art in Nondestructive Material Testing

Nondestructive material testing and evaluation (NDT&E) is a vast interdisciplinary field and hence challenging to survey [4, 6, 10, 11]. Whereas the focus of nondestructive testing (NDT) is to detect and localize anomalies within a specimen, the reconstruction of defect properties as dimensions, structure and influence on the material's usability is part of the nondestructive evaluation (NDE), [12].

2.1 Nondestructive Material Testing

Nondestructive material testing is understood as a noninvasive examination of any kind of specimen without changing or altering the test object's properties, in order to check whether the specimen contains anomalies or not. Anomalies are any kind of defects or material property changes that can be of natural or artificial origin, influencing the usefulness or serviceability of that object. Consequently, the list of possible anomalies is long [13].

The main anomalies that have a negative influence on the usefulness of a specimen are cracks caused by false manufacturing methods, fatigue or thinning due to corrosion or erosion [4]. Fatigue results from high mechanical loads and impacts and causes changes in microstructure resulting in e. g. altered conductivity [14]. Obviously, no existing nondestructive testing technique suits the detection of every kind of defect. Due to the physical limitations the method of investigation has to be chosen according to the defects that shall be examined.

The standard in Europe is defined in *DIN EN 1330*. The examination of the objects can be performed during or after the manufacturing process as well as during operation and after failure. The goal is - besides preventing the loss of functionality - the reduction of safety factors in dimensioning of structural components, shorter return-to-investment times for complex and expensive machines and the extension of life-time for extremely expensive machines, e. g. aircrafts [4, 15]. Nondestructive testing turned from a rather empirical procedure that has been dependent on the examiners experience into a more quantitative measurement technique that serves to determine the influence of material anomalies on the structural health of the specimen [12].

In order to classify the existing nondestructive testing techniques according to their limitations and not only according to the physical phenomenon, in the literature it has been proposed to separate the methods in visual, surface and volumetric ones [4] (cf. Fig. 2.1).

Naturally, in many publications the classification in electromagnetic and acoustic methods can be found [10, 13, 16]. The decisive classification factor in this case is the frequency of the examination technique or exploited physical phenomenon.

Especially visual nondestructive material testing is as old as mankind. In order to check whether a designated wood for a spear is useful or not, human beings in ancient time applied visual inspection with the naked eye. Consequently, the visual inspection methods have been improved in magnification and resolution. Nowadays *aided direct vision methods* are widely spread [4]. Whereas mirrors and endoscopes enable the user to examine parts of the specimen that cannot be seen with the naked eye, optical microscopy enables the investigation of the microstructure of objects under test. It is obvious that visual methods are limited to the outer surface of the specimen when access is possible [4, 13]. However, the costs are low and only a minimal training is required.

Certainly many accidents happen due to deep-lying material defects that cannot be seen on the surface but weaken the structure of the

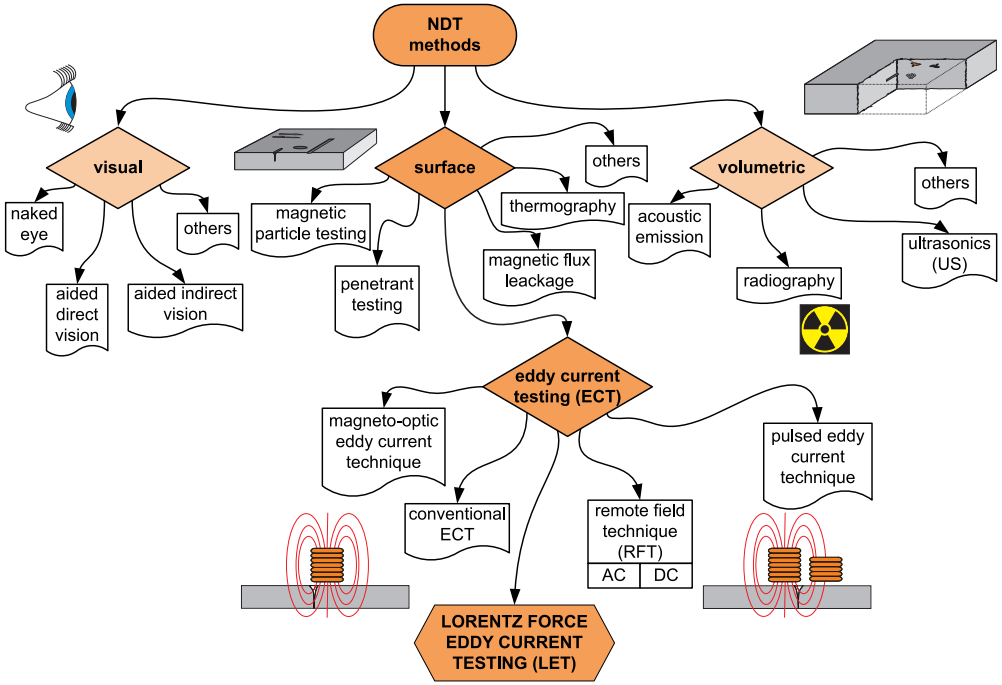

Figure 2.1: Overview of available techniques in nondestructive testing (NDT) in general and place of the Lorentz force eddy current testing in this context.

mechanical parts from within. No matter if it is an exploding vessel or a collapsing building, the danger of human lives necessitated a certain amount of safety of the used material. This necessity unleashed the investigation of the inspection of volumetric defects.

One of the oldest techniques to find anomalies (e. g. enclosures, air bubbles) is the acoustic emission testing or "ringing technique" [4, 13, 16]. Instead of "seeing" an anomaly as in most of the nondestructive testing techniques the aim of the acoustic emission testing is to "hear" it. By applying force, pressure or thermal energy the anomalies are forced to propagate. The propagation itself induces acoustic waves that can be measured by sensitive microphones. A huge advantage of the acoustic emission is that large areas and big volumes can be inspected with only a few transducers and material anomalies are forced to grow (what they do in use, causing failures). The disadvantages are that acoustic emission needs contact to the object under test, the requirement of signal interpretation and the disturbances due to environment [16].

The invention of radiography and ultrasonics enabled the examination of volumetric defects with relatively high spatial resolution compared to acoustic emission with a limited number of transducers. Especially radiography has become the most widely used and accepted volumetric inspection technique. Despite the working safety issues due to radiation hazards, the thickness of the object under test is limited because of the radiation attenuation based on the material density [13].

Overcoming this disadvantages, ultrasonic testing provides information about thickness of the specimen, depth and size of the anomaly. Here, the requirement of couplants and problems with productionally caused dirt has been reported as big disadvantages [13, 17]. The necessity of volumetric methods to examine carbon-fiber reinforced composites has pushed the air-coupled ultrasonic techniques due to the fact that these materials are hygroscopic [18]. One remaining disadvantage of ultrasonic methods is the backscattering of the surface which leads to the effect that surface defects cannot be detected well and that the measurement time is quite long [6]. In terms of nondestructive evalua-

tion anisotropy and heterogeneous material properties impede to draw conclusions from ultrasonic measurements [19].

In order to provide high-resolution measurements just below the surface the so-called surface methods are applied. Some of them will be discussed in the following Sec. 2.2. Everybody dealing with nondestructive testing has to be aware of that there does not exist any method that is applicable for the detection and characterization of every kind of defect [4, 13]. Intelligent systems consisting of sensors of different kind exploit synergy effects and help to improve the inspection [4, 20].

2.2 Surface Methods

An inspection method is understood as a surface method if the detection of defects on and close underneath the surface of the object is possible. While penetrant testing is bound to the outer surface, most of the existing electrical, magnetic and electro-magnetic methods are surface methods with a view beneath the surface [4].

Penetrant testing is a quite simple technique and has many different applications. Roughly summarized a penetrant is applied to the cleaned surface of a component to be tested. After some time the penetrant on the surface is washed away and a fluorescent developer is applied. Due to the capillary action the penetrant entered small defects and can be seen under black light. Main advantages of this technique are low costs, portability, high sensitivity and the virtual application to any solid nonporous material. The limitation to the surface of the object under test including the dependency on surface conditions and the extensive preparation are disadvantageous [13].

Magnetic particle testing represents techniques that are using magnetic particles instead of penetrants. After magnetizing the specimen the magnetic particles are applied on the surface. Due to the leak-

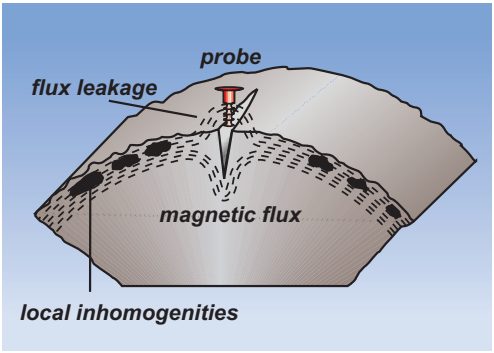

Figure 2.2: Basic principle of the magnetic flux leakage method. The object under test is magnetized. The magnetic flux leaking due to the presence of a defect is measured by a probe. Courtesy of *Institut Dr. Foerster GmbH & Co. KG*, `www.foerstergroup.de` [22].

age fields around a crack the magnetic particles align accordingly. The particles can be fluorescent or detected by magnetic field transducers. One of the biggest disadvantages is that the method is only effective on ferromagnetic materials and that the orientation of the defects is of importance for the probability of detection.

Since not every defect is affecting the functionality of the object, three steps are proposed to detect a crack properly [21]. First of all, the orientation of defects affecting functionality has to be considered. Then the main dimension and the depth of the defect in the material have to be determined. It is mentioned that the width of the defect is not as dominant as the depth of crack-like defects. Due to the fact that the defects are breaking through the surface the application of the magnetic flux leakage is proposed (cf. Fig. 2.2). With the help of Hall-transducers the magnetic leakage field can be measured with very high sensitivity.

A review of the common magnetic inspection techniques is available in literature [11]. The huge advantage of most of the methods is their easier application compared to ultrasonics. Due to the fact that especially steel is being used in many technological branches investigations on the possibility of efficient inspections are being performed.

Another comprehensive overview on the applied nondestructive testing techniques in steel manufacturing industry can be found [17]. There have been investigations on specimens with different kinds of defects at different velocities. The authors point out that a high testing velocity is important due to the rising production costs. Specimens are usually examined while reducing the velocity to suit the nondestructive testing method which results in an overall lower production speed. The challenges of applying ultrasonics have been discussed and alternative surface methods (thermography, flux leakage method, eddy current testing) have been presented.

The influence and the detection of creeping damage which becomes important for heavily loaded objects such as steel pipes has been investigated in [23]. Defects around weld joints have been the focus of this work. The defects are categorized in four different types and an overview of the appropriate detection method has been given - comprising some of the volumetric methods as well.

Another huge field of application is the examination of non-magnetic (more precise: not ferromagnetic) electrically conducting materials [13, 16, 24]. One of the oldest and most common nondestructive testing techniques is the eddy current testing which will be discussed in the following Sec. 2.3.

2.3 Eddy Current Testing

An early application of a differential eddy current testing system has been reported in the late 1870s [25]. On the basis of Faraday's observations on electromagnetic induction and the theory of Maxwell, Hughes has presented a setup to sort metals according to their specific electrical conductivity. The use of a reference specimen and the high sensitivity on its alignment have limited the setup. Nevertheless, the first application of a noninvasive and contactless method has been demonstrated.

The basic principle of eddy current testing is the induction of eddy currents into a specimen which can be done by feeding an alternating current into a coil which itself creates the so-called primary magnetic field. The transient change of the magnetic field induces eddy currents into the electrical conductor according to the induction law:

$$\nabla \times \vec{E} = -\frac{\partial \vec{B}}{\partial t}, \tag{2.1}$$

where $\vec{E}$ is the electrical field strength, $\vec{B}$ the magnetic flux density and t the time.

The eddy currents themselves induce a secondary magnetic field that interacts with the primary magnetic field and with the receiver coil. As long as the conductor is without any anomalies there is an equilibrium state which results in a certain complex impedance of the receiver coil. In the presence of anomalies the flow of the eddy currents is altered. Thus, the secondary magnetic field changes resulting in a change of the complex impedance of the receiver coil. The impedance (absolute) and the change in impedance (differential) of the receiver coil is measured and so, the anomaly is detected. This method is referred to as the conventional eddy current testing (cf. Fig. 2.3).

The real breakthrough of eddy current testing has been the extensive use of submarines and aircrafts in world war II and therewith the need

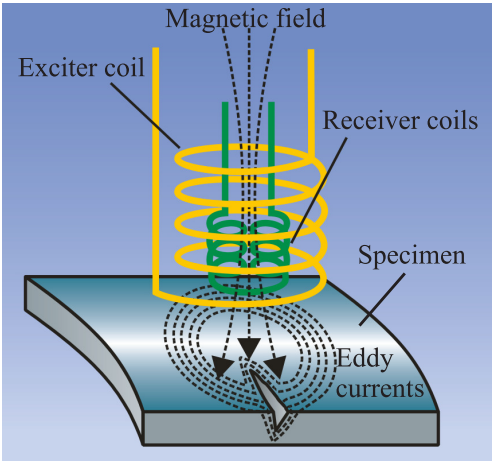

Figure 2.3: Basic principle of the eddy current testing.
Courtesy of *Institut Dr. Foerster GmbH & Co. KG*,
`www.foerstergroup.de` [22].

for safety of the heavily loaded equipment. Thus, the conventional eddy current testing has undergone many improvements, especially concerning the sensitivity of measurement equipment and coil design. Besides the simplicity of application, the accuracy and reproducibility of the measurements helped to evolve from art to an accepted (quantitative) nondestructive testing technique [26].

While the versatile use of conventional eddy current testing for defect detection and material characterization, such as conductivity measurement and permeability measurement even for ferromagnetic materials has been described in [24], the quantitative description of the measurement results has been focused on in [27]. It has been shown that changes in the lift-off distance and the presence of defects alter the magnitude and the phase of the measured impedance. The interest in defect reconstruction has forced investigations on the mathemati-

cal characterization of the primary magnetic field and its interaction with the specimen. This resulted in analytical descriptions for different kinds of coils, e. g. in [28, 29].

Eddy current testing is a surface technique due to the limiting parameter skin depth. The skin depth is per definition the depth in which the current attenuated to $1/e$ (roughly 37%) of its value at the surface of the specimen and depends on the applied frequency, the relative permeability and the conductivity of the specimen [13]. It serves as a measure on how deep internal defects can be detected. Nevertheless in several publications very deep lying defects were detected with eddy current sensors combined with giant-magneto-resistance (GMR) [30], fluxgate [31] and ultra-sensitive superconducting quantum interference device (SQUID) sensors down to a depth of 28.8 mm [32] and even 38 mm [33]. Even for laminated structures deep lying defects can be detected to a depth of 20.4 mm applying GMR-based eddy current testing [34]. Despite the ultra-sensitive magnetic field sensors, low excitation frequencies enable this deep detection resulting in rather low measurement velocities and poor spatial resolution. Nevertheless, the detection of very deep lying defects can be understood as a benchmark problem in the examination of the technique's limits.

The wish for larger detection depths, higher sensitivity, higher probability of defect detection and the need for short measurement times evolved many different eddy current based techniques. Multifrequency approaches and combinations with other sensor types have led to a vast amount of different techniques [26, 35]. A GMR-based eddy current testing instrument of the size of a computer mouse has been reported by [36] and is able to detect surface breaking defects at measurement velocities up to 10 mm/s.

Especially differential eddy current testing sensors are very sensitive to small changes in the impedance (cf. Fig. 2.4). The adjustment of the measurement range around zero and the possibility of high resolution electronics has given rise to a high amount of applications. Thus, the detection of deep lying defects is reported to a depth of 18 mm

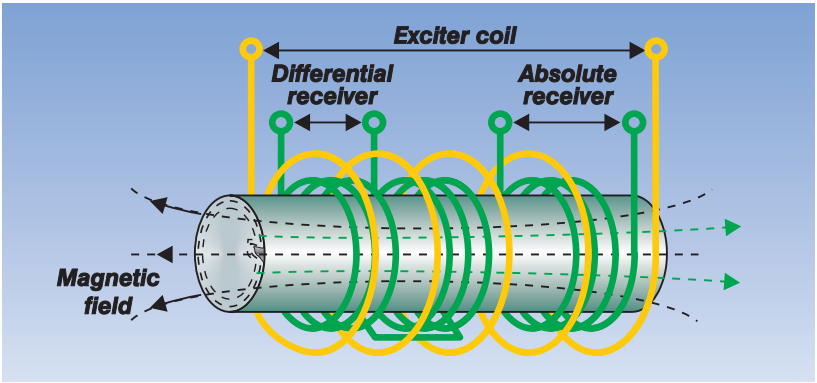

Figure 2.4: Basic principle of differential eddy current testing combined with an absolute measurement. The absolute receiver measures the impedance. The differential receiver measures the change in impedance caused by a defect.
Courtesy of *Institut Dr. Foerster GmbH & Co. KG*, `www.foerstergroup.de` [22].

experimentally and 28 mm numerically [37]. A novel differential eddy current testing technique comprising a rectangular coil which is capable to detect the growth direction of surface breaking defects has been reported [38]. A new approach using phase shifted excitation fields enables higher inspection speeds and a higher probability of detection of deep lying defects [39].

In order to reduce the necessity of intense training of the examiner, the ultrasonic-like imaging is proposed [40]. The characterization of defects is reported to be done by analysis in frequency domain. Imaging itself is used for the so-called magneto-optic eddy current testing. Modern portable systems comprise a head-mounted display on which the examiner can see anomalies through several layers of laminated material with a minimum of training in real-time [15]. Due to the still relatively low

speed of manual inspection robots are developed for the examination of complex shaped objects [41]. The reported flexibility of the robot arm is comparable with the human arm whereas the reproducibility of measurements increases due to the precise motion control on the basis of inverse kinematics.

In future inspection on low-conducting materials such as carbon-fiber reinforced composites is going to gain more and more importance due to the fact that these materials have a very good load-to-mass ratio. Even though thermography is at the moment superior in determining defects as delamination in these composites [42], the inspection is basically possible [26]. But not only the detection of delamination is needed. Inclusions of microscopic particles splinted from tools while manufacturing can cause serious damage on aircrafts. The reliable detection applying eddy current testing has been reported [43].

Since the number of applications in eddy current testing is vast and the capabilities of numerical computation have grown steadily, most of the considered problems are studied numerically. Numerical investigations save costs, time and material. However, a drawback of numerical simulations is that the applied model is deterministic and the measurement signal is not noisy. The noise is understood as a variation of the measurement signal in time. Usually this variation is decreasing the probability of detection of a defect significantly [37]. Consequently, the adaption of numerical models by including noise based on a *a priori* determined distribution has been proposed in [44].

A differential testing technique is the so-called remote field eddy current testing [45]. The source coil is separated from the detection coil in such a way that the direct interaction between both is minimal (sometimes shielded against each other). The magnetic field lines close on an indirect path through the specimen. Anomalies perturb the magnetic field lines and cause a transient change in the magnetic flux which induces a measurable voltage in the detection coil. The technique has been developed and investigated both experimentally and numerically focusing on the application in pipe inspection [46]. It can be applied

for planar objects as well [47, 48]. It has been demonstrated that the remote field eddy current testing provides a higher sensitivity than conventional eddy current testing and is suitable for the detection of (artificial) anomalies even in laminated structures to a depth of 17 mm [49].

The application of remote field eddy current testing sensors in sensor arrays has been investigated [50]. It has been demonstrated that each sensor can be used as source and detector at same time. In difference to the conventional eddy current testing the detection of the remote field is appreciated. Due to the "Mexican hat point spread function" of a remote field eddy current testing sensor the ability of result imaging is very good [51]. It has been demonstrated that a clear image of defects 1 mm beneath the surface is possible using measurements with velocities of up to 50 mm/s in microscanning technique.

Furthermore, development on data fusion of different nondestructive testing techniques is recognized to be promising to improve the probability of defect detection [26, 52]. Especially the combination of ultrasonics and eddy current testing is promising due to the fact that the advantages of each technique compensate limitations of the other one. Thus, applications in rail inspection have been reported with high measurement velocities up to 90 km/h [53]. Nevertheless, improvements are still required because eddy current testing does not provide deep enough penetration for ferromagnetic materials to cover the full backscattering region of ultrasonics [54]. Despite that, the successful application to carbon-epoxy composites has been reported [18]. Due to the higher number of measured signals multi-sensor data fusion increases requirements to the data processing techniques. Improvements in defect evaluation using fuzzy algorithms and neuron networks have been reported mainly in the field of defect reconstruction [5].

The classical eddy current testing suffers strongly from lift-off effects, the surface conditions of the specimen and the frequency dependent skin effect [13, 16]. Efforts have been taken to overcome some of these limitations. Thus, alternative mechanisms for the induction of eddy

currents have been investigated focusing on nondestructive testing capabilities [8, 55, 56]. The use of permanent magnetic fields turned out to be promising to avoid the frequency dependent skin effect and suppresses lift-off effects using appropriate data processing [57]. Due to the physical need of relative motion between the specimen and the magnetic field source, the methods are classified as motion induced eddy current testing and Sec. 2.4 is devoted to them.

2.4 Motion Induced Eddy Current Testing

Eddy currents are induced in electrically conducting materials whenever the magnetic field is changing in time (cf. Eq. (2.1)). The transient change has absolutely not to be created by an alternating (AC) magnetic field. Relative motion between a magnetic field source and the electrically conducting object causes a transient change of the magnetic field in the specimen generating eddy currents. The magnetic field source can be a direct current driven electromagnet or a permanent magnet. Both create a direct (DC) magnetic field.

An alternative method in the field of remote field eddy current testing has been presented as motion induced remote field eddy current testing [46]. Basically, it is the DC variant of the remote field eddy current testing discussed in Sec. 2.3. Nevertheless, it has been demonstrated that the method is capable of detecting deep lying defects in any kind of electrically conducting material. The high speed application in pipe inspection at velocities of up to 5 m/s has been reported [58]. An industrial use for the inspection of flat material in rolling mills has been presented as well [59]. Especially the fact that the sensor works on differential basis results in high sensitivity to defect detection inside the material.

Anyway, the interaction between direct magnetic fields and electrically conducting materials found interest already much earlier. The physical

effect of magnetic levitation led to several investigations [60]. Especially the acting Lorentz force as a result of the interaction between the magnetic field source and the secondary magnetic field has been of big interest [28, 61, 62]. Besides magnetic levitation for transportation, the Lorentz force has found application in electromagnetic braking [63].

The drag force generated by the interaction of a permanent magnet with a metallic material in relative motion can be used to determine the material properties [55]. Further investigations, especially on ferromagnetic materials, led to the so-called drag force method [56, 64]. The determination of hysteresis losses has enabled to draw conclusions on fatigue [65] and residual stresses [66]. A numerical model which is applied in order to predict and study hysteresis losses has been developed as well [67].

The determination of defects in nonmagnetic material by measuring Lorentz force perturbations has found its application in the so-called Lorentz force eddy current testing [8]. There, the proof of principle has been provided with large defects which have been detected with the help of a complex magnet system. The thesis at hand provides a more comprehensive study on the physical behavior of the measured force on changing system parameters what can be validated with the work on magnetic levitation [61, 62]. This basic research helps to understand the basic physics behind the proposed technique and evaluates the limits of the existing measurement setup. Especially the proof of concept is provided for rather small artificial defects deep inside the specimen. With the help of the measured forces the reconstruction of the defects is possible [68]. Furthermore, Lorentz force eddy current testing can be used for the nondestructive evaluation of material properties, e. g. the electrical conductivity. An appropriate signal processing provides a force signal which is less sensitive to lift-off effects.

Further studies on the interaction of a DC magnetic field with an electrically conducting bar have been performed by [69]. Experimental and numerical investigations have shown that the measurement of all three components of the Lorentz force enables the detection of defects [70–72]

and the determination of the electrical conductivity of the object under test [57].

Due to the fact that the interaction of a permanent magnet with any electrically conducting material in relative motion (including fluids) is causing the velocity-dependent Lorentz force, the determination of casting velocities of molten metal has found its application in the Lorentz force velocimetry [73, 74]. Naturally the method depends on the accuracy of the force measurement system. Due to further improvements on force sensors, the usability of Lorentz force velocimetry for low conducting fluids, e. g. salt water and glass melts, has been demonstrated [75].

3 Theoretical Basis of Lorentz Force Eddy Current Testing

Within this chapter a simple model of the Lorentz force eddy current testing that is suitable for analytical treatment is presented and discussed. Even if it has no practical application and despite of educational purposes, it helps to elucidate the basic principle which Lorentz force eddy current testing is based on.

In Sec. 3.1, the mathematical model is derived and discussed. In order to validate the model results, a comparison with an experiment has been performed. A more comprehensive analysis can be found in [76] comprising a numerical model that serves to formulate the limits of the analytical approach. In order to understand the link to the presented Lorentz force eddy current testing in Sec. 3.2 the idea is given and hypotheses about its advantages are made.

3.1 A Prototype Model - The Creeping Magnet

The model presented here is a slight modification of a popular educational experiment sketched in Fig. 3.1a. The experiment is used to introduce Faraday's law of induction and consists of dropping a permanent magnet through a vertical, electrically conducting nonmagnetic pipe [77–80].

The discussion is divided into two parts. The first part is concerning the pipe without any defect in order to provide the solution of the educational problem. The second part is comprising the analytical solution of the problem of a pipe with an artificial defect (cf. Fig. 3.1b)

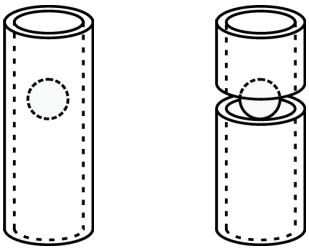

Figure 3.1: Permanent magnet and pipe with different defect shapes
(a) No defect,
(b) Idealized axisymmetric defect.

and an extensive discussion of the results. An experimental validation is provided as well [76].

3.1.1 Pipe Without Defect

An infinitely long electrically conducting non-(ferro)magnetic pipe is considered. The "creeping magnet problem" described here refers to the case when the pipe is at rest and a spherical permanent magnet with the radius R_{mag} is released to fall through the pipe. The magnetic field outside of the spherical magnet (uniform magnetization) is equivalent to that of a magnetic point dipole that is located in the center of the sphere [81]. If the pipe contains no defect, the magnetic dipole falls with a constant velocity. The goal of the analysis is to predict the time-dependent position $z(t)$ of the falling magnet by determining its velocity. The analytical model of this problem has been derived in [82] and has been applied in [77]. In order to improve the understanding of the physics behind Lorentz force eddy current testing the solution of the educational problem is applied as follows.

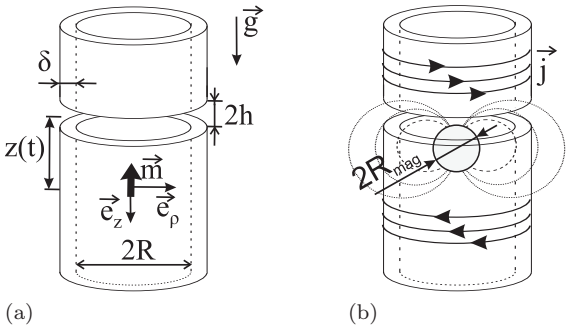

Figure 3.2: Geometrical sketch containing the characteristic parameters,
(a) Mathematical model,
(b) Real geometry with eddy currents $\vec{j}$ and spherical magnet (radius R_{mag}).

The analytical model of the pipe and the magnetic dipole can be described by the parameters shown in Fig. 3.2a. Since a magnetic point dipole concentrates its mass within a single point the mechanical models for point masses can be applied. The movement of such a point mass is described by Newton's equation of motion:

$$M\,\ddot{\vec{r}} = \sum_{(i)} \vec{F}_i + \sum_{(j)} \vec{Z}_j, \tag{3.1}$$

where M is the moving mass, $\vec{r}$ the field point, $\vec{F}_i$ are external forces and $\vec{Z}_j$ constraining forces. Due to the fact that the movement is performed along the z-axis only, the field point, the velocity and the acceleration are given by

$$\vec{r} = z(t)\,\vec{e}_z, \tag{3.2}$$

$$\dot{\vec{r}} = \dot{z}(t)\,\vec{e}_z, \tag{3.3}$$

$$\ddot{\vec{r}} = \ddot{z}(t)\,\vec{e}_z, \tag{3.4}$$

where $\vec{e}_z$ is the unit vector in z-direction.

Clearance cutting of the magnetic dipole leads to the acting forces. The dipole is accelerated in positive z-direction by the gravitational force $\vec{F}_g$ and decelerated by the Lorentz force $\vec{F}_{LF}$. Due to the fact that the dipole is freely falling the constraining forces are zero:

$$\sum_{(i)} \vec{F}_i = \vec{F}_g + \vec{F}_{LF}, \tag{3.5}$$

$$\sum_{(j)} \vec{Z}_j = 0. \tag{3.6}$$

The forces are determined by the following equations considering their right directions:

$$\vec{F}_g = M\,g\,\vec{e}_z, \tag{3.7}$$

$$\vec{F}_{LF} = \iiint\limits_{(V)} \left(\vec{j} \times \vec{B}\right) dV. \tag{3.8}$$

As one can see the gravitational force $\vec{F}_g$ is depending only on the mass of the magnetic dipole M and the gravitational constant g whereas the Lorentz force $\vec{F}_{LF}$ depends on the eddy currents $\vec{j}$, the magnetic flux density $\vec{B}$ and the conductor volume V.

The magnetic flux density $\vec{B}$ that is produced by the magnetic dipole at any point in space is calculated according to [83] by

$$\vec{B} = \frac{\mu_0}{4\,\pi} \left\{ 3\,\frac{(\vec{m}\cdot\vec{r}\,')\;\vec{r}\,'}{|\vec{r}\,'|^5} - \frac{\vec{m}}{|\vec{r}\,'|^3} \right\}, \tag{3.9}$$

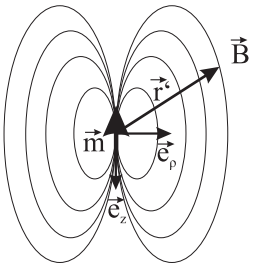

Figure 3.3: Field point $\vec{r}'$ used in the analytical model to calculate the magnetic induction $\vec{B}$.

where $\vec{r}'$ is the field point starting at the magnetic dipole pointing at a point in space (cf. Fig. 3.3), $\vec{m}$ is the magnetic dipole moment and μ_0 the absolute permeability. The magnetization of the magnetic dipole is directed along the z-axis with the magnetic dipole moment

$$\vec{m} = -m\,\vec{e}_z. \tag{3.10}$$

This magnetization direction is an stable equilibrium state. Any deviation from this orientation leads to momenta which orient the magnetization back along the z-axis. In reality the material of the pipe is neither homogeneous nor isotropic. Due to that fact and friction effects a motion along a helicoidal line is observed. The analytical model is only taking the translational motion into account whereas rotation has been neglected.

The pipe wall thickness has been assumed to be small in comparison to the inner radius of the pipe in order to neglect the magnetic flux density decay within the pipe wall. So, only the magnetic field at the pipe wall at $\vec{r}' = R\,\vec{e}_\rho$ is contributing to the generated eddy currents. Additionally the problem at hand is axisymmetric. Thereby, only the radial component of the imposed magnetic field needs to be considered.

Using the nondimensional position coordinate $\xi(t) = z(t)/R$, the radial component of the magnetic induction B_ρ can be written as

$$B_\rho = -\frac{3\,\mu_0\,m}{4\,\pi\,R^3}\,\frac{\xi'}{\left(1+\xi'^{\,2}\right)^{\frac{5}{2}}}. \tag{3.11}$$

The relative movement between the dipole and the pipe induces eddy currents that are governed by Ohm's law for moving conductors which has the form

$$\vec{j} = \sigma\,\left(\vec{E} + \dot{\vec{r}} \times \vec{B}\right). \tag{3.12}$$

Moreover, if there is no source or sink of electric currents in the pipe, the distribution of the induced eddy currents is purely azimuthal and the electric field is zero. In this case the φ-component of Ohm's law for moving conductors (cf. Eq. (3.12)) simplifies to $j_\varphi = \sigma\,\dot{z}(t)\,B_\rho$ and the eddy currents become

$$j_\varphi = -\frac{3\,\mu_0\,m\,\sigma\,\dot{z}(t)}{4\,\pi\,R^3}\,\frac{\xi'}{\left(1+\xi'^{\,2}\right)^{\frac{5}{2}}}. \tag{3.13}$$

These currents give rise to a secondary magnetic field. The resulting magnetic field represents a superposition of both, the primary and the induced secondary field. The magnetic field associated with the induced eddy currents is much smaller than the applied primary magnetic field, and is neglected.

The resulting Lorentz force density is calculated using $\vec{f}_{LF} = \vec{j} \times \vec{B}$. The only azimuthal distribution of the eddy currents and the assumed radial distribution of the magnetic flux density within the pipe wall lead to a Lorentz force density $\vec{f}_{LF}$ that is acting only in z-direction:

$$f_{LF,z} = -j_\varphi\,B_\rho = -\frac{9\,\mu_0^2\,m^2\,\sigma\,\dot{z}(t)}{16\,\pi^2\,R^6}\,\frac{\xi'}{\left(1+\xi'^{\,2}\right)^{5}}. \tag{3.14}$$

Integrating the Lorentz force density over the volume of the pipe leads to the total Lorentz force

$$F_{LF,z} = -\frac{9\,\mu_0^2\,m^2\,\sigma\,\delta\,\dot{z}(t)}{8\,\pi^2\,R^4} \underbrace{\int_{-\infty}^{\infty} \frac{{\xi'}^2}{\left(1+{\xi'}^2\right)^5}\,d\xi'}_{=\frac{5\,\pi}{128}}. \tag{3.15}$$

This Lorentz force acts, due to Newton's third axiom "action equals reaction", on both, the pipe and the magnet (in opposite direction) [84]. Consequently, the integration leads to the total Lorentz force acting on a pipe without defect F_0:

$$F_{LF,z} = F_0 = -\frac{45\,\mu_0^2\,m^2\,\sigma\,\delta}{1024\,R^4}\,\dot{z}(t). \tag{3.16}$$

The calculated Lorentz force F_0 depends on the velocity and the properties of both, the magnetic dipole and the pipe. The geometrical and material properties are given by the setup under investigation. This Lorentz force can be reinserted in Newton's equation of motion, see Eq. (3.1). The result is

$$M\,\ddot{z}(t) = F_0 + F_g. \tag{3.17}$$

Due to the fact that the gravitational force F_g is accelerating the motion of the dipole whereas the Lorentz force F_0 is opposing the motion linearly with velocity, there has to be an equilibrium state, when both external forces are equal. At this moment, the acceleration of the magnetic dipole turns to $\ddot{z}(t) = 0$ and the dipole is falling with equilibrium velocity v_0. This fact can be described by the modified Newton's equation of motion

$$0 = -\frac{45\,\mu_0^2\,m^2\,\sigma\,\delta}{1024\,R^4} \cdot v_0 + M\,g. \tag{3.18}$$

Solving this equation for the equilibrium velocity v_0 leads to

$$v_0 = \frac{1024\, M\, g\, R^4}{45\, \mu_0^2\, m^2\, \sigma\, \delta}. \tag{3.19}$$

The equilibrium velocity of the magnetic dipole is constant and depends on the gravitational constant, material parameters and the geometry of the pipe. The use of good conductors with thick walls together with strong magnets will result in a very strong deceleration of the free fall when the gap between pipe and magnet is small.

This fact is well known, cf. [77–80]. In the following section a pipe with an ideal defect will be considered in order to study the feasibility of force measurements for the detection of defects. The case of a pipe without defect is necessary in order to introduce the values of the unperturbed Lorentz force F_0 and the equilibrium velocity v_0. Thus, it is easier to detect the changes caused by the defect.

3.1.2 Pipe With an Ideal Defect

The basis of the following discussion is the infinitely long pipe containing exactly one ideal defect as shown in Fig. 3.1b and Fig. 3.2a. The defect consists of a gap with a height of $2\,h$ in which the electrical conductivity is assumed to be zero. Since the pipe is interrupted symmetrically around $z = 0$, Eq. (3.15) has to be adapted appropriately. The integration interval is split into two parts $(-\infty; -h/R]$ and $[h/R; \infty)$. Applying the additivity of integration on intervals the perturbed Lorentz force is calculated by

$$F_{LF,z} = F_0 + \frac{9\, \mu_0^2\, m^2\, \sigma\, \delta\, \dot{z}(t)}{8\, \pi^2\, R^4} \int_{\xi' = \frac{z-h}{R}}^{\xi' = \frac{z+h}{R}} \frac{{\xi'}^2}{\left(1 + {\xi'}^2\right)^5}\, d\xi'. \tag{3.20}$$

The term consists of the unperturbed Lorentz force F_0 and the modification due to the influence of the defect. Notice that the direction of the Lorentz force is along the negative z-axis, i. e. $F_{LF,z} < 0$. So the perturbation results in a decrease of the total acting Lorentz force $|F_{LF,z}| < |F_0|$. Introducing the Lorentz force into Eq. (3.17) leads to the differential equation of motion that describes the falling magnetic dipole through a pipe which is containing an ideal defect:

$$M\,\ddot{z}(t) = -\frac{45\,\mu_0^2\,m^2\,\sigma\,\delta}{1024\,R^4}\,\dot{z}(t) + \frac{9\,\mu_0^2\,m^2\,\sigma\,\delta}{8\,\pi^2\,R^4}\,\dot{z}(t)\int\limits_{\xi'=\frac{z-h}{R}}^{\xi'=\frac{z+h}{R}}\frac{{\xi'}^2}{\left(1+{\xi'}^2\right)^5}\,d\xi' + M\,g. \quad (3.21)$$

In order to reduce the number of independent variables the quantities are normalized on the basis of the scales R and v_0/g for length and time, which are characteristic for the given problem. As a consequence, the time derivatives contain no time anymore but a dimensionless time parameter τ. The nondimensional parameters are calculated as follows:

$$\alpha = \frac{v_0^2}{g\,R} \quad (3.22)$$

$$\beta = \frac{h}{R} \quad (3.23)$$

$$d\tau = \frac{g}{v_0}\,dt. \quad (3.24)$$

Introducing the nondimensional parameters into Eq. (3.21) results in the nondimensional equation of motion:

$$\ddot{\xi} + \left[1 - \frac{128}{5\,\pi}\int\limits_{\xi'=\xi-\beta}^{\xi'=\xi+\beta}\frac{{\xi'}^2}{\left(1+{\xi'}^2\right)^5}\,d\xi'\right]\dot{\xi} = \alpha \quad (3.25)$$

with the initial conditions

$$\xi\,(\tau = 0) = \xi_0, \tag{3.26}$$

$$\dot{\xi}\,(\tau = 0) = \alpha, \tag{3.27}$$

where ξ_0 is the starting position.

Equation (3.25) is a nonlinear ordinary differential equation of second order containing two dimensionless parameters, namely α and β. To highlight the mathematical structure of the equation of motion it can be rewritten as

$$\ddot{\xi} + f\,(\xi, \beta)\;\dot{\xi} = \alpha. \tag{3.28}$$

The function $f\,(\xi, \beta)$ represents a position-dependent electromagnetic friction coefficient which differs from its unperturbed value $f = 1$ only in a small neighborhood of the defect location $\xi = 0$. A peculiarity of the present problem consists of the fact that the value of this coefficient is determined by an integral over the whole pipe. Before passing on the solution of this model it is useful to discuss the physical meaning of the parameters α and β briefly.

All geometrical data and material properties are contained in α. This parameter can be interpreted as a forcing parameter since it appears on the right-hand side of Eq. (3.25). If there is no defect, this equation reduces to

$$\ddot{\xi} + \dot{\xi} = \alpha.$$

The solution $\xi(\tau) = \alpha\,\tau$ describes steady electromagnetically damped motion of the magnet with constant downward velocity α. Notice that α represents the ratio between the unperturbed velocity v_0 and the velocity $\sqrt{g\,R}$ which a freely falling body would attain in the absence of electromagnetic damping after having traversed a height $R/2$. Hence, small values of α correspond to low velocity and strong electromagnetic damping whereas higher values of α indicate a higher velocity and weak damping. The "geometry" of the defect is described by the parameter β where $\beta = 0$ represents the pipe without defect.

Ideal Defect - General case

Selected numerical solutions of Eq. (3.25) are shown in Fig. 3.4. The solution has been calculated using an iterative solver for the finite difference method realized in *MATLAB*. The provided solutions highlight the role of the parameters α and β. The solution is presented in the form $\dot{\xi} = f(\xi)$ representing the velocity of the falling dipole as a function of the position. This representation is more convenient for the present work than the seemingly more natural form $\xi = f(\tau)$ (see Fig. 3.5) because it allows the determination of the falling velocity of the dipole at one particular location relative to the defect. Figure 3.4a shows, in particular, the solution for variable α for fixed $\beta = 0.01$ corresponding to the experiment to be discussed below, whereas in Fig. 3.4b $\alpha = 0.0592$ is kept constant and β is changed. One apparently counterintuitive feature is common to all solutions shown in Fig. 3.4. Based on qualitative reasoning, one may expect that the presence of a defect would lead to a temporary rise in velocity, and that the curve $\dot{\xi} = f(\xi)$ would therefore have a bell-shape with a single maximum velocity close to the location of the defect, i. e. close to $\xi = 0$. By contrast, all curves shown in Fig. 3.4 have two maxima rather than one. This indicates that the falling magnet experiences two phases of acceleration when passing the defect. The reason for this behavior can be easily understood by invoking Fig. 3.2b in which the qualitative structure of the eddy currents is shown. Figure 3.2b shows that the eddy currents induced by the moving dipole consist of two structures with opposite orientation. This leads to the fact that the Lorentz force has two minima rather than just one and that $\dot{\xi} = f(\xi)$ has two maxima if the gap is not too wide.

Figure 3.4a shows that $\dot{\xi} = f(\xi)$ is symmetric for small values of the forcing parameter. When α increases, the velocity distribution becomes asymmetric due to the increasing influence of inertia for high velocities. Bigger defects cause an asymmetry in the velocity distribution as shown in Fig. 3.8b. There, the acceleration phase is dominating when the magnet is exerting a decrease of the breaking Lorentz force due to the presence of a defect.

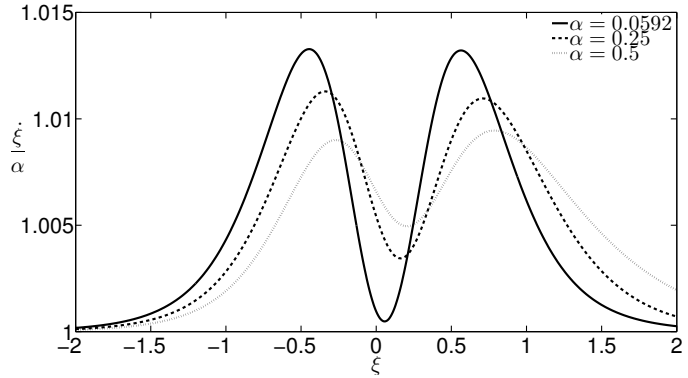

(a)

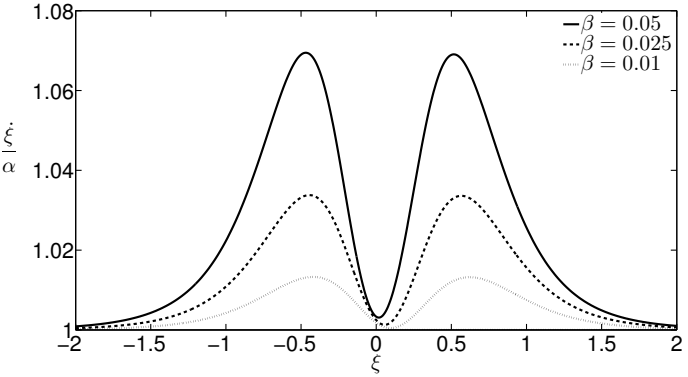

(b)

Figure 3.4: Velocity distribution in the defect region as obtained from the solution of Eq. (3.25) without any further approximations,
(a) $\beta = 0.01$, different α
(b) $\alpha = 0.0592$, different β.

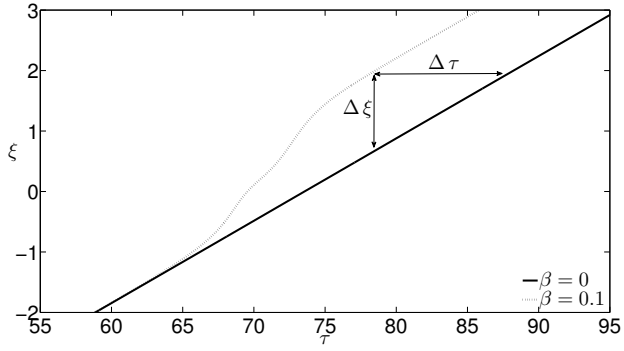

Figure 3.5: Path of the magnetic dipole with and without a defect in the pipe; $\Delta\tau$ - time shift, $\Delta\xi$ - path expansion, where $\alpha = 0.0592$.

The resulting path of the dipole is shown in Fig. 3.5. When the unperturbed path (full line) is compared with the distance traveled in the presence of the defect (dotted line), two features become apparent. In a given time the magnetic dipole travels a distance that is $\Delta\xi$ longer than in the unperturbed case. From another point of view, the dipole arrives $\Delta\tau$ earlier at any position that is sufficiently far "downstream" of the defect. In the following $\Delta\tau$ is referred to as the falling time difference, whereas $\Delta\xi$ is the path expansion compared to the nondefective pipe.

Since the falling time difference is a direct effect of the Lorentz force perturbation it will be used for the experimental validation. It is a particularly important quantity, used to detect and identify the defect. To get a first idea of the characteristic change of falling time for any size of the defect, the motion in the defect region is investigated. Therefore Eq. (3.25) has to be integrated for $\tau = [-\tau^*; \tau^*]$ where τ is the nondimensional time scale and $-\tau^*$ the nondimensional time when entering

the defect region. Considering the height of the defect region to be $2\,\beta = 2\,h/R$ and the fly-by time $\Delta\tau = 2\,\tau^*$, Eq. (3.25) turns to

$$\left[\dot{\xi}\,(\tau^*) - \dot{\xi}\,(-\tau^*)\right] + \left[\xi\,(\tau^*) - \xi\,(-\tau^*)\right] = \alpha\,\Delta\tau + \frac{128}{5\pi}\int_{-\tau^*}^{\tau^*} d\,\tau\,\dot{\xi}\int_{\xi-\beta}^{\xi+\beta}\frac{\xi'^{\,2}}{\left(1+\xi'^{\,2}\right)^5}\,d\xi'. \quad (3.29)$$

The magnetic dipole is falling with equilibrium velocity when being outside the defect region. This fact is described by

$$\lim_{\tau^*\to\infty}\left\{\dot{\xi}(\tau^*) - \dot{\xi}(-\tau^*)\right\} = 0. \quad (3.30)$$

Inserting Eq. (3.30) into Eq. (3.29) is leading to

$$\xi\,(\tau^*) - \xi\,(-\tau^*) = \alpha\,\Delta\tau + \frac{128}{5\pi}\int_{\tau^*=-\infty}^{\tau^*=\infty} d\,\tau\,\frac{d\,\xi}{d\,\tau}\int_{\xi-\beta}^{\xi+\beta}\frac{\xi'^2}{\left(1+\xi'^2\right)^5}\,d\xi'. \quad (3.31)$$

Introducing the Heaviside function $\Theta(a,\,b)$ into Eq. (3.31) the integration limits can be exchanged. Applying two Heaviside functions $\Theta(a,\,b)$ a window with a length of $2\,\beta$ is generated. Considering that $\lim_{\tau^*\to\infty}\xi(\tau^*) = \infty$ one finds

$$\Theta\,(a,\,b) = \begin{cases} 0; & a < b \\ 1; & a \geq b \end{cases}, \quad (3.32)$$

$$\xi(\tau^*) - \xi(-\tau^*) = \alpha\,\Delta\tau + \frac{128}{5\pi}\int_{\xi=-\infty}^{\xi=\infty}\int_{\xi'=-\infty}^{\xi'=\infty} W(\Theta)\,f(\xi')\,d\xi'\,d\xi, \quad (3.33)$$

where $W(\Theta) = \Theta(\xi', \xi - \beta) - \Theta(\xi', \xi + \beta)$ and $f(\xi')$ is the integrand that depends only on ξ'. The evaluation of the integral leads to

$$\underbrace{\xi(\tau^*) - \xi(-\tau^*)}_{=\Delta\xi} = \alpha\,\Delta\tau + \frac{128}{5\,\pi}\,2\,\beta \underbrace{\int_{\xi'=-\infty}^{\xi'=\infty} \frac{\xi'^2}{\left(1+\xi'^2\right)^5}\,d\xi'}_{=\frac{5\pi}{128}}, \tag{3.34}$$

which can be condensed to

$$\Delta\xi = \alpha\,\Delta\tau + 2\,\beta. \tag{3.35}$$

Since $2\,\beta$ is the normalized defect length and $\Delta\tau$ is the fly-by time one can conclude that the dipole's distance traveled increases by the same length as the size of the defect and the flight time shortens by the unperturbed fly-by time. Thus, it has been shown analytically that the falling time difference is increasing linearly with the defect height and that $\Delta\xi$ and $\Delta\tau$ obey the rigorous relations

$$\Delta\xi = \quad 2\,\beta\,\Big|_{\Delta\tau\to 0} \tag{3.36}$$

$$\Delta\tau = -\frac{2\,\beta}{\alpha}\,\Big|_{\Delta\xi\to 0} \tag{3.37}$$

This analysis is performed under the assumption that the pipe contains exactly one idealized defect. Moreover, only the presence and the size of a defect is determined, but not its location. In order to simplify the equation of motion and gain more information about the behavior of the dipole motion, an analysis dealing with two extreme defect sizes is performed. This is referred to as the so-called narrow and large defect approximation, respectively.

Narrow defect approximation

Assuming a very small defect, compared with the radius of the pipe, the equation of motion can be further simplified. Stating that $\beta \ll 1$, the integral appearing in Eq. (3.25) is approximated as the integrand itself multiplied by the length of the integration domain. This leads to the simplified equation of motion

$$\ddot{\xi} + \left[1 - \frac{256\,\beta}{5\,\pi}\,\frac{\xi^2}{\left(1+\xi^2\right)^5}\right]\,\dot{\xi} = \alpha, \tag{3.38}$$

that can be rewritten as

$$\ddot{\xi} + C\left(\xi, \beta\right)\,\dot{\xi} = \alpha, \tag{3.39}$$

where

$$C\left(\xi, \beta\right) = \left[1 - \frac{256\,\beta}{5\,\pi}\,\frac{\xi^2}{\left(1+\xi^2\right)^5}\right]. \tag{3.40}$$

Using the narrow defect approximation (NDA), the dynamics of the falling dipole are equivalent to the motion of a mass with a position dependent linear friction coefficient. Its value is given by the term $C(\xi,\,\beta)$ in Eq. (3.40). The initial conditions remain the same as formulated in Eqs. (3.26) & (3.27). Figure 3.6 shows the spatial structure of this coefficient which can be considered as an electromagnetic friction coefficient in comparison with the perturbation coefficient $f(\xi,\,\beta)$ of the complete solution. Notice that in the framework of the NDA, the height of the defect β only affects the amplitude but not the shape of the position-dependent part of $C(\xi,\,\beta)$. It should also be emphasized that $C\left(\xi,\,\beta\right)$ is symmetric with respect to the location of the defect and $C(\xi,\,\beta = 0) = 1$ as well as $C(\xi = 0,\,\beta) = 1$. These properties are consequences of the assumption that the velocity of the falling dipole is low.

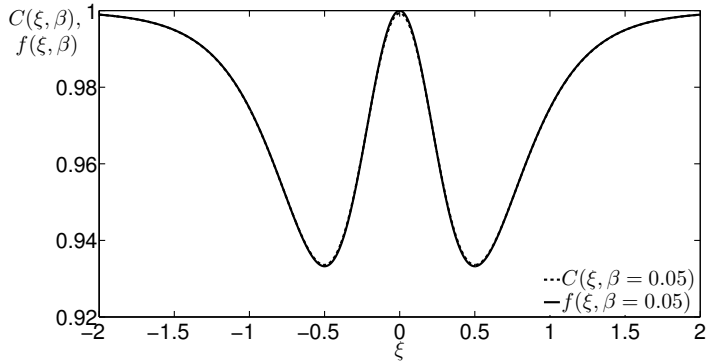

(a)

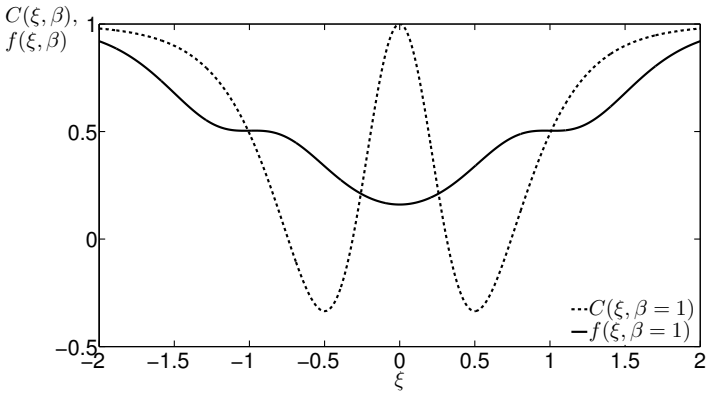

(b)

Figure 3.6: Comparison of the position-dependent perturbations of the motion dynamics between the complete solution and the NDA, where $\alpha = 0.0592$ and
(a) $\beta = 0.05$ (the perturbations are almost identical),
(b) $\beta = 1$ (the perturbations are strongly different).

The exact closed-form solution of a nonlinear differential equation as Eq. (3.38) is usually not possible. In order to emphasize the nonlinearity, Eq. (3.38) can be rewritten as

$$\ddot{\xi} + \dot{\xi} + \beta\, D\,(\xi)\; \dot{\xi} = \alpha, \tag{3.41}$$

where $D\,(\xi)$ is the nonlinear term

$$D\,(\xi) = -\frac{256}{5\,\pi}\;\frac{\xi^2}{(1+\xi^2)^5}. \tag{3.42}$$

Besides numerical methods there are asymptotic methods which engineers apply in order to approximate the solution of nonlinear differential equations for small perturbations, i. e., $\beta \ll 1$. Two well-known methods are the averaging method and the perturbation method. Whereas the averaging method is approximating the solution on a large range of the solution variable, the perturbation method is providing an approximation as a finite Taylor expansion of the exact solution at a certain point [85].

In order to study the effect of a small defect perturbation $\beta \ll 1$ the perturbation method is applied. Suppose that $\dot{\xi}(\tau,\, \beta)$ is continuous and has continuous partial derivatives. Additionally, suppose that there exists a unique solution $\xi(\tau,\, 0)$ which is referred to as the nominal problem and represents the pipe without defect. Thus, the solution of the differential equation Eq. (3.41) $\xi(\tau)$ can be displayed in a series of expansions

$$\xi(\tau) = \xi^{(0)}(\tau) + \beta\, \xi^{(1)}(\tau) + O\left(\beta^2\right), \tag{3.43}$$

where $\xi^{(0)}(\tau)$ is the zeroth order perturbation, i. e. no defect, and $\xi^{(1)}(\tau)$ the first order perturbation and the remaining error is in the order of $O(\beta^2)$.

In order to derive the differential equation that describes the first order perturbation, Eq. (3.43) has to be applied to Eq. (3.25). Therefore, all derivatives of $\xi(\tau)$ are needed:

$$\xi = \xi^{(0)} + \beta\,\xi^{(1)} + O\left(\beta^2\right), \tag{3.44}$$

$$\dot{\xi} = \dot{\xi}^{(0)} + \beta\,\dot{\xi}^{(1)} + O\left(\beta^2\right), \tag{3.45}$$

$$\ddot{\xi} = \ddot{\xi}^{(0)} + \beta\,\ddot{\xi}^{(1)} + O\left(\beta^2\right). \tag{3.46}$$

Applying Eqs. (3.44), (3.45) & (3.46) to Eq. (3.38) the resulting equation of motion is written as

$$\begin{aligned}\ddot{\xi}^{(0)} + \beta\,\ddot{\xi}^{(1)} \\ + \left[1 - \frac{256\,\beta}{5\,\pi}\,\frac{\left(\xi^{(0)} + \beta\,\xi^{(1)}\right)^2}{\left(1 + \left(\xi^{(0)} + \beta\,\xi^{(1)}\right)^2\right)^5}\right]\left(\dot{\xi}^{(0)} + \beta\,\dot{\xi}^{(1)}\right) \\ + O(\beta^2) = \alpha.\end{aligned} \tag{3.47}$$

Finally, Eq. (3.47) can be rewritten with an accuracy of β^2 as

$$\ddot{\xi}^{(0)} + \beta\,\ddot{\xi}^{(1)} + \dot{\xi}^{(0)} + \beta\,\dot{\xi}^{(1)} - \frac{256\,\beta\,{\xi^{(0)}}^2}{5\,\pi\,\left(1 + {\xi^{(0)}}^2\right)^5}\,\dot{\xi}^{(0)} = \alpha. \tag{3.48}$$

Comparing the coefficients the terms containing the zeroth order perturbation term $\xi^{(0)}$ and first order perturbation term $\xi^{(1)}$ are sorted according to Eq. (3.43). The following equations are obtained:

$$\ddot{\xi}^{(0)} + \dot{\xi}^{(0)} = \alpha \tag{3.49}$$

with the initial conditions

$$\xi^{(0)}\left(\tau = 0\right) = \xi_0, \tag{3.50}$$

$$\dot{\xi}^{(0)}\left(\tau = 0\right) = \alpha, \tag{3.51}$$

where ξ_0 is the starting position, and

$$\ddot{\xi}^{(1)} + \dot{\xi}^{(1)} = \frac{256\,\left(\xi^{(0)}\right)^2}{5\,\pi\,\left(1 + {\xi^{(0)}}^2\right)^5}\,\dot{\xi}^{(0)} \tag{3.52}$$

with the initial conditions

$$\xi^{(1)}\left(\tau = 0\right) = 0, \tag{3.53}$$

$$\dot{\xi}^{(1)}\left(\tau = 0\right) = 0. \tag{3.54}$$

The differential equation of motion for the zeroth order perturbation represents the case of a nondefective pipe. The general solution is

$$\xi^{(0)}(\tau) = C_1\,e^{-\tau} + C_2 + \alpha\,\tau, \tag{3.55}$$

where C_1 and C_2 are integration constants. When solving this equation for the initial conditions according to Eqs. (3.50) & (3.51), the solution of the zeroth order perturbation is obtained

$$\xi^{(0)}(\tau) = \alpha\,\tau + \xi_0. \tag{3.56}$$

Inserting Eq. (3.56), which is the solution of Eq. (3.49), into Eq. (3.52) leads to the differential equation of motion for the first order perturbation. This represents the motion dynamics of the magnetic dipole in the narrow defect region:

$$\ddot{\xi}^{(1)} + \dot{\xi}^{(1)} = \frac{256\,\left(\alpha\,\tau + \xi_0\right)^2}{5\,\pi\,\left(1 + \left(\alpha\,\tau + \xi_0\right)^2\right)^5}\,\alpha. \tag{3.57}$$

Equation (3.57) together with Eq. (3.43) shows that the magnet is accelerated when entering the defect region, but it is decelerated by the Lorentz force again when leaving the defect region. This leads to the typical M-shape phase diagram that has been already obtained in the exact solution of Eq. (3.25) (cf. Figs. 3.7a & 3.7b).

Equation (3.57) is a linear inhomogeneous differential equation of second order. A full analytical solution of the NDA equation can be found using Green functions. The full expression is lengthy and can be calculated using mathematical software tools as `Maple`.

Note, that the validity of the NDA is only given for $\beta \ll 1$. In Fig. 3.6 one finds the comparison of the friction terms. Figure 3.6a shows the case when $\beta \ll 1$. As a consequence the approximation and the complete solution $f(\beta, \tau)$ are almost identical. In Fig. 3.6b the opposite case is shown where $\beta = 1$. The shape of the complete solution is changing significantly, whereas the NDA is keeping the M-shape constantly and only the magnitude is changing as can be expected from Eq. (3.40). The resulting error is big and therefore, the NDA is not valid anymore.

A changing velocity α does not have much influence on the difference between the full and the NDA solution (see Fig. 3.7a), whereas the comparison in Fig. 3.7b shows the difference in magnitude for higher β. Nevertheless, the NDA is a good approximation of the complete solution for small β that allows to save computational time since the position dependent integration is avoided.

Large defect approximation

For large defects ($\beta \gg 1$) an approximation is possible as well, which is referred to as the large defect approximation (LDA). For this approximation the dipole is assumed to be sufficiently far away from the edges of the pipe. Without the edge effects the magnetic dipole reaches equilibrium velocity, i. e. it is falling with a constant velocity v_0.

The path of the dipole along the pipe is divided into three parts: first part of the pipe (index U(pper)), free fall (index M(iddle)), second part of the pipe (index L(ower)). Considering the three parts of the pipe the differential equations of motion of the magnetic dipole for each part can be formulated according to

$$\ddot{\xi}_U + \dot{\xi}_U = \alpha, \tag{3.58}$$

$$\ddot{\xi}_M = \alpha, \tag{3.59}$$

$$\ddot{\xi}_L + \dot{\xi}_L = \alpha, \tag{3.60}$$

assuming that the magnet is falling with the equilibrium velocity v_0 in the pipe parts U and L, whereas the magnet does not experience any braking Lorentz force in the pipe part M.

The general solutions of the differential equations of motion are given as

$$\xi_U(\tau) = -C_1\, e^{-\tau} + \alpha\,\tau + C_2 \tag{3.61}$$

$$\xi_M(\tau) = \frac{\alpha}{2}\,\tau^2 + C_3\,\tau + C_4 \tag{3.62}$$

$$\xi_L(\tau) = -C_5\, e^{-\tau} + \alpha\,\tau + C_6, \tag{3.63}$$

where C_i, $i = 1 \ldots 6$ are integration constants. These constants have to be determined in such a way that they satisfy the given initial and continuity conditions of the investigated problem.

At the starting time the magnetic dipole is placed at a certain starting position ξ_0 and moving with equilibrium velocity v_0 that corresponds, in nondimensional values, to the forcing parameter α. The initial conditions for the motion start are given as

$$\xi_U(\tau = 0) = \xi_0, \tag{3.64}$$

$$\dot{\xi}_U(\tau = 0) = \alpha. \tag{3.65}$$

The magnetic dipole reaches the boundary between the upper and the middle part of the pipe at the nondimensional time instant τ_{U-M}. In order to satisfy the continuity of the motion the position is $-\beta$ and the velocity is unchanged when approaching the intersection point from both directions:

$$\xi_U\left(\tau=\tau_{U-M}\right)=-\beta, \tag{3.66}$$
$$\xi_M\left(\tau=\tau_{U-M}\right)=-\beta, \tag{3.67}$$
$$\dot{\xi}_U\left(\tau=\tau_{U-M}\right)=\dot{\xi}_M\left(\tau=\tau_{U-M}\right). \tag{3.68}$$

Accordingly the boundary between the middle and the lower part of the pipe is at the nondimensional time instant τ_{M-L}:

$$\xi_M\left(\tau=\tau_{M-L}\right)=\beta, \tag{3.69}$$
$$\xi_L\left(\tau=\tau_{M-L}\right)=\beta, \tag{3.70}$$
$$\dot{\xi}_M\left(\tau=\tau_{M-L}\right)=\dot{\xi}_L\left(\tau=\tau_{M-L}\right). \tag{3.71}$$

As a result of the stated boundary and continuity conditions the equation of motion of the magnetic dipole is obtained. Thus, the exact solution of Eqs. (3.58), (3.59) & (3.60) is an approximation of Eq. (3.25) for large defects:

$$\xi(\tau)=\begin{cases}\alpha\,\tau+\xi_0, & (0\le\tau\le\tau_{U-M})\\[2ex] \frac{\alpha\,\tau^2}{2}+(\alpha+\beta+\xi_0)\,\tau & \\ \qquad+\frac{\beta^2+2\,\beta\,\xi_0+\xi_0^2+2\,\xi_0\,\alpha}{2\,\alpha}, & (\tau_{U-M}\le\tau\le\tau_{M-L})\\[2ex] -\frac{\left(\sqrt{\alpha^2+4\,\alpha\,\beta}-a\right)}{e^{\frac{\alpha+\xi_0+\beta-\sqrt{\alpha^2+4\,\alpha\,\beta}}{\alpha}}}\,e^{-\tau} & \\ \qquad+\alpha\,\tau+2\,\beta+\xi_0, & (\tau\ge\tau_{M-L})\end{cases} \tag{3.72}$$

where the intersection points between the pipe parts are marked by the nondimensional time instants:

$$\tau_{U-M} = -\frac{\beta - \xi_0}{\alpha}, \tag{3.73}$$

$$\tau_{M-L} = -1 - \frac{\beta + \xi_0}{\alpha} + \sqrt{1 + \frac{4\,\beta}{\alpha}}. \tag{3.74}$$

The approximation of the full equation of motion is capturing the general behavior of the magnetic point dipole falling through a pipe with defect. Due to the simplifications and the ansatz using continuity conditions the path of the dipole is different in the defect region. The characteristic M-shape of the phase curve is not captured (see Figs. 3.8a & 3.8b). But nevertheless, the LDA is an approximation of the complete solution of the ordinary differential equation of motion that is especially useful when the free fall is dominating. Using LDA it is possible to save computational costs since only the calculation of linear and quadratic equations is needed and it allows to determine defect sizes and to estimate falling times as well.

Experimental validation of the analytical model

In order to validate the presented analytical model a model experiment of the investigated problem has been performed. A spherical permanent magnet (NdFeB) has been dropped through a copper pipe and the falling time has been measured. All necessary geometrical and material properties have been measured according to Table 3.1. Due to the fact that the measurements have been carried out with a stop watch the reaction time has also been determined as $t_{react} = 324 \pm 10$ ms.

The experiments have been performed with two permanent magnets of different diameter. There have been done forty runs for each magnet which allows the investigation of random errors following the guideline [86]. The experimental data are shown in Table 3.2, together with the

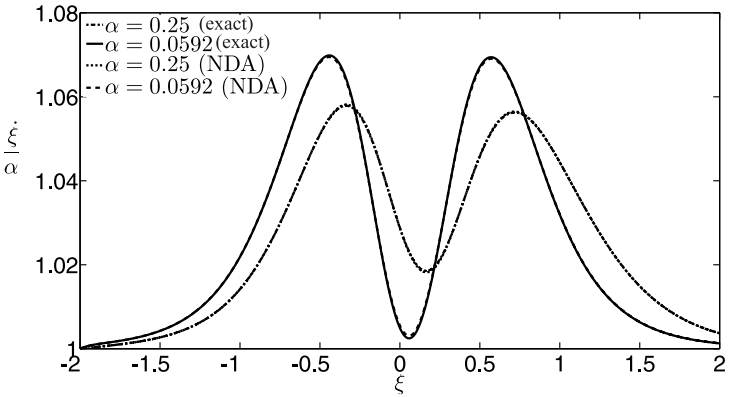

(a)

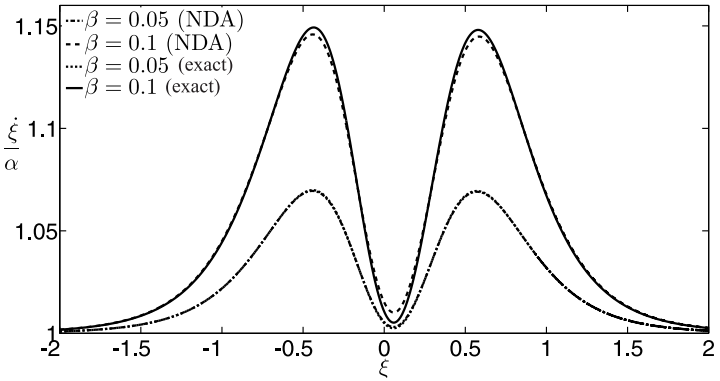

(b)

Figure 3.7: NDA, velocity distribution in the defect region: comparison between approximation and exact solution of Eq. (3.25)
(a) $\beta = 0.05$, different α,
(b) $\alpha = 0.0592$, different β.

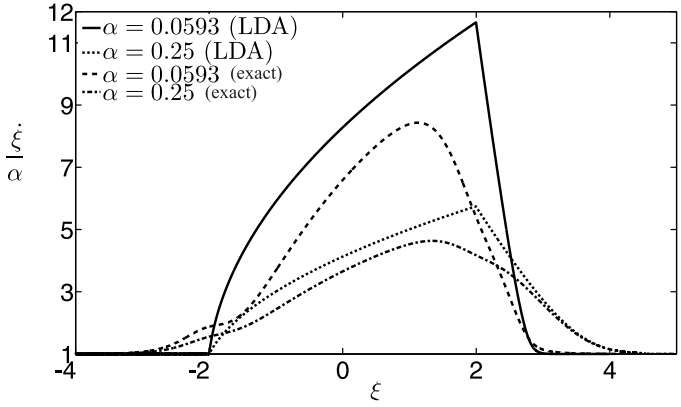

(a)

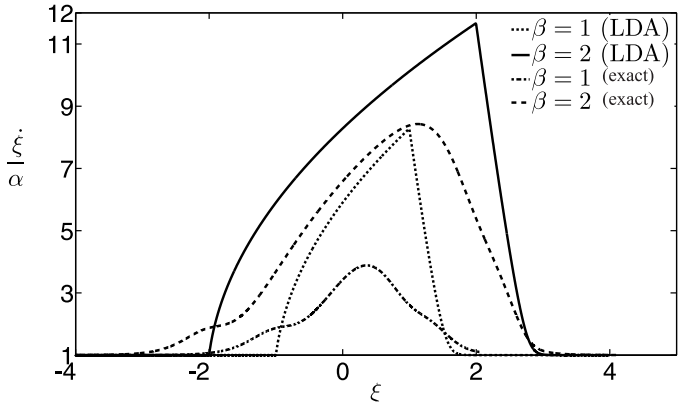

(b)

Figure 3.8: LDA, velocity distribution in the defect region: comparison between approximation and exact solution of Eq. (3.25)
(a) $\beta = 2$, different α,
(b) $\alpha = 0.0592$, different β.

Table 3.1: Geometrical and material properties of the "creeping magnet" experiment

Parameter	**Value**
Pipe radius R	8 cm
Pipe length L	1.001 m
Wall thickness δ	1 mm
Conductivity σ	$4.45 \cdot 10^7\ \Omega^{-1}\,\mathrm{m}^{-1}$
Magnet radius 1 R_{mag}	7.5 mm
Magnet radius 2 R_{mag}	5 mm
Magnet density ρ	7588.85 kg $^{-3}$m
Permeability μ	$4\,\pi \cdot 10^{-7}\ \mathrm{V\,s\,A^{-1}\,m^{-1}}$
Magnetic dipole moment density $\lvert\vec{m}\rvert$	$0.9054 \cdot 10^6\ \mathrm{A\,m^{-1}}$

absolute errors $|e|$ comparing the calculated falling time using Eq. (3.25) with the experimentally measured falling time:

$$|e| = \frac{|t_{exp} - t_{anl}|}{t_{exp}} \cdot 100\% \tag{3.75}$$

To record the time changes caused by an ideal defect, a pipe with changeable defect size has been build up. To minimize the perturbation, a mechanical nonmagnetic and nonconducting guidance has been applied. The flight time should increase linearly with the defect size according to Eq. (3.37). The dependency has been validated with Fig. 3.9. The slope differs from the analytical one because of the difference in the forcing parameter α. Additionally, the errors in time measurement for the experimental data have to be taken into account.

The difference between the presented solutions of the analytical approach and the experiments normalized by the analytical solution are shown in the subplots of Fig. 3.9. Due to higher speed, the error of the measurements with the 5 mm-magnet is larger and the gradient of the

Table 3.2: Experimental validation for a pipe with ideal defect: error estimation between measured and analytically calculated falling times

defect	**length of pipe**	t_{exp}	$\|e\|$
$R_{mag} = 7.5$ mm			
0 mm	0.8535 m	10.32 ± 0.09 s	22.70%
2 mm	0.8735 m	10.23 ± 0.08 s	22.45%
4 mm	0.8935 m	10.20 ± 0.09 s	22.89%
6 mm	0.9135 m	10.15 ± 0.11 s	23.45%
8 mm	0.9335 m	10.00 ± 0.11 s	25.30%
12 mm	0.9735 m	10.03 ± 0.07 s	24.95%
$R_{mag} = 5$ mm			
0 mm	0.8535 m	2.77 ± 0.06 s	27.10%
2 mm	0.8735 m	2.81 ± 0.06 s	32.73%
4 mm	0.8935 m	2.79 ± 0.06 s	33.96%
6 mm	0.9135 m	2.82 ± 0.06 s	32.42%
8 mm	0.9335 m	2.80 ± 0.06 s	33.57%
12 mm	0.9735 m	2.74 ± 0.06 s	36.15%

graph is bigger than that of the 7.5 mm-magnet. The linear behavior of Eq. (3.35) has been found in the numerical results as well [76].

The effect of a finite magnetic Reynolds number R_m

The effect of the secondary magnetic field has been neglected in the presented model. Naturally, it is reasonable to expect that the conductor slightly perturbs the magnetic field of the magnetic dipole. To satisfy this extended model the magnetic flux density $\vec{B}$ in the presence of a moving conductor has to be described by the induction equation. The ratio between the magnetic advection and the magnetic diffusion

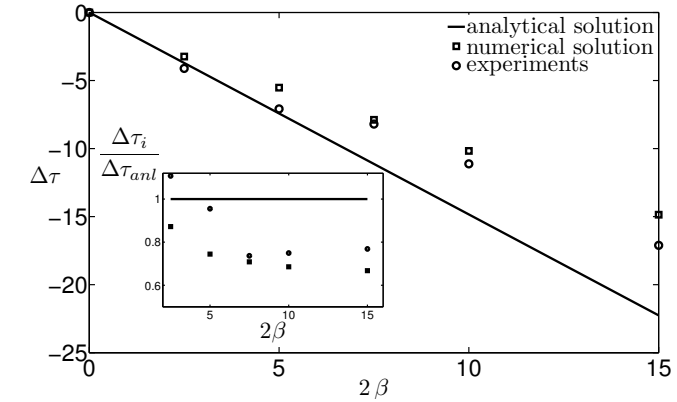

(a)

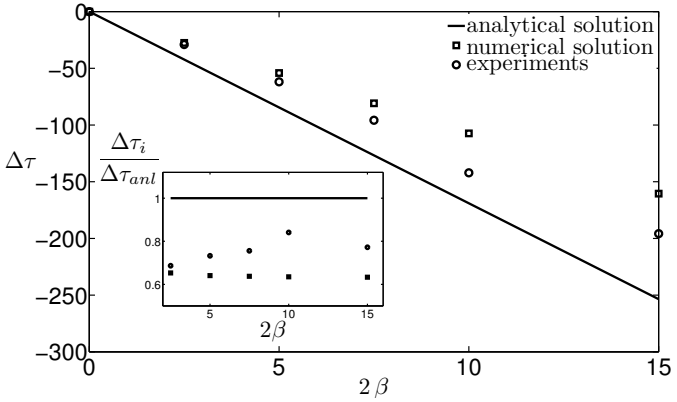

(b)

Figure 3.9: Comparison of experimental data with analytical and numerical [76] obtained falling time changes $\Delta\tau$,
(a) magnet $R_{mag} = 5$ mm, subplot: compensated plot,
(b) magnet $R_{mag} = 7.5$ mm, subplot: compensated plot.

is described by a nondimensional quantity referred to as the magnetic Reynolds number R_m [87, 88]:

$$R_m = \mu_0 \, \mu_r \, \sigma \, v \, L, \tag{3.76}$$

where L is a characteristic length and v the relative velocity.

A low magnetic Reynolds number $R_m \ll 1$ describes the situation when the diffusion of the magnetic field is dominating over transient and convecting effects. Then the magnetic field transport equation [87, 88] becomes a diffusion equation and the magnetic field stays unperturbed within the vicinity of a moving conductor (cf. Figs. 3.10a – 3.10c).

In the case of a high magnetic Reynolds number $R_m \gg 1$, the convection of the magnetic field is stronger than its diffusion and the magnetic field is strongly perturbed by the relative motion of the conductor. As a result, the magnetic field is gradually expelled from the conductor (cf. Figs. 3.10g, 3.10h & 3.10i). This effect is referred to as the skin effect.

The analytical model which has been presented here is valid for $R_m \ll 1$ only. Taking into account the deformation of the field lines, a numerical solution of the induction equation together with Eq. (3.17) is required. A more extensive study including numerical investigations on the "creeping magnet problem" can be found in [76].

3.2 Lorentz Force Eddy Current Testing

In difference to the rather academic model in Sec. 3.1, the more general case of the so-called Lorentz force eddy current testing problem cannot be treated analytically. Thus, this case will be only shortly discussed. A permanent magnet falling through a vertical pipe is not a wide spread technical application. The investigation on the applica-

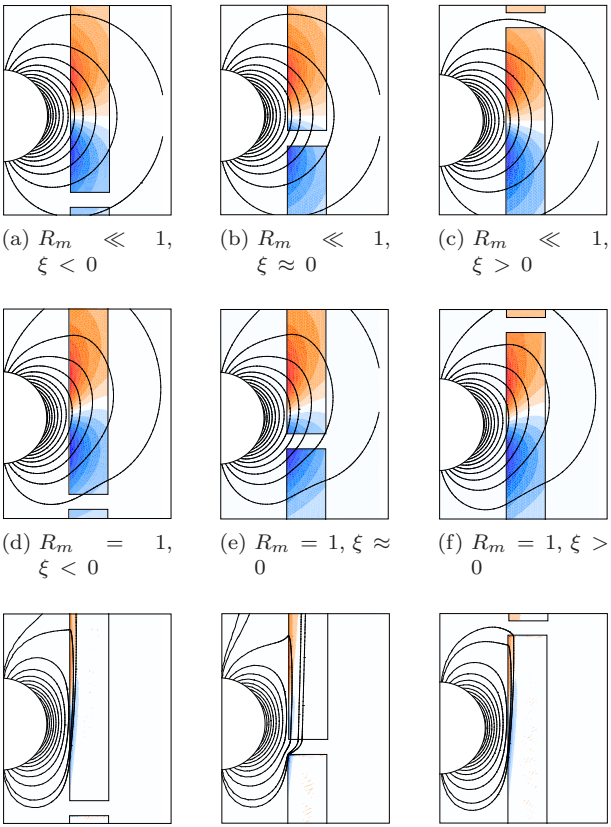

(a) $R_m \ll 1$, $\xi < 0$ (b) $R_m \ll 1$, $\xi \approx 0$ (c) $R_m \ll 1$, $\xi > 0$

(d) $R_m = 1$, $\xi < 0$ (e) $R_m = 1, \xi \approx 0$ (f) $R_m = 1, \xi > 0$

(g) $R_m \gg 1$, $\xi < 0$ (h) $R_m \gg 1$, $\xi \approx 0$ (i) $R_m \gg 1, \xi > 0$

Figure 3.10: Influence of the magnetic Reynolds number R_m on the magnetic field distribution. The magnet is moving down, using $\alpha_{a,b,c} = 0.4078$ ($R_m = 0.01$), $\alpha_{d,e,f} = 4.078 \cdot 10^3$ ($R_m = 1$), $\alpha_{g,h,i} = 4.078 \cdot 10^7$ ($R_m = 100$) and $\beta = 0.125$. Courtesy of Dipl.-Ing. Mladen Zec.

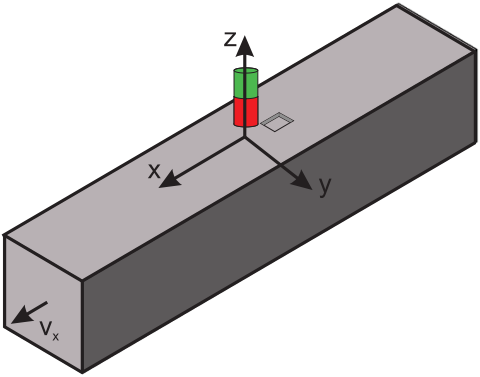

Figure 3.11: Conductor of finite dimensions with an artificial surface defect in the vicinity of a permanent magnet.

bility of Lorentz force eddy current testing to plates, bars and other more complex geometries is useful. In order to study more complex geometries the problem is transformed into a different albeit physically similar configuration where a conductor of finite dimensions is moving in the vicinity of a permanent magnet (see Fig. 3.11). The problem is not axisymmetric and is not solvable analytically. An semi-analytical approach of solving this configuration using a dipole approximation instead of the magnet is found in [69] even though the investigated parameters are outside a measurable range.

As a consequence, the defect is not detected and localized by time measurement anymore but by measuring the force acting on the permanent magnet. Whereas a conductor without any defect provides a constant force signal (analogue to the constant falling velocity of the creeping magnet), defects will cause perturbations in the force signal. Experiments of an early stage of the investigations on Lorentz force eddy current testing are presented in [8]. There, a long conductive rod with

many huge artificial defects has been moved. The goal has been to prove the possibility of defect detection with force measurements.

In order to provide an alternative to applications of the classical eddy current testing, the limits of the detection have to be exceeded in terms of depth and size of the defect. The main reason for applying permanent magnets in Lorentz force eddy current testing is the potential increase in depth in which a defect can be detected. Furthermore, the higher testing velocity can be advantageous.

The application of direct (DC) magnetic fields has a big advantage compared with alternating (AC) magnetic fields. Due to the lack of source frequencies, the magnetic field penetrates the conductor under test to a much greater depth. A measure of the field displacement is the so-called skin depth [62]. The skin depth δ_{skin} is the depth in which the magnetic field strength has weakened by a factor of $e^{-1} \approx 36\%$ compared to the value at the surface of the conductor. The classical notation is well-known from alternating current applications:

$$\delta_{skin} = \sqrt{\frac{1}{\pi\, f\, \mu_0\, \mu_r\, \sigma}}, \tag{3.77}$$

where f represents the source frequency and μ_r is the relative permeability of the conductor. For high frequencies, the field is expelled strongly from the conductor as in the case of a high magnetic Reynolds number. This physical effect limits the classical eddy current testing in terms of detection depth to a few millimeters for practical applications. However, there are satisfactory improvements in the detection of deep lying defects with classical eddy current testing down to 28 mm applying low frequencies and special coil configurations [32]. In order to overcome the frequency dependent practical limitation, the application of permanent magnets is considered.

It is obvious that the skin depth has to be defined in a different manner when applying the model to a permanent magnet in the vicinity of a linearly moving conductor. However, using a characteristic frequency

in terms of velocity and characteristic length scale according to $2\,\pi\,f = v/L$, a motional skin depth can be defined [62]:

$$\delta_{msd} = \sqrt{\frac{2\,L}{\mu_0\,\mu_r\,\sigma\,v}}. \tag{3.78}$$

The achieved skin depths using a permanent magnet exceed by far the limitation of alternating current driven techniques. The estimated motional skin depth is one order of magnitude higher. A comparison with usually used values is presented in Fig. 3.12 [13].

In order to prove the basic idea and the presented physical effects, a model experiment has been performed. It will be discussed in the following chapters. The investigation can be compared with results from studies of magnetic levitation [28, 61, 62]. Since the physical effects are the same in both applications, there is a good opportunity to verify the experimental results for the low and medium R_m-range.

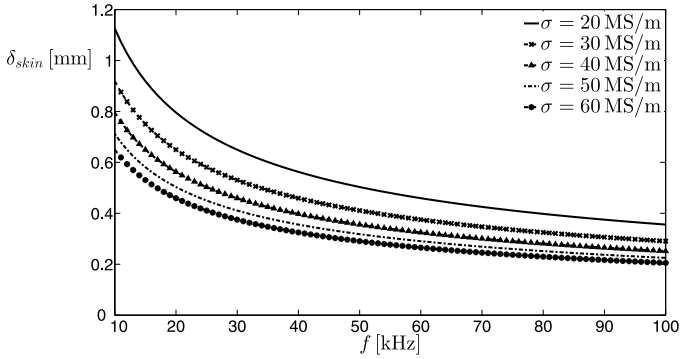

(a)

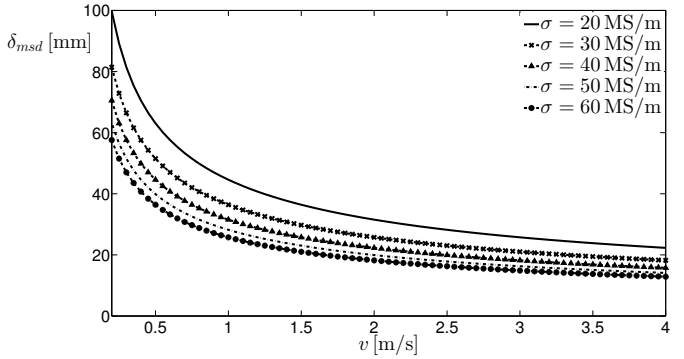

(b)

Figure 3.12: Comparison of calculated skin depths considering different conductors for
(a) classical eddy current testing in the frequency range of $f = 10 \ldots 100$ kHz
(b) Lorentz force eddy current testing for a characteristic length scale of $L = 25$ mm and in the velocity range of $v = 0.2 \ldots 4$ m/s.

4 Measurement Apparatus

In this chapter the used equipment for the measurement apparatus is described. The functional structure of the measurement setup is discussed in order to understand the interaction between the components. The description starts with the functional analysis of the measurement setup. This analysis is providing general ideas which led to the constructive realization. A more detailed introduction into the used devices is given afterwards. Calibration data and required parameters for the operation of the measurement setup are summarized. The alignment procedure is discussed at the end of this chapter to cover the basics for the following topics that focus mainly on measurements and their results.

4.1 Functional Analysis

The main demand to a working measurement setup for Lorentz force eddy current testing is the application of a permanent magnet or magnet system which is in relative motion to an electrically conducting, nonmagnetic specimen. The relative motion can be realized in three different ways: (i) the magnet is moving while the specimen is at rest, (ii) the specimen is moving while the magnet is at rest and (iii) both magnet and specimen are moving in different, most likely opposite direction. Due to the effect of inertia the variant (ii) has been chosen. The mass of the magnet is much smaller than the specimen's. Due to the necessity of high dynamic force measurements a small mass is guaranteeing a higher eigen frequency which is preferable for measurements as will be discussed later on.

The motion has been chosen to be linear instead of rotary to ensure a wider variety of specimen and to provide data which are more relevant

to industrial applications. A sketch of the setup consisting of the main components is shown in Fig. 4.1. As a result, the functional structure according to Fig. 4.2 shows the physical links between the components of the measurement setup.

The operator has to provide data about the position of the magnet relative to the specimen and the velocity in x-direction v_x (cf. Fig. 3.11). The position of the magnet is defined by the lift-off distance δz and the lateral displacement δy (cf. Fig. 4.3).

The given data are transfered to the control unit which supplies all active parts of the measurement setup with electrical energy (not shown in Fig. 4.2). The electrical energy supplied to the motor of the drive system is a function of the necessary number of turns that is calculated according to the predetermined velocity. The motor provides the current number of turns from which the applied velocity can be calculated. The position of the magnet or magnet system is attained by a y-z-positioning stage that is controlled by position-dependent currents. The stage is fixed to the measurement frame that stands on the foundation (cf. Fig. 4.4).

The rotary motion of the motor is transformed to a linear motion with the help of a pinion and a tooth belt. Since the number of turns at the motor output is too high, it has to be decreased with a planetary gear. The driven tooth belt is fixed to a sledge on which the specimen is mounted. The guidance of the linear axis is fixed to a C-profile that is placed on the foundation and guides the movement of the specimen through the magnetic field $\vec{B} = \mathbf{B}$ (cf. Fig. 4.2) created by the magnet system. As a result of the generated eddy currents, the Lorentz force according to Fig. 4.3a is acting on the magnet system (see Ch. 6). The Lorentz force is detected by a 3D force sensor which is providing a force-dependent voltage to the control unit. The force sensor is fixed to the y-z-positioning stage and thus, to the magnet. As a result, the operator can read the value of the acting Lorentz force at the control unit.

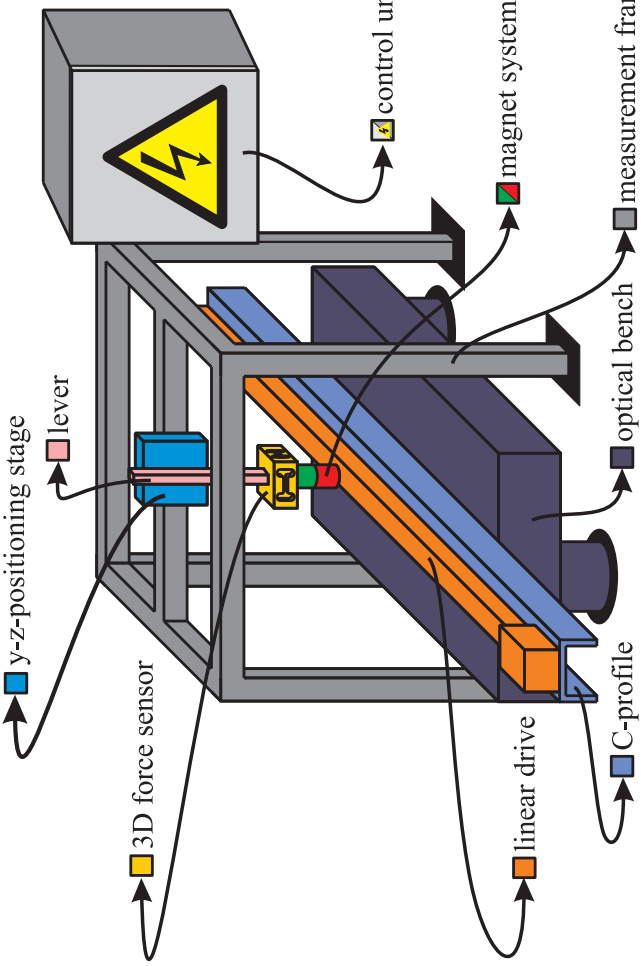

Figure 4.1: Sketch of the proposed and investigated Lorentz force eddy current testing measurement setup with all main components.

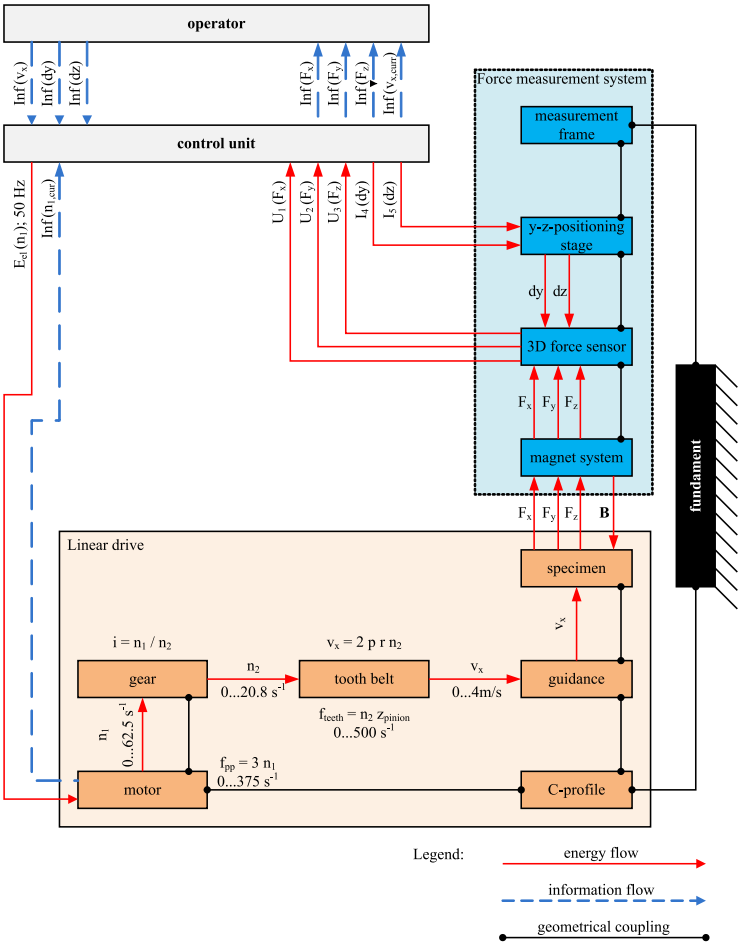

Figure 4.2: Functional structure of the measurement apparatus including all interfaces showing energy and information flows, control parameters and sources of noise, taken from [89] and translated.

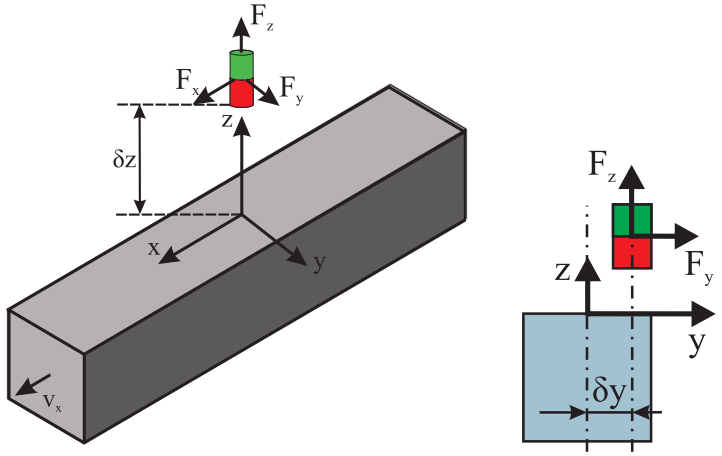

(a) (b)

Figure 4.3: Main parameters of the Lorentz force eddy current testing measurement setup:
(a) lift-off distance δz and measured Lorentz force components F_x, F_y, F_z,
(b) lateral displacement δy and force components (front view).

(a)

(b)

Figure 4.4: Assembled measurement setup:
(a) total view without data acquisition unit,
(b) detail view on force sensor.

4.2 Devices

The measurement principle of Lorentz force eddy current testing needs only a small number of components. There are four main components of the system, i. e. (i) the linear drive to provide the relative motion, (ii) the y-z-positioning stage for the positioning of the magnet, (iii) the force sensor to measure the reaction force on the magnet and (iv) the data acquisition to acquire the raw data and provide them for signal processing.

4.2.1 Linear Drive

The specimen is set into motion using a linear belt driven drive by *Jenaer Antriebstechnik GmbH* on a *Bahr Modultechnik GmbH*-axis (see Fig. 4.5). The drive consists of a motor which is applying a rotational driving motion on a pinion. The high rotational speed of the motor is reduced using a planetary gear which provides a gear ratio of three. The pinion has 24 teeth and drives a tooth belt. In order to investigate a wide range of relative velocities, the drive supports velocities up to 4 m/s. The corresponding number of turns can be calculated using the parameters of the linear drive that are summarized in Table 4.1.

In order to guarantee an almost constant force, the velocity should not vary much. The manufacturer specifies that the predetermined velocity in the measurement region will not vary more than 5%. The measured force and the velocity of the internal position decoder have been compared. The velocity is affecting the force but is constant within the 5%-range. This fact could not be verified because an external velocity measurement system has not been available.

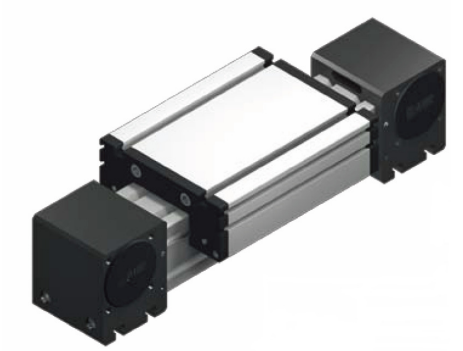

Figure 4.5: Exemplary photography of the used linear belt driven drive.

Table 4.1: Parameters of the used linear belt driven drive

Parameter	**Symbol**	**Value**
number of terminal pairs	-	3
rotational speed of rotational drive	n_1	$0 \ldots 62.5$ Hz
planetary gear ratio	$i = n_1/n_2$	3
rotational speed of planetary gear output	n_2	$0 \ldots 20.8$ Hz
pinion radius	r_{pinion}	30.56 mm
number of teeth per turn	z_{pinion}	24
belt velocity	$v_x = 2\,\pi\,r\,n_2$	$0 \ldots 4$ m/s

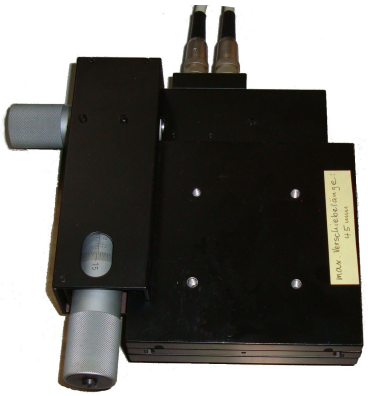

Figure 4.6: Photography of the used y-z-positioning stage (disassembled).

4.2.2 Positioning Stage

The position of the permanent magnet or magnet system is controlled precisely by the y-z-positioning stage. The positioning stage is a microscopic table manufactured by *Märzhäuser Wetzlar*, see Fig. 4.6. It provides a measurement range of 45 mm × 45 mm with a resolution and repeatability lower than 1 µm. The table has been turned by 90° in order to provide the accurate position in the y-z-plane.

The drives can be controlled electrically using the 2-phase step motors or manually. The electrical step motors are coupled to a spindle which is supported by ball bearings in order to transform the rotational motion into linear motion. To move the mass of the mounted magnet system, a gravity compensation with a mechanical spring is applied. The control unit of the stage *MC2000* has been addressed using the RS232-serial interface.

4.2.3 Force Sensor

The demand on a wide band basic investigation forced the use of a wide band force sensor. Since the Lorentz force is not only acting in movement direction but depending on the position of the permanent magnet in transversal and vertical direction as well, a 3D force sensor based on strain gauge technology by *ME Systeme GmbH* has been chosen. A huge advantage of strain gauge based force sensors are their relatively low costs and the good knowledge of the technology [90, 91]. The relatively low mechanical eigen frequency of the sensor is the main disadvantage because dynamic measurements are limited to a frequency which is close to the first eigen frequency of the deformation body of the sensor. According to the manufacturer's data sheet it corresponds to 180 . . . 60 Hz depending on the applied load.

Due to the need of dynamic measurement an amplifier with a limiting frequency of $f_{lim} = 10$ kHz has been chosen which means that signals that are changing with higher frequencies are damped stronger than 3 dB. So, the limiting frequency is given by the deformation body itself.

The manufacturer is providing a calibration for the sensor (see Table 4.2). Every channel has been carrying a load that has been approved by the National Institute of Metrology that is in Germany the Physikalisch Technische Bundesanstalt (PTB) in Braunschweig. The corresponding voltage is given in order to recalculate the force F_i as

$$F_i = U_{meas,i} \cdot \frac{F_{cal,i}}{U_{cal,i}}, \tag{4.1}$$

where $F_{cal,i}$ is the calibration load of the channel i, $U_{cal,i}$ the corresponding voltage and $U_{meas,i}$ the actual measured voltage.

In the given data sheet, the spring constant is not determined correctly [92]. Stating that the displacement of 0.07 mm is measured, the spring constant is calculated according to

Table 4.2: Calibration data of the used force sensor according to the manufacturer (ME Systeme GmbH)

Channel i	**applied load** $F_{cal,i}$	**measured voltage** $U_{cal,i}$
1	3 N	3.1969 V
2	3 N	4.8835 V
3	10 N	7.803 V

Table 4.3: Spring constants and deformations of the used force sensor

Channel i	**deformation at** $F_{N,i}$	**spring constant** c_i
1	0.07 mm	42.86 N/mm
2	0.07 mm	42.86 N/mm
3	0.07 mm	142.86 N/mm

$$c_i = \frac{F_{N,i}}{\Delta x_i} \quad , i = 1, 2, 3,$$

where $F_{N,i}$ is the maximum force acting in the direction of a channel i and Δx_i is the caused deflection. So, the spring constants in Table 4.3 are obtained.

The strain gauges are fixed to an aluminum deformation body. The deformation is forced at flexural hinges where stress and tension are measured with the help of a full bridge. Further data are given according to the data sheet [92].

4.2.4 Data Acquisition System

The data acquisition is done using a commercial PXI system by *National Instruments* (NI). The measurement computer provides real-time application, i. e. the guarantee to acquire data at a predetermined time taking waiting times into account. The voltage of the force

sensor amplifier is sampled by the 8-channel dynamic signal acquisition module *NI PXI-4472* simultaneously with a sample frequency $f_{sample} = 10\,\text{kHz}$. The Nyquist-Shannon sampling theorem [93, 94] ensures that signals with a frequency up to $f = 5\,\text{kHz}$ can be reconstructed. This is more than enough for the used force sensor and provides the possibility to improve the dynamics of the force sensor in future work.

The data acquisition unit is used for the automation of the whole measurement setup with the help of TCP/IP communication and serial RS232 interface. The programming language is *LabVIEW 2010* which has been developed by *NI*. The acquired raw data is stored on hard disk in binary file format. The transformation to text files is performed after the measurement due to the time critical writing on files. The binary format has been found to be faster and more reliable [95]. The text file is read with a script in *MATLAB 2009a* and converted to the *MATLAB*-native format .mat. The mat-file is processed with filters and stored on hard disk again. So the raw and filtered data are available for further use.

4.3 Assembly

The linear drive is mounted on a steel C-profile which is screwed to an optical bench. The optical bench consists of a steel frame which is filled with quartz sand around a massive granite block. The steel frame is situated on three circular feet on the linoleum covered concrete floor. The mass of the specimen is very small compared to that of the optical bench. Nevertheless, the high acceleration of $\ddot{x}(t) \leq 20\,\text{m/s}^2$ is inducing forces into the bench which is guiding them into the floor. A simplified and idealized sketch of the linear drive base is found in Fig. 4.7 whereas the assembled setup is shown in Fig. 4.4a.

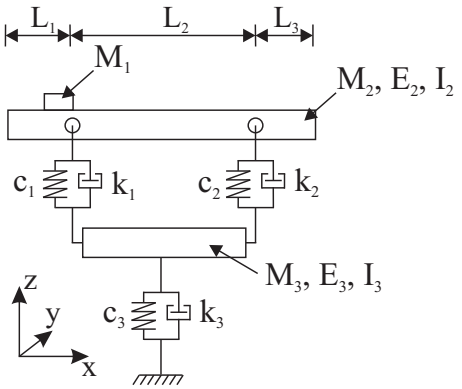

Figure 4.7: Scheme of the simplified mechanical model of the linear drive base comprising the linear drive (Index 1), the C-profile (Index 2) and the optical bench (Index 3). The unknown coupling elements are denoted with stiffnesses (c_i) and damping (k_i) elements.

The measurement frame is assembled from aluminum profiles standing next to the linear drive base on the linoleum covered concrete floor. The y-z-positioning stage is fixed to the aluminum frame with aluminum parts. A long rod which is mounted on the stage is carrying the force sensor on the bottom and is connected to the gravitational compensation on the top. The permanent magnet is screwed to a mounting adapter that is hanging at the force sensor.

All coupling elements between the single parts of the measurement setup are modeled by spring/damper systems in the mechanical model in Fig. 4.7. A big challenge is to determine the exact values of each spring and damper constant for every single coupling. Furthermore, there are effects of nonuniform contacts between the C-profile and the granite table. That is the main reasons for the difficulty of using multibody simulation to describe the dynamic behavior of the whole setup.

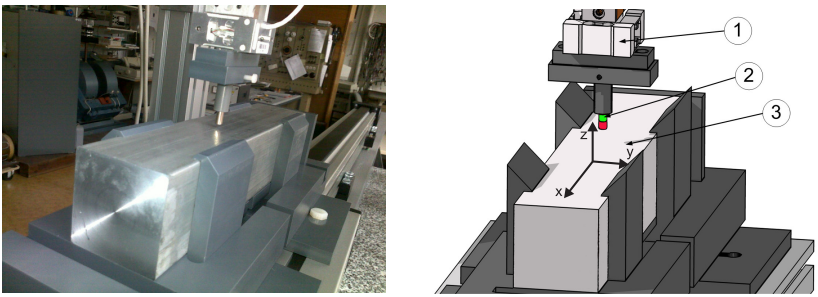

(a) (b)

Figure 4.8: Basic experimental setup comprising a (1) force sensor, (2) permanent magnet and (3) specimen,
(a) Photography,
(b) Sketch.

An experimental modal analysis combined with an analytical analysis will be demonstrated in Ch. 5.

Due to the fact that the permanent magnet is a free-hanging object, an alignment procedure is necessary to guarantee an exact position relative to the specimen.

4.4 Calibration and Alignment

The dimensions of the permanent magnet and the specimen have to be known. Without additional external sensors there exists the possibility to use the force sensor as a reference for the alignment procedure. This method is referred to as force feedback [96].

In the used measurement setup, the surface of the specimen can be touched from two sides by using the joystick control of the microscopic

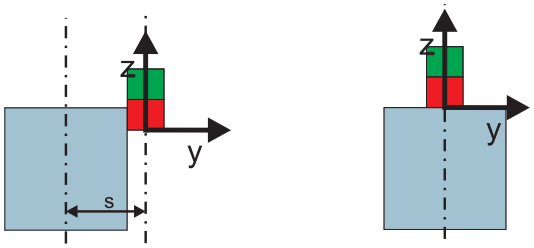

(a) (b)

Figure 4.9: Alignment procedure using force feedback on the permanent magnet:
(a) Contact from the side to obtain y-position (z unknown, offset s)
(b) Contact from top to obtain z-position (absolute zero, no offset).

table. In the real-time displayed voltage signal one can read when the voltage and so, the contact force is rising. Naturally, a movement without contact produces a noisy voltage signal around $U_{meas} = 0$ V. A sufficient contact has been established when the voltage crosses $U_{meas} = 0.1$ V.

The alignment has been performed for the y-axis first and then for the z-axis. So the absolute zero coordinate can be located in the longitudinal symmetry axis of the bar that allows to determine the system parameters lift-off distance δz and lateral displacement δy without any additional sensors (see Fig. 4.9). The contacting force causes a slight deformation of the force sensor which represents a systematic error in the position during measurements. The error can be calculated using the spring constants from Table 4.3.

The voltage of $U_{meas} = 0.1$ V corresponds to a force of $F_y = 61.43$ mN in y-direction and $F_z = 128.16$ mN in z-direction respectively. This force causes a deformation of approximately 1.43 µm in y-direction

and 0.90 µm in z-direction. The error is small and neglectable for the performed measurements. When using the system for close-to-surface measurements, an external position measurement system for the magnet position control is preferable because the sensitivity is increasing with decreasing lift-off distance as will be shown in Sec. 6.1.3.

5 Signal Processing

In measurement technologies, the signal quality is a very important aspect. It can be defined with the help of the so-called signal-to-noise ratio which implies to be rather low if the signal's quality is poor. In contrast, a high ratio describes a significant change in the Lorentz force magnitude compared to the existing noise. In order to study the influence of defects in metallic materials with the help of Lorentz force eddy current testing, the signal quality of the measurement apparatus has to be investigated and improved, if necessary. Since small changes in force have to be detected in short process times, the focus is on oscillation phenomena due to the fact that they are of significant importance for the high dynamic measurement technique.

5.1 Experimental Modal Analysis

A measured signal is influenced by a lot of unknown disturbances and effects. Filters are used to separate the measured signal from disturbances. In many publications the applied filter techniques rely on experimental-heuristic approaches or on handbook tables and are not explained well [90, 91]. Thus, the influence of applied filters on the measurement signal is often not exactly known. This implies obtaining signals that were expected without satisfying the application needs in filtering.

However, there is a big difference between measurements of low and high dynamic effects. Whereas averaging and other classical filter techniques can be applied to signals that are slowly changing in time, the demand on signals with reduced noise for high dynamic applications cannot be fulfilled. Thus, more sophisticated filter techniques have to be applied. As will be shown in the following, a significant improve-

ment of signal quality can be achieved taking care of the constructive realization and its influence on the system dynamics.

5.1.1 Operational Sequence

The influence of disturbances on the measured force signal has been investigated. Therefore, measurements under different environmental conditions are performed. The first measurements are performed completely without motion to make sure that the oscillations in the interesting range from environment without noise sources (e. g. motors) are captured. The advantage is that a time-invariant linear signal can be assumed which allows to use Fourier transformation to investigate the signal [97]. These measurements are referred to as zero measurements.

A further investigation contains the motion of the linear drive under running conditions but without the specimen. Again, Fourier transform can be used as a tool to process the assumed time-invariant linear signal. Since motion is inducing local effects on the measurement setup, the investigation is extended to the time-frequency domain using wavelet transformation. The big power of this approach is the determination of time-dependent changes in the frequency spectrum of the measured signal. Among mechanical engineers, this powerful tool whose origin is the file compression and denoising of acoustic signals is becoming increasingly important [97].

The last step in gathering system information is the oscillation analysis of the specimen in motion. Therefore, considerations in the time-frequency domain are strongly required. The specimen produces a clearly time-variant signal. Cutting time-invariant pieces would reduce the resolution of the Fourier spectrum which can be avoided by using windowed Fourier transform [98] or wavelet analysis. Due to the higher resolution for higher frequencies wavelets have been applied [99].

5.1.2 Zero Measurement

The separation of the measured signal from noise is quite easy when producing a signal that shall be zero. This has been done by recording the force signal without any motion. The signal contains actually no force (should be zero) but all the environmental and mechanical noise.

At the bottom of Fig. 5.1 the force signal in drag direction F_x is shown with respect to the time t. It is clear that there is a small offset in the force signal from the zero-line that can be corrected. There have been almost no impacts on the system. On the left hand side of Fig. 5.1, the standard Fourier transform of the signal can be found. As expected, the power frequency and its harmonics can be identified clearly. Additionally, there is a band of oscillation frequencies between 58 Hz and 98 Hz.

In order to investigate whether this disturbance is time-invariant or transient the time-frequency domain is shown in the center of Fig. 5.1. The color of the graph corresponds with the magnitude of the signal at a certain time t and frequency f, blue means no energy whereas red corresponds to high energy. The 50 Hz-line has low energy and one can find time-variant amplifications of the oscillation band between 0 s and 5 s and at 12.5 s as well as at 20 s.

The oscillations in the other two directions without movement are of lower magnitude (factor ten). In general the behavior is similar even though one cannot see the oscillation band between 58 Hz and 98 Hz as clearly as for the drag force. The signals of the y- and z-component of the force sensor are analyzed in Figs. 5.2 & 5.3 the same way as the drag force.

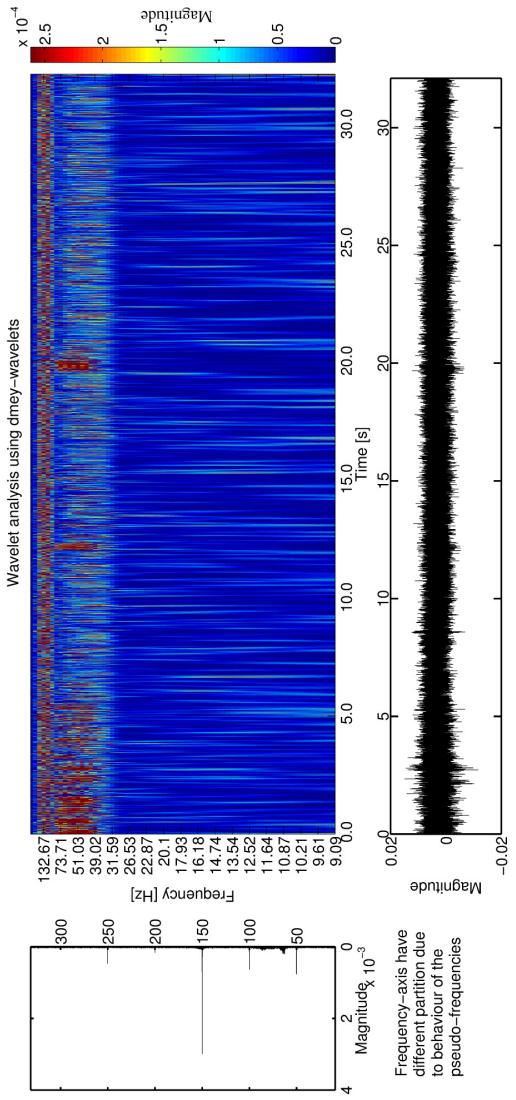

Figure 5.1: Oscillation measurement (bottom), wavelet- (center) and Fourier-analysis without motion: drag force F_x.

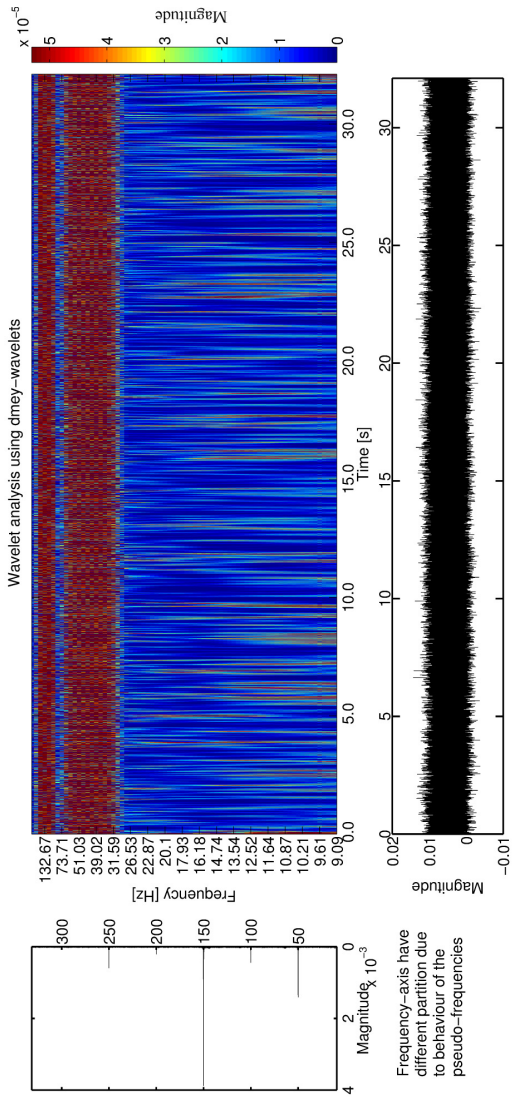

Figure 5.2: Oscillation measurement (bottom), wavelet- (center) and Fourier-analysis without motion: lateral force F_y.

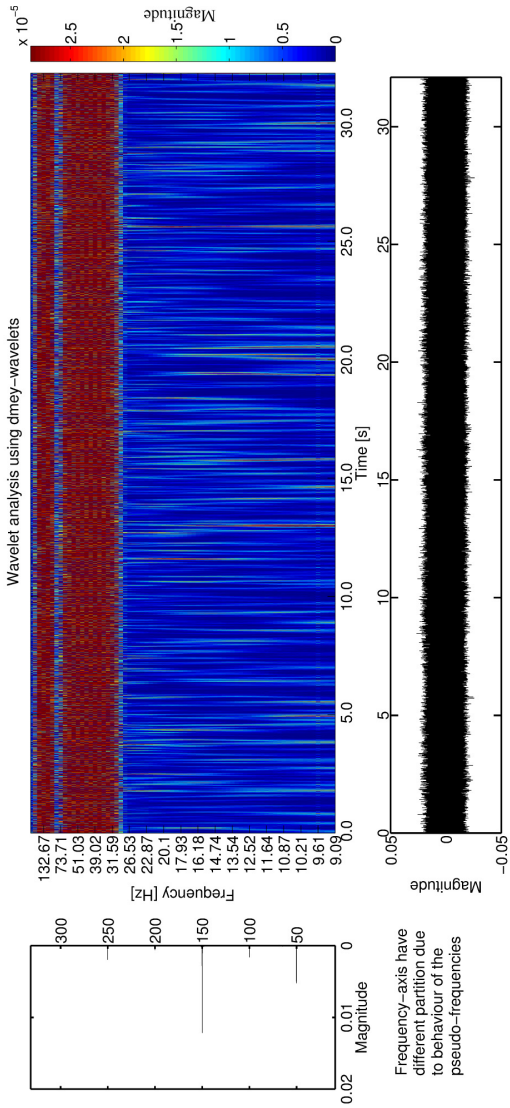

Figure 5.3: Oscillation measurement (bottom), wavelet- (center) and Fourier-analysis without motion: lift force F_z.

5.1.3 Motional Measurement

Without specimen

The zero-measurement provides information about environmental and natural oscillations. The next step is the determination of forced oscillations due to the motion of the linear drive. In order to create a time-invariant signal for the Fourier transform, the investigation has been performed without a specimen. So, the measured force should remain zero.

As one can find in Figs. 5.4 – 5.6 the motion of the linear drive is increasing the noise on the signal drastically. From the Fourier transform on the left hand side of all sub-figures the oscillation in a wide band between 50 Hz and 225 Hz can be found. On the time signal one can see time-variant resonance-like amplification in magnitude. Additionally, the wavelet-graph in the center of all sub-figures shows that there are several impacts, best to see at 2.6 s and 3.2 s and at 3.8 s as well as at 4.4 s in Fig. 5.4. Small influence of these impacts can be found in Fig. 5.6 at the same time instants.

The obtained signal is representing the zero-force during a measurement cycle. One measurement cycle means that the linear drive moves from one end point position to the other, forth and back. In Fig. 5.5 the motion phases of the linear drive can be determined in the wavelet-graph in the region of low frequencies.

With specimen

The last measure is to establish the remaining signal transmission path due to the influence of eddy currents. Therefore, the specimen is mounted on the linear drive and moved with same velocities as for the measurements before. The main impacts are the specimen edges. The Fourier transform suffers strongly from the time-variant signal. In this case, the power of signal processing procedures using the frequency-time domain is obvious.

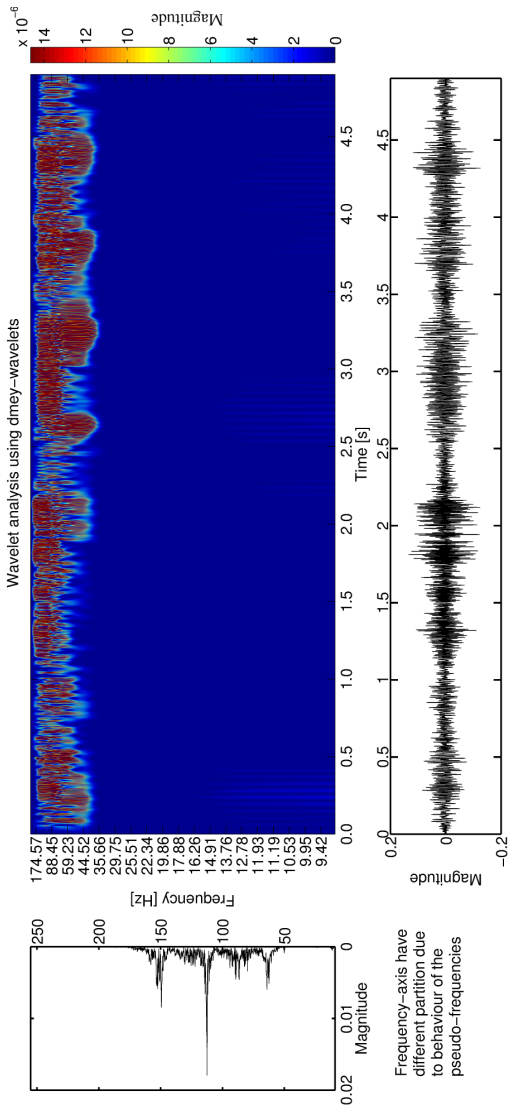

Figure 5.4: Oscillation measurement (bottom), wavelet- (center) and Fourier-analysis at velocity $v = 900$ mm/s and lift-off distance $\delta z = 1$ mm without specimen: drag force F_x.

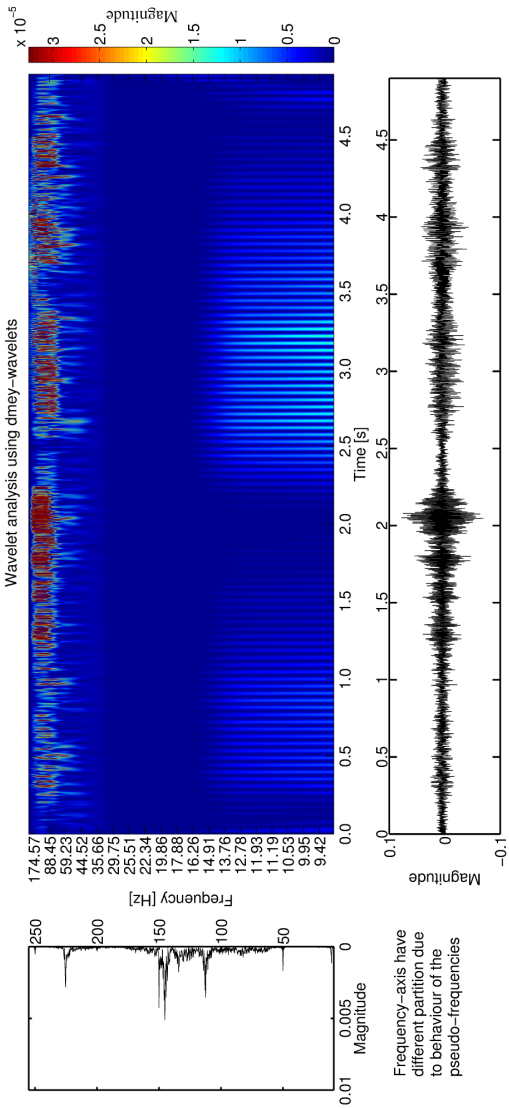

Figure 5.5: Oscillation measurement (bottom), wavelet- (center) and Fourier-analysis at velocity $v = 900$ mm/s and lift-off distance $\delta z = 1$ mm without specimen: lateral force F_y.

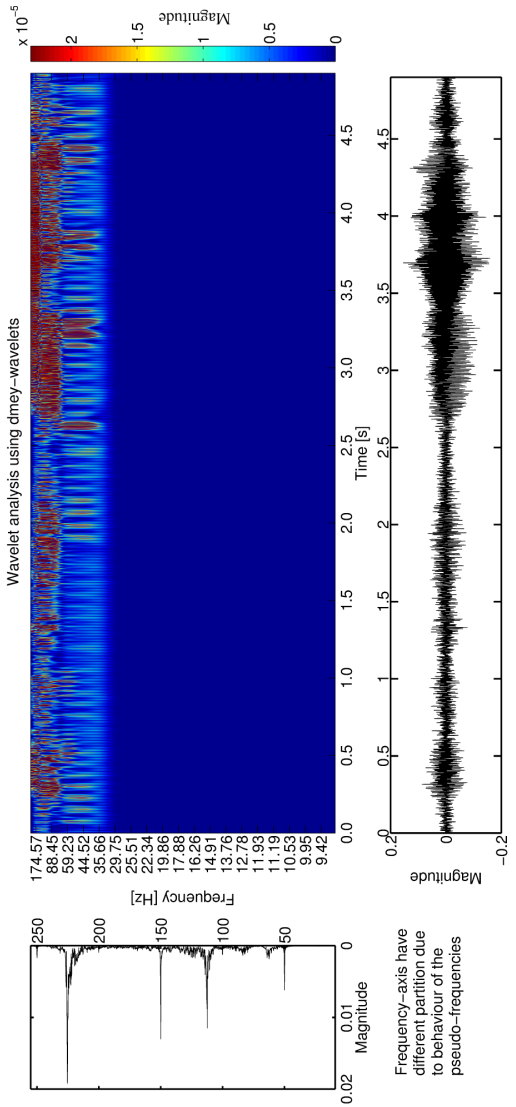

Figure 5.6: Oscillation measurement (bottom), wavelet- (center) and Fourier-analysis at velocity $v = 900$ mm/s and lift-off distance $\delta z = 1$ mm without specimen: lift force F_z.

In Figs. 5.7 – 5.9 the edges of the specimen are dominant and cause impacts. Especially low frequencies around 10 Hz and a frequency band between 58 Hz and 170 Hz are stimulated in all channels. Since impacts tend to stimulate all natural frequencies, the conclusion is that especially natural frequencies are responsible for strong oscillations. A remarkable fact is that the observed oscillations are time-variant and occur during the motion of the linear drive but not necessarily during the time the specimen is in the vicinity of the permanent magnet.

5.2 Analysis of Oscillation Phenomena

The analysis of oscillation phenomena is usually a very complex problem. The high number of oscillation inducing events and the imperfect knowledge of the observed system make it almost impossible to figure out what exactly reduces the signal quality. Measurements as performed in Sec. 5.1 help to draw conclusions in order to improve the setup from the constructive point of view. Therefore, the disturbing sources and natural frequencies of the measurement setup will be briefly analyzed. Due to the interests of brevity the moving load problem will be discussed without any analytical solution.

Analysis of noise sources

It is well known that any machine is a source of oscillation by itself [100, 101]. The particular sources of vibrations can be determined by a functional system analysis. Due to the relative low number of components of the measurement setup the main oscillators in the system can be found easily.

Vibrations occur everywhere where parts are moving. A strong noise source is the linear drive. As shown in Fig. 4.2 the rotary motor is

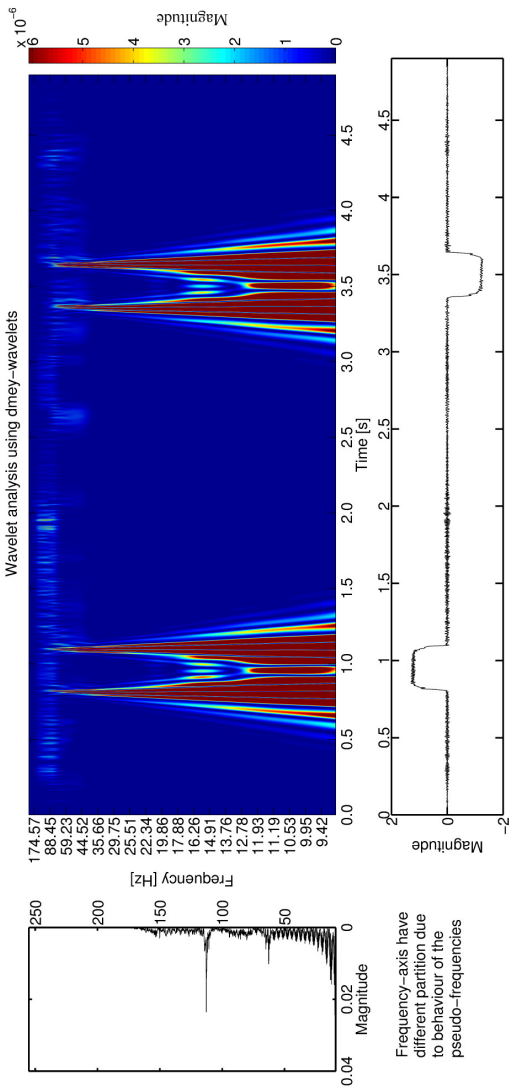

Figure 5.7: Oscillation measurement (bottom), wavelet- (center) and Fourier-analysis at velocity $v = 900$ mm/s and lift-off distance $\delta z = 1$ mm with Al-specimen: drag force F_x.

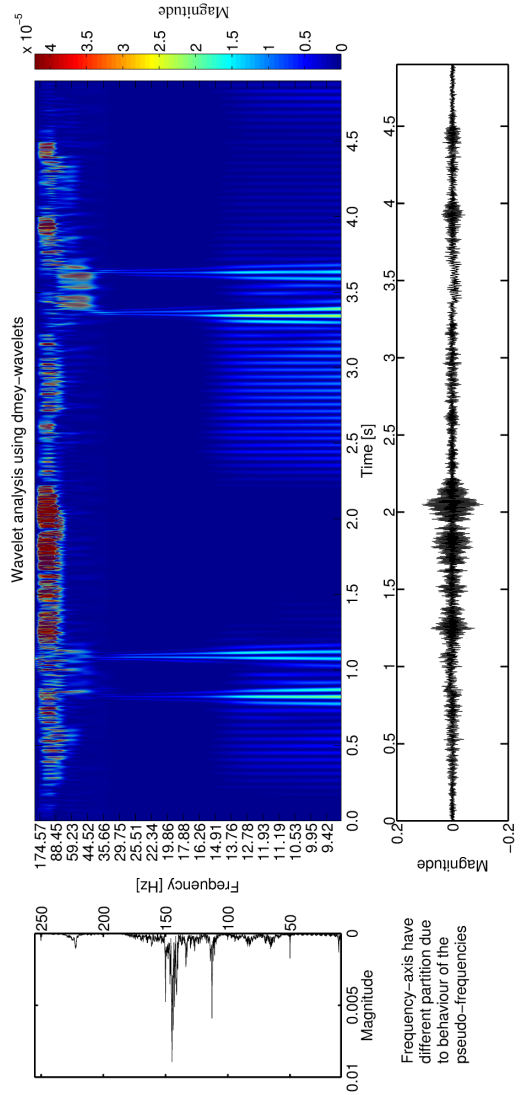

Figure 5.8: Oscillation measurement (bottom), wavelet- (center) and Fourier-analysis at velocity $v = 900$ mm/s and lift-off distance $\delta z = 1$ mm with Al-specimen: lateral force F_y.

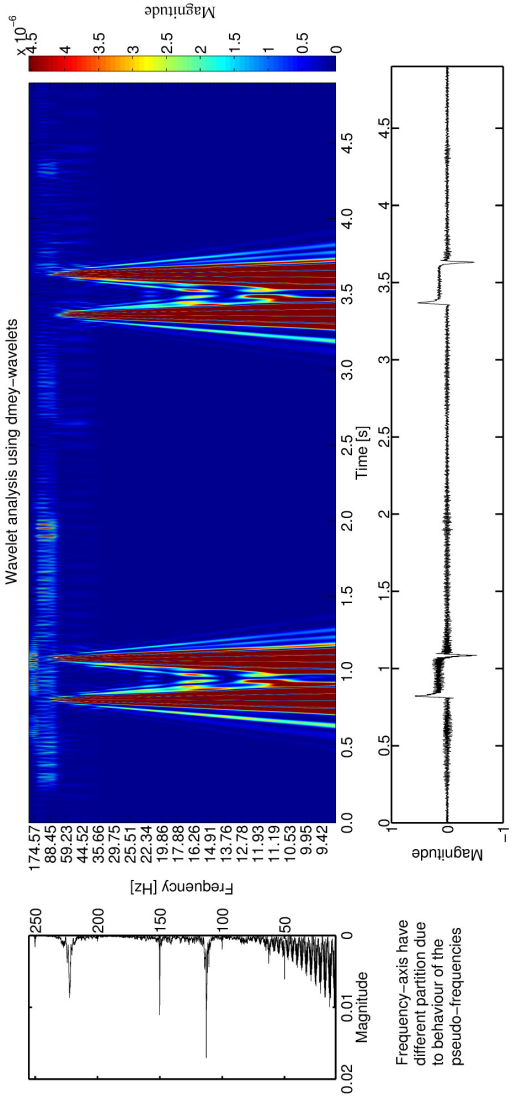

Figure 5.9: Oscillation measurement (bottom), wavelet- (center) and Fourier-analysis at velocity $v = 900$ mm/s and lift-off distance $\delta z = 1$ mm with Al-specimen: lift force F_z.

Table 5.1: Excitation frequencies connected to the linear drive at certain velocities.

v_x [mm/s]	500	900	1500	4000	$v = 2\,\pi\,r\,n_2$
f_{tooth} [Hz]	62.4	112.56	187.44	499.92	$f_{tooth} = n_2\,z_{pinion}$
n_2 [Hz]	2.60	4.69	7.81	20.83	n_2
n_1 [Hz]	7.80	14.07	23.43	62.49	$n_1 = i\,n_2$
f_{pp} [Hz]	23.4	42.21	70.29	187.47	$f_{pp} = 3\,n_1$

driving the gear which is itself driving the tooth belt. The tooth belt is fixed to the sledge which is moved along a guidance and carrying the specimen. The rotary drive is introducing an oscillation due to its unbalance in the order of the number of turns $n_1 = 0 \ldots 62.5$ Hz depending on the addressed velocity of the sledge. Furthermore, the asynchronous motor can produce a halt frequency f_{pp}.

The gear reduction of the planetary drive induces an additional frequency on its output in the range of $n_2 = 0 \ldots 20.8$ Hz. Due to the transmission of the motional energy on a pinion, the motion of the tooth belt is causing the so-called tooth engagement frequency f_{tooth}. The excitation frequencies at certain velocities can be found in Table 5.1.

Despite the mentioned excitation frequencies excitations from the environment have to be considered, i. e. building oscillations, vibrations from surrounding laboratories.

The tooth engagement frequency is providing a wide band of excitation frequencies depending on the applied velocity. This is the reason why it has to be checked whether components of the measurement setup have natural frequencies within the order of excitation. In this case they would be amplified which usually results in a decrease of the signal-to-noise ratio. The tooth engagement frequency can be found in Figs. 5.4 – 5.6 as the dominating mechanical excitation on all three channels of the force sensor.

Other disturbing sources are excited natural frequencies of the mechanical parts which have to be calculated or read from data sheets. Furthermore, the power frequency is superpositioning the measurement signal. Especially the power frequency is easy to determine. In Germany the power net frequency is 50 Hz. So, one can find a clear 50 Hz-line and lines for the higher order harmonics in all wavelet figures.

Another known excitation is the moving load that excites oscillations due to the transient change of the load's position on the mounting. This phenomenon is usually observed when trains cross rail bridges and has led to extensive analytical and numerical investigations [102]. The knowledge of that fact, ensures that attention is paid to the impacts that can be seen clearly on all force channels at same times (red spots at 2.6 s, 3.2 s and 3.8 s) in Figs. 5.4 – 5.6 & 5.7 – 5.7. Since the effect is missing during the zero measurements, the conclusion is that the support of the C-profile is not areal. Whenever the sledge passes a part of the C-profile that is not connected to the granite table it is pushed down by the moving mass inducing an impact to the foundation.

Impacts excite all natural frequencies of the system [100]. An overview of noise sources and the applied models is given in Tab. 5.2.

Natural frequencies

Besides the used multicomponent force sensor ($f_0 = 180 \ldots 60$ Hz, cf. [92]) the C-profile is most likely a main source of oscillations since the optical bench is heavy (around 350 kg) compared with the profile (around 80 kg). In order to underline the assumption, the well-known model of oscillating continuous media will be used [103, 104]. The C-profile is fixed to the optical bench at two sides by screws (cf. Fig. 5.11c). The assembly is not rigid and the C-profile is not supported areally. Therefore, the beam can oscillate longitudinally and transversely.

Table 5.2: Overview of noise sources influencing the measurement signal of the particular setup and the applied model

	noise source	**applied oscillation model**
1.	rotary drive	unbalance
2.	planetary gear	unbalance
3.	tooth belt	tooth engagement frequency
4.	linear guidance	not considered
5.	C-profile	longitudinally and transversally oscillating beam
6.	optical bench	not considered
7.	measurement frame	not considered
8.	force sensor	fixed frequency band
9.	building	not considered
10.	operator	not considered
11.	environment	not considered
12.	power frequency	fixed frequency

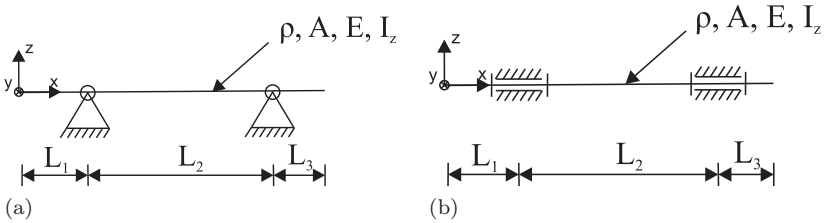

Figure 5.10: Oscillating bar with different mountings:
(a) Double mounted on solid mountings,
(b) Double mounted in fixtures.

The differential equation of motion for a longitudinally oscillating beam is

$$\frac{\partial^2 u_1(x,t)}{\partial t^2} = \frac{E}{\rho}\,\frac{\partial^2 u_1(x,t)}{\partial x^2}, \tag{5.1}$$

where $u_1(x,t)$ is the longitudinal deflection of the beam (x-direction), ρ the density and E Young's modulus of the material of the beam [104]. Equation (5.1) is of second order, whereas the description of flexural (bending) oscillations of a beam is of fourth order. It is given by [104] as

$$\frac{\partial^2 u_3(x,t)}{\partial t^2} + \frac{E\,I_z}{\rho\,A}\,\frac{\partial^4 u_3(x,t)}{\partial x^4} = 0, \tag{5.2}$$

where $u_3(x,t)$ is the transversal deflection of the beam (z-direction), I_z the area moment of inertia and A the cross-sectional area of the beam. The general solutions of Eqs. (5.1) & (5.2) are well-known and consist of trigonometric and hyperbolic functions. The particular solutions for a given problem have to be calculated applying the corresponding boundary and transition conditions.

The particularly solved problem is illustrated in Fig. 5.10. The C-profile has to be divided into three parts that are denoted by the indices $1, 2, 3$. The term $u_{31}(x,t)$ is the deflection of the first part (L_1) of the

beam in z-direction. The boundary and transition conditions for the longitudinal oscillating beam are for both mounting options

$$u'_{11}(x = 0, t) = 0 \tag{5.3}$$
$$u_{11}(x = L_1, t) = u_{12}(x = L_1, t) = 0 \tag{5.4}$$
$$u_{12}(x = L_1 + L_2, t) = u_{13}(x = L_1 + L_2, t) = 0 \tag{5.5}$$
$$u'_{13}(x = L_1 + L_2 + L_3, t) = 0 \tag{5.6}$$

whereas the flexural oscillating beam requires a more customized view on the mounting. The solid mountings (cf. Fig. 5.10a) are modeled by

$$u''_{31}(x = 0) = 0 \tag{5.7}$$
$$u'''_{31}(x = 0, t) = 0 \tag{5.8}$$
$$u_{31}(x = L_1, t) = u_{32}(x = L_1, t) = 0 \tag{5.9}$$
$$u_{32}(x = L_1 + L_2, t) = u_{33}(x = L_1 + L_2, t) = 0 \tag{5.10}$$
$$u'_{31}(x = L_1, t) = u'_{32}(x = L_1) \tag{5.11}$$
$$u''_{31}(x = L_1, t) = u''_{32}(x = L_1, t) \tag{5.12}$$
$$u'_{32}(x = L_1 + L_2, t) = u'_{33}(x = L_1 + L_2, t) \tag{5.13}$$
$$u''_{32}(x = L_1 + L_2, t) = u''_{33}(x = L_1 + L_2, t) \tag{5.14}$$
$$u''_{33}(x = L_1 + L_2 + L_3, t) = 0 \tag{5.15}$$
$$u'''_{33}(x = L_1 + L_2 + L_3, t) = 0 \tag{5.16}$$

and the fixtures (cf. Fig. 5.10b) by

$$u''_{31}(x = 0, t) = 0 \tag{5.17}$$
$$u'''_{31}(x = 0, t) = 0 \tag{5.18}$$
$$u_{31}(x = L_1, t) = u_{32}(x = L_1, t) = 0 \tag{5.19}$$
$$u_{32}(x = L_1 + L_2, t) = u_{33}(x = L_1 + L_2, t) = 0 \tag{5.20}$$
$$u'_{31}(x = L_1, t) = u'_{32}(x = L_1, t) = 0 \tag{5.21}$$
$$u'_{32}(x = L_1 + L_2, t) = u'_{33}(x = L_1 + L_2, t) = 0 \tag{5.22}$$

Table 5.3: Geometrical and material properties used for the analytical model of an oscillating beam.

Dimension	**Value**
L_1	0.895 m
L_2	2.058 m
L_3	1.070 m
A	$2.57 \cdot 10^{-3}$ m^2
E	$2.1 \cdot 10^5$ MPa
ρ	7850 kg/m^3
I_z	$1.08 \cdot 10^{-6}$ m^4

$$u''_{33}(x = L_1 + L_2 + L_3, t) = 0 \tag{5.23}$$
$$u'''_{33}(x = L_1 + L_2 + L_3, t) = 0 \tag{5.24}$$

The geometrical and material properties of the C-profile at hand are summarized in Tab. 5.3. The resulting linear systems of equations have been solved with a mathematical software, e. g. in this case with *Maple*.

The natural frequencies of the real C-profile are lying in between those of the two investigated mounting situations because the real assembly should be between a solid mounting and a fixture. The obtained results can be found in Tabs. 5.4 and 5.5. In order to verify the results for a flexural oscillating beam, a structural mechanics model has been solved numerically for the C-profile that is mounted on elastic bearings and on fixtures. The results differ slightly. The most interesting part for the modal analysis is that both models provide a natural frequency band between 60 . . . 90 Hz which can be observed in the measurements as well. So, a precise distinction whether the oscillations in this band are caused by the force sensor or another source cannot be made.

Table 5.4: Natural frequencies of a longitudinal oscillating beam calculated with the analytical model.

mode	**analytical solid**
1^{st}	36.34 Hz
2^{nd}	39.30 Hz
3^{rd}	51.94 Hz
4^{th}	157.18 Hz
5^{th}	327.08 Hz
6^{th}	353.66 Hz

Table 5.5: Natural frequencies of a flexural oscillating beam calculated with different models.

mode	**analytical fix.**	**numerical fix.**	**analytical solid**	**numerical elastic**
1^{st}	51.79 Hz	44.53 Hz	22.47 Hz	15.89 Hz
2^{nd}	74.02 Hz	62.77 Hz	39.87 Hz	21.47 Hz
3^{rd}	89.08 Hz	79.29 Hz	78.25 Hz	37.25 Hz
4^{th}	245.55 Hz	88.23 Hz	188.12 Hz	59.74 Hz
5^{th}	324.55 Hz	110.41 Hz	275.69 Hz	71.56 Hz
6^{th}	463.87 Hz	126.09 Hz	364.46 Hz	92.82 Hz

5.3 Filter Synthesis

As found in Sec. 5.2 there are different disturbing sources influencing the Lorentz force eddy current testing setup. In order to suppress unwanted signals the application of digital filters is preferable. The advantage of a software realization of filters is the rather simple adaption to digital circuits, such as FPGAs.

Most of the classical filter approaches (low pass, high pass, bandpass, bandstop filters,...) are useful for the determination of static values. Phase shifts and amplifications of the signal require a good knowledge of the applied filters and the process times in order to reduce errors induced by the applied filters. The filtering of high dynamic signals is more difficult because the conservation of fast signal changes has to be ensured and parts of the signal which are caused by disturbing sources and noise have to be suppressed.

In Table 5.6 the found disturbing sources are summarized and the applied filters are named [70]. The applied filters ensure a wide working range with high dynamics. The classical filters are used for the suppression of known disturbing sources that are almost time-invariant. Due to the good adjustment a small phase shift ($<$ 10 data points) is realized and the amplification of the filtered signal yields within 10 data points.

The white noise, i. e. the statistically distributed variation of the measured signal, is filtered using a wavelet filter. The huge advantages of wavelet filters are the high dynamics and the simplicity of choice of the right settings [97, 99]. Attention has to be paid to the fact that the filter is able to generate a signal that has been expected. It is recommended to test the filter on artificial signals and example measurement signals. Another advantage of wavelet filters is the possible realization on FPGAs [105].

Table 5.6: Identified disturbing sources and applied filters.

Effect	**Filter**	**Frq. [Hz]**	**Sampling frq. [Hz]**
Foundation frequency	Notch filter	10.9	44
Power frequency	Notch filter	50	200
Mechanical mounting	Band-stop filter	60 ... 90	300
White noise	Dmey-wavelet filter	$\approx 50 \ldots 230$	continuous

5.4 Constructive Improvements

Besides the implementation of appropriate filter techniques a significant improvement of the signal-to-noise ratio can be achieved by constructive improvements. As shown in Sec. 5.2 many excitation frequencies and natural frequencies are situated close together. Especially the frequency band 60 ... 90 Hz is problematic due to the fact that the natural frequencies of the force sensor and the C-profile, which is part of the foundation of the drive system, are in this range.

A conclusion can be drawn from the natural frequency of an undamped free single degree of freedom oscillator which can be calculated according to [104]

$$f_0 = \frac{1}{2\,\pi}\sqrt{\frac{c}{m}}. \tag{5.25}$$

Increasing the stiffness and decreasing the mass of the system lead to an increase of the natural frequency. It has been shown that it is possible to increase the signal-to-noise ratio of the measured force signal by a factor of ten [89].

Table 5.7: Natural frequencies of an oscillating beam calculated with analytical model after constructive changes.

mode	**longitudinal osc.**	**transversal osc., fix.**	**transversal osc., solid**
1^{nd}	39.30 Hz	35.45 Hz	89.08 Hz
2^{rd}	153.29 Hz	99.61 Hz	218.43 Hz
3^{th}	157.18 Hz	147.75 Hz	218.43 Hz
4^{th}	353.66 Hz	237.02 Hz	245.55 Hz
5^{th}	$>$ 628 Hz	$>$ 424 Hz	$>$ 479 Hz

Due to the fact that the C-profile caused impacts and oscillations within the measurement range it has been shortened (mass reduction) and assembled symmetrically with tenterhooks (increase of stiffness of the system). These measures result in a drastic increase of the natural frequencies. Table 5.7 illustrates the analytical solution applying the changed geometry to the model. The lengths according to Table 5.3 have been changed to $L_1 = L_3 = 0.521$ m.

In order to reduce the impacts on the system induced by the movement of the linear drive sledge, a damping mat has been placed between the C-profile and the granite block. It ensures an areal contact between both elements. Furthermore, the measurement frame has been isolated from the foundation using damping mats as well (cf. Figs 5.11). Additionally, a poly-v-belt has been assembled instead of the tooth belt in order to reduce the number of oscillation sources.

The overall resulting decrease in noise can be seen while comparing Figs. 5.1 – 5.6 with Figs. 5.12 – 5.14 & 5.15 – 5.17. In Figs. 5.12 – 5.14 & 5.15 – 5.17 the reduction in magnitude of the excited frequencies is observed. The dominant disturbing frequency remains the power frequency of 50 Hz and its harmonics. The oscillations in the frequency band $60 \ldots 90$ Hz are not visible anymore. The impacts have vanished and there are no motion induced oscillations anymore (cf. Fig. 5.15 –

(a)

(b)

(c)

(d)

Figure 5.11: Lorentz force eddy current testing, measurement setup before and after the constructive changes:
(a) overview before changes,
(b) overview after changes,
(c) mounting of the C-profile before changes,
(d) mounting of the C-profile after changes.

5.17). There are remaining artifacts from the movement of the drive which can be caused by the acceleration forces.

After the constructive changes, the filters have to be modified according to the signals to suppress. Therefore, only the notch filter for the power frequency and the wavelet-filter for the white noise filtering remain.

5.5 Force Signal Verification

The constructive improvement of the measurement setup for Lorentz force eddy current testing has had immense influence on the signal quality. The signal-to-noise ratio has been improved by the factor of ten. The changes on the setup require a verification of the measured force signal to be sure that both signals, before and after the constructive changes, can be used to determine the characteristics of Lorentz force eddy current testing.

Therefore, the raw signals and the corresponding filtered signals are compared with each other in Fig. 5.18. The forces are in very good agreement. The difference in both force components, drag and lift force, is around 5% which is in the range of the repeatability of the measured forces.

Figure 5.18a shows convincingly that many oscillation effects are removed. The rather simple changes on the measurement setup have had big influence on the measured signal. Especially resonance-like effects as can be found before the changes at around 1.7 s for the drag force are gone. Remarkable for the filter synthesis is that the filtered signal remains the same qualitatively even though the signal-to-noise ratio increased by a factor of ten. The slight declination of the filtered drag force is due to a misalignment of the specimen towards the force sensor. All fluctuations are conserved in both force components. In the following chapters results from before and after the constructive changes are

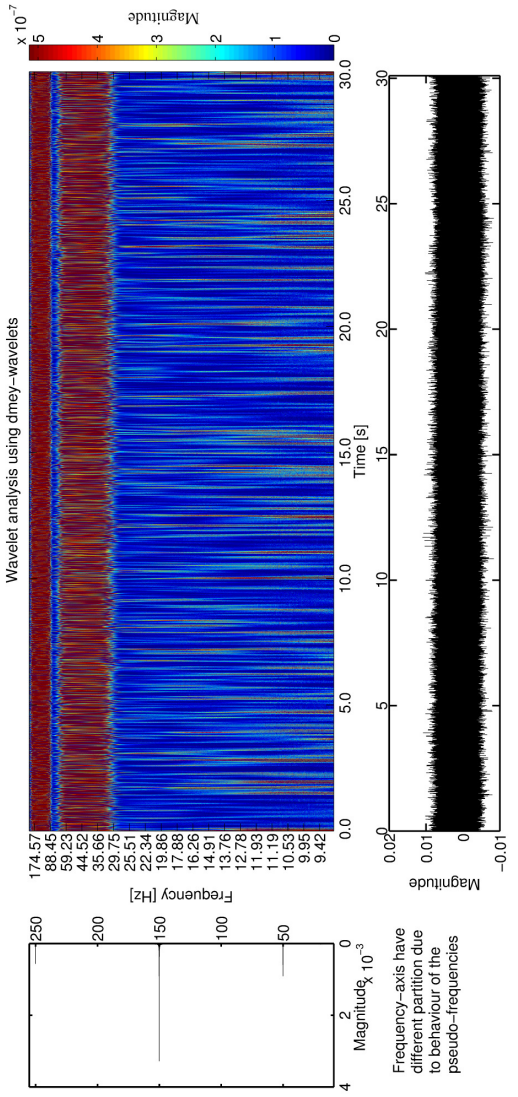

Figure 5.12: Oscillation measurement (bottom), wavelet- (center) and Fourier-analysis without motion: drag force F_x.

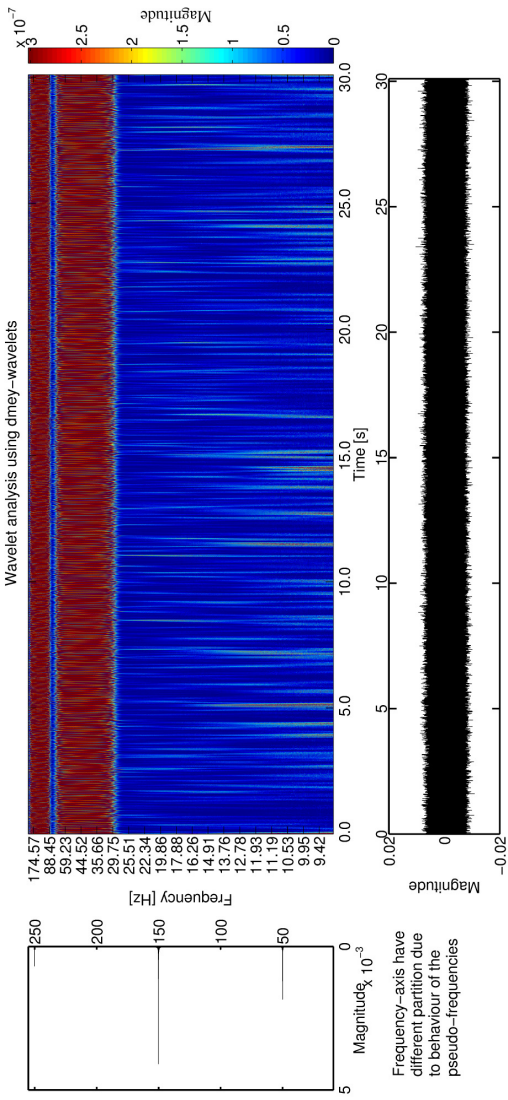

Figure 5.13: Oscillation measurement (bottom), wavelet- (center) and Fourier-analysis without motion: lateral force F_y.

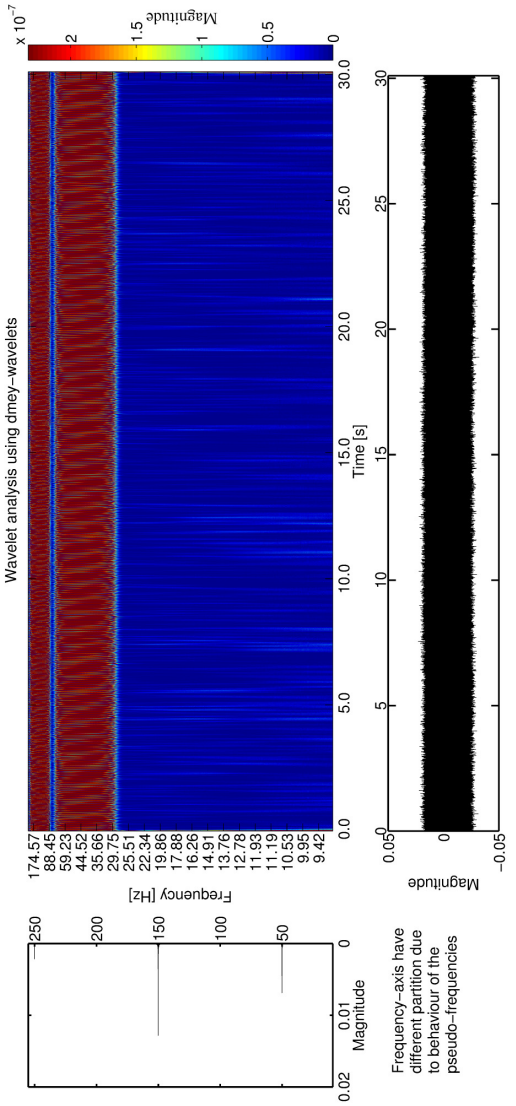

Figure 5.14: Oscillation measurement (bottom), wavelet- (center) and Fourier-analysis without motion: lift force F_z.

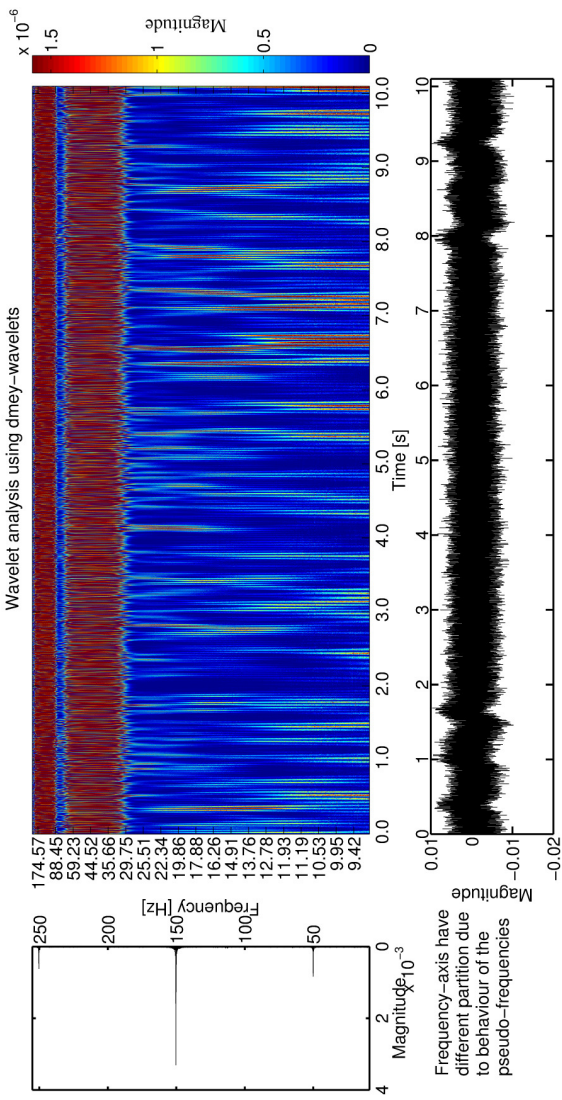

Figure 5.15: Oscillation measurement (bottom), wavelet- (center) and Fourier-analysis at velocity $v = 900$ mm/s and lift-off distance $\delta z = 1$ mm without specimen: drag force F_x.

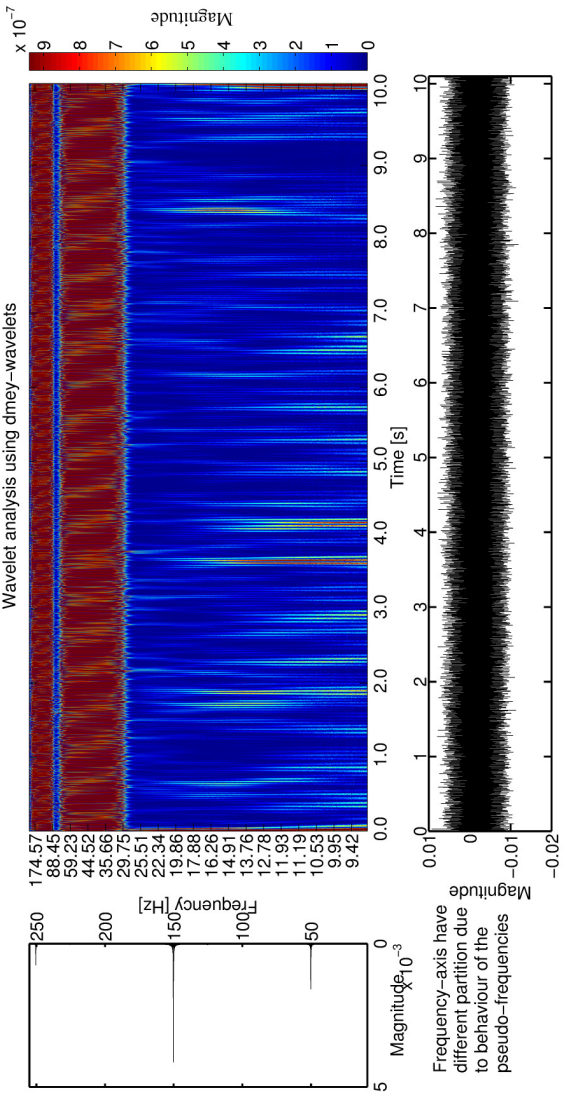

Figure 5.16: Oscillation measurement (bottom), wavelet- (center) and Fourier-analysis at velocity $v = 900$ mm/s and lift-off distance $\delta z = 1$ mm without specimen: lateral force F_y.

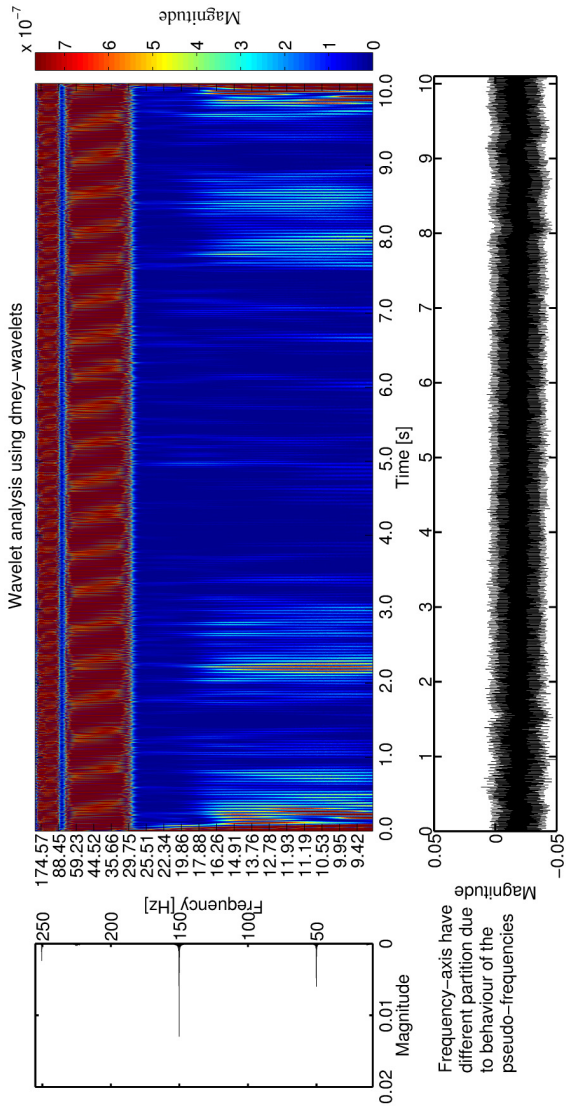

Figure 5.17: Oscillation measurement (bottom), wavelet- (center) and Fourier-analysis at velocity $v = 900$ mm/s and lift-off distance $\delta z = 1$ mm without specimen: lift force F_z.

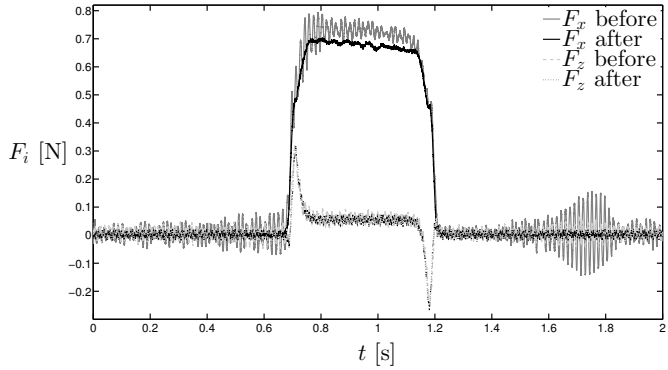

(a)

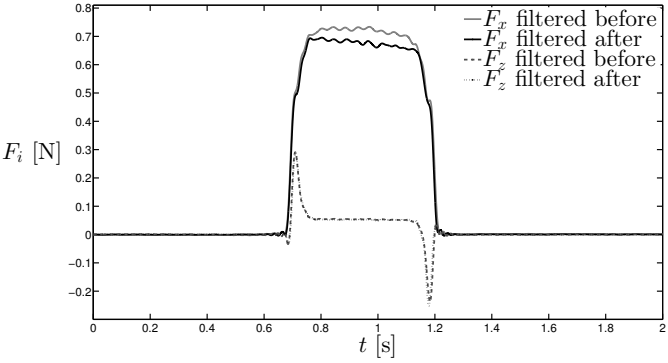

(b)

Figure 5.18: Measured force signals before & after constructive changes on the setup at $v = 500$ mm/s and lift-off distance $\delta z = 1$ mm, Al-bar without defects:
(a) raw signals,
(b) filtered signals.

equivalent. There is no longer a need to emphasize whether the force has been measured on the improved or the original setup.

6 Application of Lorentz Force Eddy Current Testing

The measurements of [8] have shown that Lorentz force eddy current testing works. Therefore, a long rod with several kinds of defects in different orientations has been examined. The rod has not been mounted areally and the defects have been introduced close to each other. The problem of a long, bended rod and overlapping defect areas made it impossible to determine sizes or locations of defects precisely. In addition, the defects have been chosen to be relatively large. Here, another approach has been chosen: the bar is relatively short whereas the magnet system has been simplified in comparison with the experiments done before.

6.1 Verification of Measured Forces Using a Specimen Without Defects

In this section, the physical behavior of the bar specimen is investigated. The main aim is to determine the system's reaction on changing parameters, e. g. velocity, lift-off distance and magnet size. The influencing parameters are summarized in Fig. 6.1. Since the behavior has been studied already extensively the results are used to verify the measured data [62, 106, 107]. Additionally, the knowledge of the basic response of a system without defects enables a more convincing comparison with a system containing artificial defects.

Two specimens of different material (aluminum and copper) have been considered (cf. Fig. 6.2). Due to the fact that the electrical conductivity of the specimens is of eminent importance for eddy current applica-

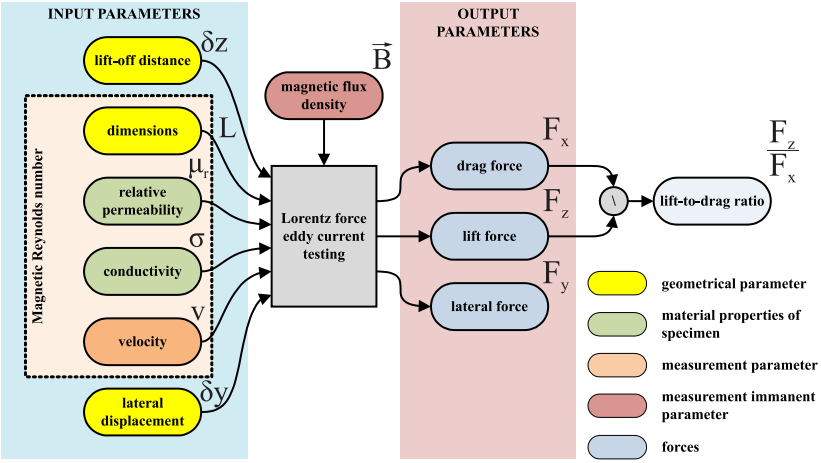

Figure 6.1: Overview on input and output parameters of Lorentz force eddy current testing.

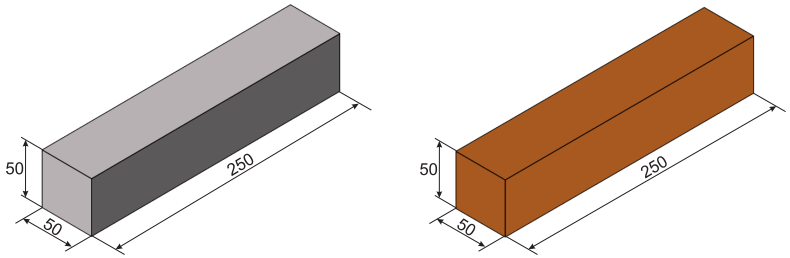

(a) (b)

Figure 6.2: Specimens without defect (dimensions $50 \times 50 \times 250$ mm^3)
(a) aluminum alloy
(b) copper alloy.

tions, the conductivities of both specimens have been measured with the commercial eddy current device *Sigmatest 2.069* (Institut Dr. Foerster GmbH & Co. KG [108]) to $\sigma_{\mathrm{Al}} = 20.4$ MS/m and $\sigma_{\mathrm{Cu}} = 57.9$ MS/m, respectively. This enables the increase of the magnetic Reynolds number R_m (see Eq. (3.76)) in order to investigate the start of the nonlinear range.

6.1.1 Lorentz Force Profile

The most natural signal is force as a function of time that will be referred to as the Lorentz force profile. As shown in Fig. 6.3 there are three channels captured simultaneously. The profile consists of five parts: (i) the measurement starts ($t = 0 \ldots 0.2$ s), (ii) the specimen enters the vicinity of the permanent magnet ($t = 0.2 \ldots 0.36$ s), (iii) the specimen is in the vicinity of the permanent magnet ($t = 0.36 \ldots 0.68$ s), (iv) the specimen leaves the vicinity of the magnet ($t = 0.68 \ldots 0.84$ s) and (v) the measurement ends ($t = 0.84 \ldots 1.1$ s). Due to the use of the real-time data acquisition system the data points are equidistantly taken according to the sampling rate of 10 kHz. As expected the lateral force component is approximately zero because the measurement has been performed at the symmetry axis ($\delta y = 0$ mm). The difference to the zero line can be understood as a measure for the alignment quality.

To investigate the general behavior of the specimen without defect, especially concerning dependencies on velocity and displacements of the magnet, the measured Lorentz force has been averaged according to

$$F_i = \frac{1}{b-a} \cdot \sum_{n=a}^{b} F_i(t_n), \tag{6.1}$$

where a and b represent the start and the end point of the averaging interval. The region that is used to determine the acting Lorentz force is sufficiently far away from the edges of the specimen. So, the force is assumed to be constant. The remaining assembly error (e. g. tilt in

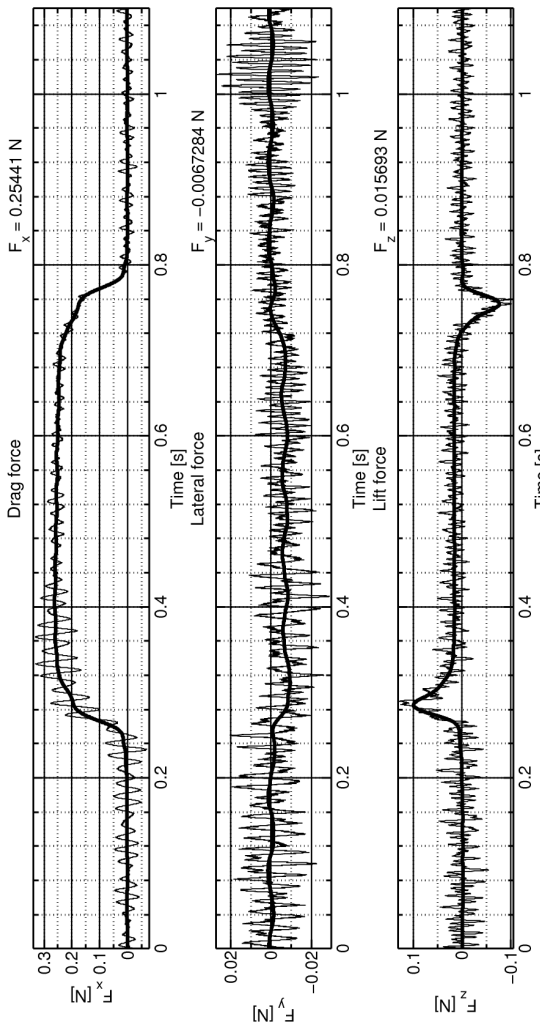

Figure 6.3: Lorentz force profile, $v = 500$ mm/s, $\delta z = 3$ mm and $\delta y = 0$ mm, cylindrical permanent magnet ø15 × 25 mm, N38. Grey line corresponds to the raw data and solid black line to the filtered data.

x-z-plane) is compensated due to the averaging process. The obtained average force is given on the right top of the graphs in Fig. 6.3. Since the measurement principle has a limited number of influencing parameters (cf. Fig. 4.2), the physical dependencies can be investigated by changing only one parameter at a time while all others are fixed.

6.1.2 Velocity Dependency

The investigations of Reitz [62] show that the drag component of the Lorentz force is depending linearly whereas the lift component depends quadratically on the relative velocity. This statement is true for relatively low magnetic Reynolds numbers R_m ($R_m \ll 1$). Reitz shows that the drag force is saturating at a certain velocity and starts to decline when the velocity is further increased. The dominating effect is the motional skin effect which leads to an expel of the magnetic field of the specimen. In contrast the lift force is rising for a bigger range of velocities.

Thess et al. used the assumption of a small magnetic Reynolds number in order to provide analytical and semi-analytical models for the Lorentz force velocimetry [69, 74]. In Fig. 6.4 is shown that this assumption is only true for velocities up to about 1 m/s depending strongly on the electrical conductivity of the specimen. Thus, velocities below 1 m/s can be understood as the low magnetic Reynolds number range. The numerical data used in Fig. 6.4 have been calculated using the model of [72] and have been validated in [109].

6.1.3 Lift-Off Distance Dependency

Due to the fact that the magnetic field drops down very fast with increasing distance between source and specimen, it is necessary to figure out the dependency between the Lorentz force and the lift-off

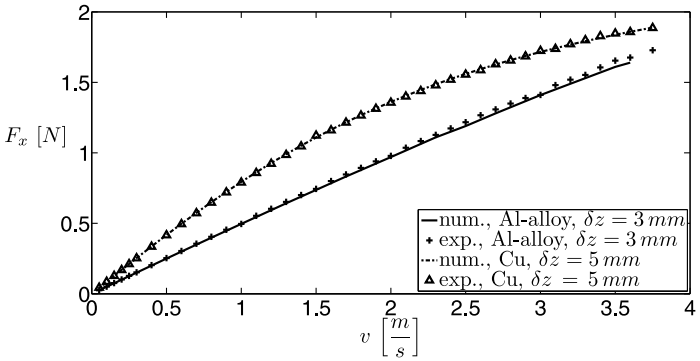

(a)

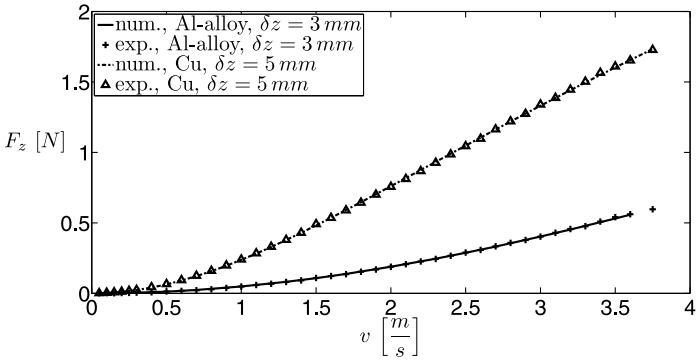

(b)

Figure 6.4: Force dependency on velocity, different materials, fixed lift-off distance δz, cylindrical permanent magnet ø15 × 25 mm, N 38:
(a) Drag force F_x vs. velocity v
(b) Lift force F_z vs. velocity v.

distance. The lift-off distance δz is the shortest distance between the surface of the specimen and the surface of the permanent magnet.

As shown in Fig. 6.5, the Lorentz force is decaying rapidly with increasing lift-off distance. The behavior leads to a change in sensitivity S with respect to the applied lift-off distance. The sensitivity can be calculated according to

$$S = \frac{dF}{d(\delta z)}. \tag{6.2}$$

This means that changes in lift-off distance are detected very accurately when the magnet is positioned close to the surface of the specimen. At a lift-off distance of $\delta z = 1$ mm the sensitivity is around $S = 30$ N/mm. Consequently, there is the possibility of using Lorentz force eddy current testing for the contactless evaluation of surface roughness. A permanent magnet that provides a high spatial resolution and a force sensor that can detect small deviations in force would have to be applied.

The main conclusion that is drawn from this behavior is that for every application another working point is optimal. Having in mind that defect detection is the main application of Lorentz force eddy current testing, the suggestion is to stick to an medium lift-off distance to avoid strong oscillations due to the surface quality of the specimen [70, 109]. In this case "medium" lift-off distance cannot be evaluated quantitatively because it is described by the optimal working point in terms of Lorentz force and sensitivity S. The Lorentz force has to be high enough to be measurable, whereas sensitivity S has to be reduced sufficiently.

6.1.4 The Lift-to-Drag Ratio

The relationship between the velocity and the resulting Lorentz force has been described. The dependency is valid for plates as well and

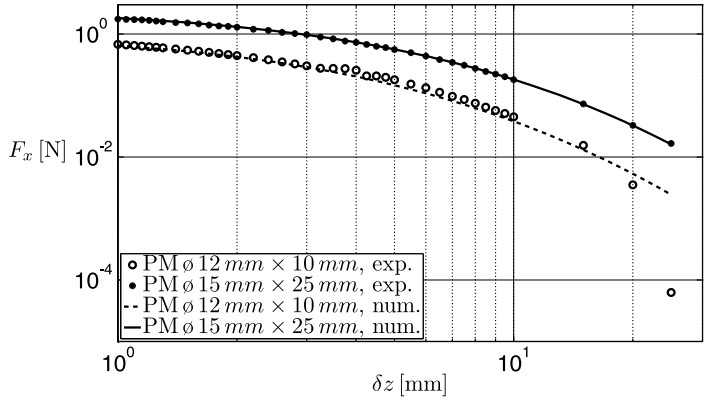

(a)

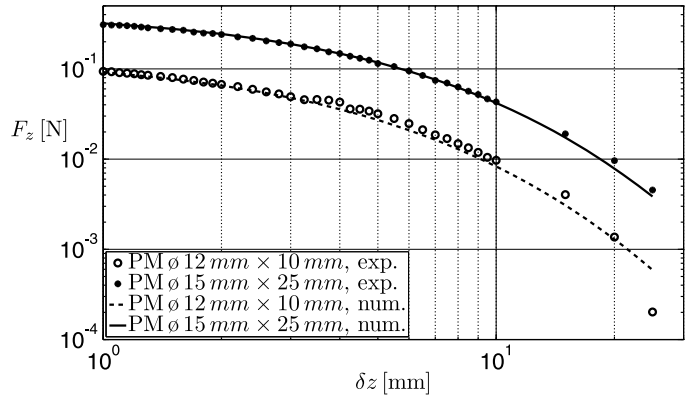

(b)

Figure 6.5: Force dependency on lift-off distance and different magnet size (fixed velocity $v = 2$ m/s, Al-bar):
(a) Drag force F_x vs. lift-off distance δz
(b) Lift force F_z vs. lift-off distance δz.

can be formulated with the help of the magnetic Reynolds number (see Eq. (3.76)) as

$$F_x \sim R_m, \tag{6.3}$$

$$F_z \sim R_m^2. \tag{6.4}$$

Consequently, the measured Lorentz force depends on the geometry of the magnet system, on the velocity and, in particular, on the lift-off distance and the magnetic flux density $\vec{B}$ [109]. Manufacturing errors and mechanical oscillations can lead easily to deviations of up to 100 µm in lift-off distance resulting in force deviations of some millinewtons depending on the lift-off distance. The magnetic field strength of the permanent magnet is usually not given and it is difficult to determine since magnetization direction and mounting errors have to be taken into account.

To overcome the disadvantages of using only the drag component a modified approach is applied. As a consequence of Eqs. (6.3) & (6.4) the ratio of F_z/F_x depends only linearly on R_m:

$$\frac{F_z}{F_x} \sim R_m. \tag{6.5}$$

For thin plates of infinite extension, it was found that for any shape of the magnetic field source the lift-to-drag ratio can be written as

$$\frac{F_z}{F_x} = \frac{v}{w}, \tag{6.6}$$

where w is the characteristic velocity of the conductor under test determined by

$$w = \frac{2}{\mu_0 \, \sigma \, D}, \tag{6.7}$$

where D is the thickness of the specimen [61].

However, Eq. (6.6) can be used for plates and sheets as long as their thickness does not exceed the motional skin depth (cf. Eq. (3.78)) and velocity is kept in the low/intermediate R_m-range which is the case for moderate velocities ($v \leq 5$ m/s) [62].

Considering half of the bar thickness to be the characteristic length scale of the present problem Eq. (6.6) can be rewritten as

$$\frac{F_z}{F_x} = R_m. \tag{6.8}$$

Obviously, the lift-to-drag ratio depends on the geometry of the test system including the specimen's dimensions, (weakly) the lift-off distance, the specimen's material properties and the translational velocity.

Nevertheless, the lift-to-drag ratio is almost linear for both materials for low and intermediate velocities (see Fig. 6.6). The experiments with copper alloy show that the linear dependency on velocity is still valid on the bounds of the existing conductivity range.

Another important issue is the dependency of the Lorentz force on the lift-off distance (see Fig. 6.5). In order to increase the total force, a smaller lift-off distance δz is preferable. The disadvantage of a decreasing lift-off distance is the increase of the sensitivity to surface dependent lift-off distance changes, e. g. surface roughness. The evaluation of the lift-to-drag ratio reduces the sensitivity to the lift-off distance drastically as can be seen from Fig. 6.7. The measured forces for high lift-off distances ($\delta z \geq 10$ mm) are far beyond the measurement uncertainty of the applied force sensor. Due to that fact, the lift-to-drag ratio is out of line with respect to the simulated values.

6.1.5 Dependency on Lateral Displacement

The change in lateral displacement causes a significant change in the eddy current distribution whereas the changes in velocity and lift-off

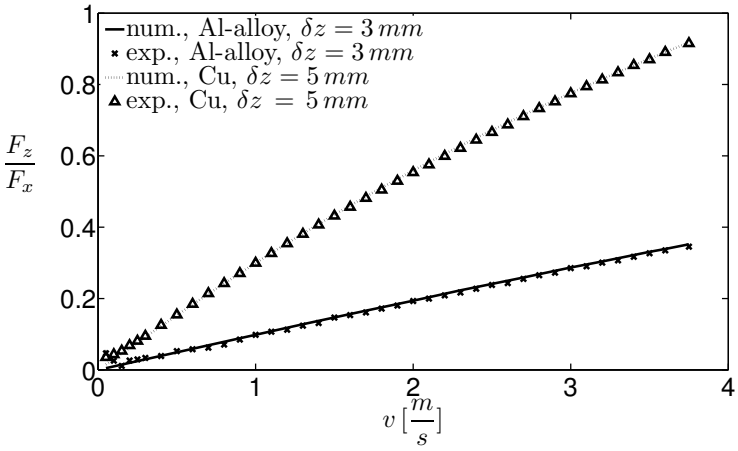

Figure 6.6: Dependency of the ratio between lift force and drag force on velocity for Al-alloy and Cu (lift-off distance $\delta z = 3$ mm and 5 mm, respectively).

have only an influence on the magnitude of the Lorentz force. Eddy currents that are not distributed symmetrically result in a repulsive force component on the magnet that is directed lateral to the direction of motion and towards the closer edge of the specimen. The drag and lift forces become smaller compared to that acting at the symmetry line whereas the lateral force is zero at the symmetry line and when the lateral sensor position is far enough away from the specimen (cf. Fig. 6.8 – 6.10).

Due to the symmetry of the eddy current distribution the following relations can be defined:

$$F_x(\delta y) = F_x(-\delta y) \tag{6.9}$$

$$-F_y(\delta y) = F_y(-\delta y) \tag{6.10}$$

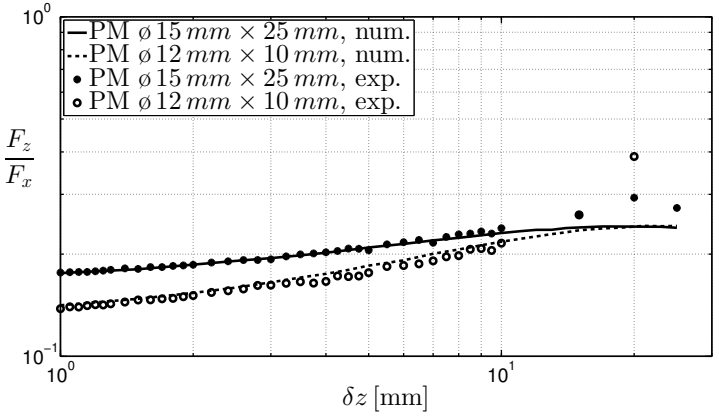

Figure 6.7: Dependency of the lift-to-drag ratio on lift-off distance for the Al-bar for different permanent magnet sizes, where $v = 2000$ mm/s and $\delta y = 0$ mm.

$$F_z(\delta y) = F_z(-\delta y) \tag{6.11}$$

Consequently the lateral force can be used to align the sensor with respect to the specimen and to determine the alignment errors. The stated relations are only valid for a specimen without defect. The force perturbations caused by defects can serve to detect the defect position relatively to the permanent magnet (left, right, central) due to the fact that the orientation of the perturbations follows the same basic principle. Thus, it becomes evident that having all three force components increases the number of information gathered during just one measurement run.

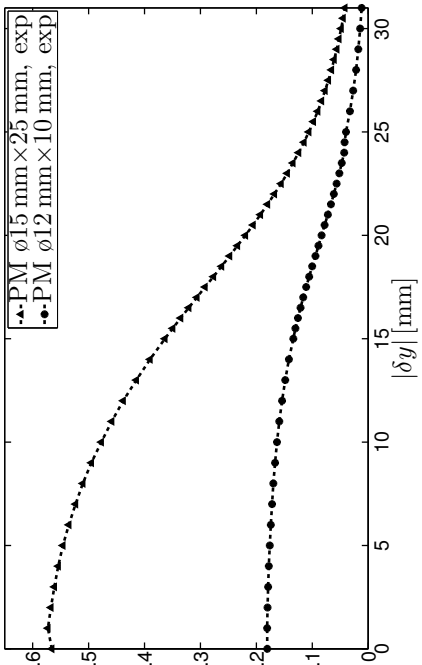

Figure 6.8: Force dependency on lateral displacement and different permanent magnet size (fixed velocity $v = 2$ m/s, lift-off distance $\delta z = 5$ mm, Al-bar): drag force F_x vs. lateral displacement δy.

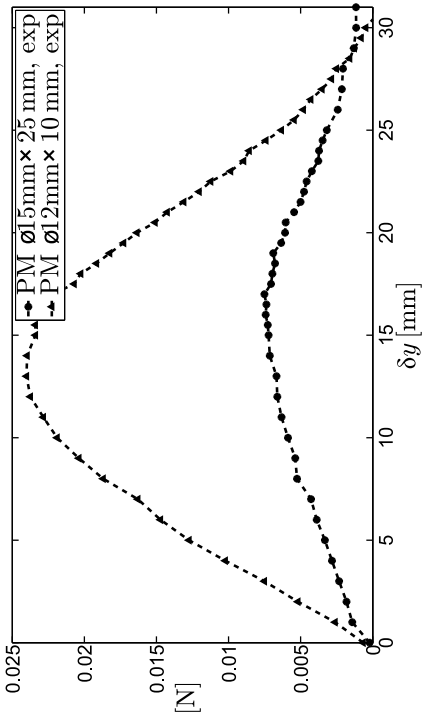

Figure 6.9: Force dependency on lateral displacement and different permanent magnet size (fixed velocity $v = 2$ m/s, lift-off distance $\delta z = 5$ mm, Al-bar): lateral force F_y vs. lateral displacement δy.

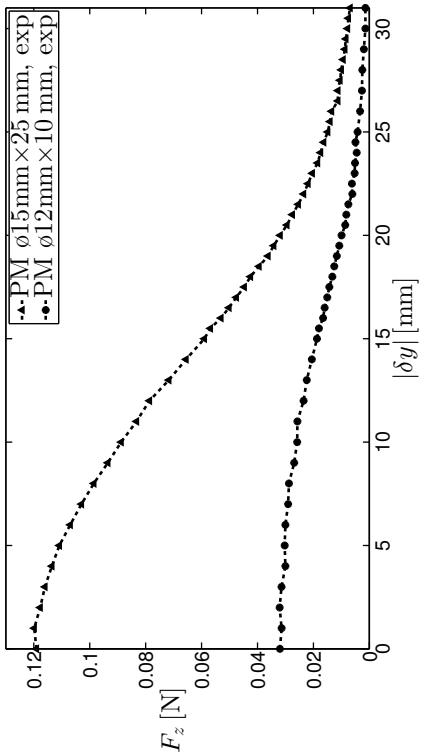

Figure 6.10: Force dependency on lateral displacement and different permanent magnet size (fixed velocity $v = 2$ m/s, lift-off distance $\delta z = 5$ mm, Al-bar): lift force F_z vs. lateral displacement δy.

6.2 Laminated Specimen

The detection of defects is the main application of Lorentz force eddy current testing. In order to enable the variation of depth of artificial defects the solid state body has been approximated by an aluminum sheet package. Even though the sheets are pressed together it is obvious that there cannot be an ideal (electrical) contact. Surface finishing and oxidation increase the resistance on the boundary layers. Furthermore, the electrical conductivity of the single metal sheets is different compared with the Al-bar. The electrical conductivity of every used sheet has been measured with the eddy current device *Sigmatest 2.069* (Institut Dr. Foerster GmbH & Co. KG) as $\sigma_{\mathrm{MS}} = 31.48$ MS/m which is an increase of around 50%. This results in a 50% higher drag force.

The characteristic Lorentz force profile is conserved whereas perturbations are stronger. Reason for the higher sensitivity is the anisotropic conductivity of the metallic sheet package. Due to the higher resistance of the boundary layers there is no z-component of the eddy currents acting [72]. In Fig. 6.11 a series of measurement results is shown. The Lorentz force is plotted as a function of the bar coordinates where $(x, y) = (0, 0)$ is the centroid of the bar surface area. All specimens have been inspected with a velocity of $v = 500$ mm/s and a lift-off distance of $\delta z = 1$ mm.

Strong oscillations can be seen in Fig. 6.11a but weak oscillations in Fig. 6.11c. Since the drag force distribution in Fig. 6.11a is not symmetric to the line $y = 0$, alignment errors between the permanent magnet and the specimen have to be considered. Besides the oscillations and edges of the conductor, there is no clear perturbation visible on the graphs. Figure 6.11d shows the lift-to-drag ratio. The strong attenuation of the oscillations allows the conclusion that they are caused by lift-off distance changes. This conclusion is strengthened by the fact that the correlation of the force signals from different measurements is very high (cf. Fig. 5.18).

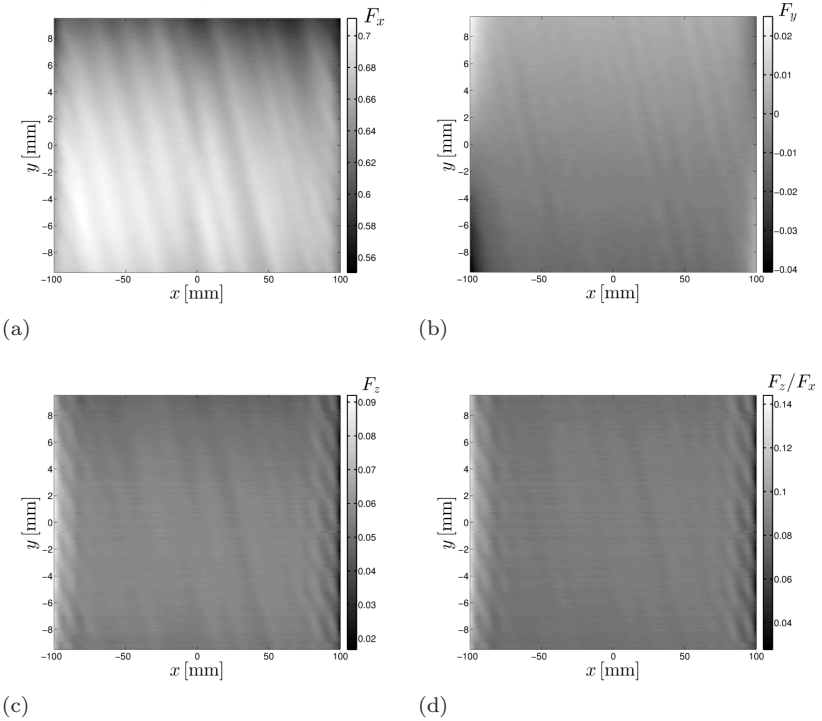

Figure 6.11: Lorentz force components depending on the position of the specimen relatively to the magnet (N38, ø15 × 25 mm^3) at a lift-off distance of $\delta z = 1$ mm and velocity $v = 500$ mm/s:
(a) metallic sheets w/o defects, drag force F_x,
(b) metallic sheets w/o defects, lateral force F_y,
(c) metallic sheets w/o defects, lift force F_z,
(d) metallic sheets w/o defects, lift-to-drag ratio F_z/F_x.

6.3 Detection of Deep-Lying Artificial Defects

Even though the technique of Lorentz force eddy current testing has been classified as a surface method (cf. Ch. 2) it has been hypothesized that applying DC magnetic fields should enable the determination of deep lying defects within electrical conductors (cf. Ch. 3).

The verification of the assumption has been performed considering different artificial defects. There are three defect types devoted to the metal sheet package which can be varied in depth (see Figs. 6.12b, 6.12c & 6.12d) and two validation bars (see Figs. 6.12e & 6.12f) in order to provide benchmark problems that can be compared with numerical simulations [9, 72].

6.3.1 Stacked Metal Sheets

The investigation on the maximum detectable depth of an artificial defect within the metal sheet package has been performed by scanning the bar with the permanent magnet. Therefore, the metal sheet package has been assembled and the alignment procedure executed according to Sec. 4.4. The specimen has been moved forth and back changing the lateral position of the permanent magnet after each measurement run. During each measurement all three components of the Lorentz force have been recorded.

After the measurement procedure, the obtained Lorentz force profiles have been synchronized on the basis of the specimen's edges and plotted as a contour plot in the x-y-plane where the measured force values correspond to a gray scale. Besides the three "raw" components the lift-to-drag ratio has been plotted as well, in order to damp surface condition induced interferences.

Due to the interests of brevity the presentation of surface breaking defects is omitted. The long defect which is placed on the second layer

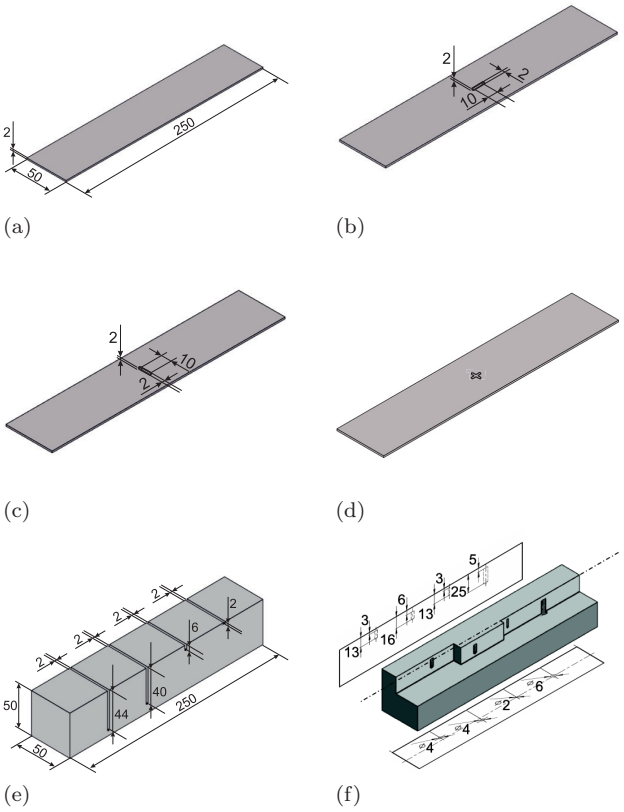

Figure 6.12: Specimen with artificial defects:
(a) aluminum alloy sheet without defect
(b) aluminum alloy sheet with defect: long (10×2 mm^2)
(c) aluminum alloy sheet with defect: wide (2×10 mm^2)
(d) aluminum alloy sheet with defect: cross (long + wide)
(e) aluminum alloy bar with four slit defects
(f) aluminum alloy bar with four hidden defects (cut view).

(2 mm under the surface) can be seen very well in Fig. 6.13. All three components of the Lorentz force comprise a significant perturbation in the centroid of the bar's surface. The drag force F_x (see Fig. 6.13a) is dropping at $x = 0$ mm. The defect induced perturbation can be easily found in the lift force F_z (see Fig. 6.13c) as well. The information of lift and drag force can be merged in the lift-to-drag ratio (see Sec. 6.1.4). As shown in Fig. 6.13d the interferences are damped and therewith the sensitivity to the perturbation is increased.

The prediction that on the symmetry line there is no response from the lateral force component F_y is confirmed with Fig. 6.13b. The force component is strongly perturbed in the vicinity of the defect but in the symmetry line. The force is unperturbed in $(x, y) = (0, 0)$. This fact is of high interest for the localization and the reconstruction of the defect because the position of the defect relatively to the magnet can be determined from the lateral force component.

Moving the defect deeper into the metal sheet package results in a weaker perturbation of the forces. Nevertheless, the long defect is detectable by the used measurement system without troubles to a depth of up to 6 mm (see Fig. 6.14).

The corresponding wide defect can only be detected to a depth of 4 mm under the surface because the perturbation is weaker than the one of the long defect (see Fig. 6.15), whereas the cross defect causes a stronger perturbation due to the bigger defect volume.

Placing the long defect deeper inside the metal sheet package than 6 mm under the surface causes the perturbation to be in the order of the remaining oscillations. That is the reason why the defect cannot be detected with a sufficiently high probability of detection anymore.

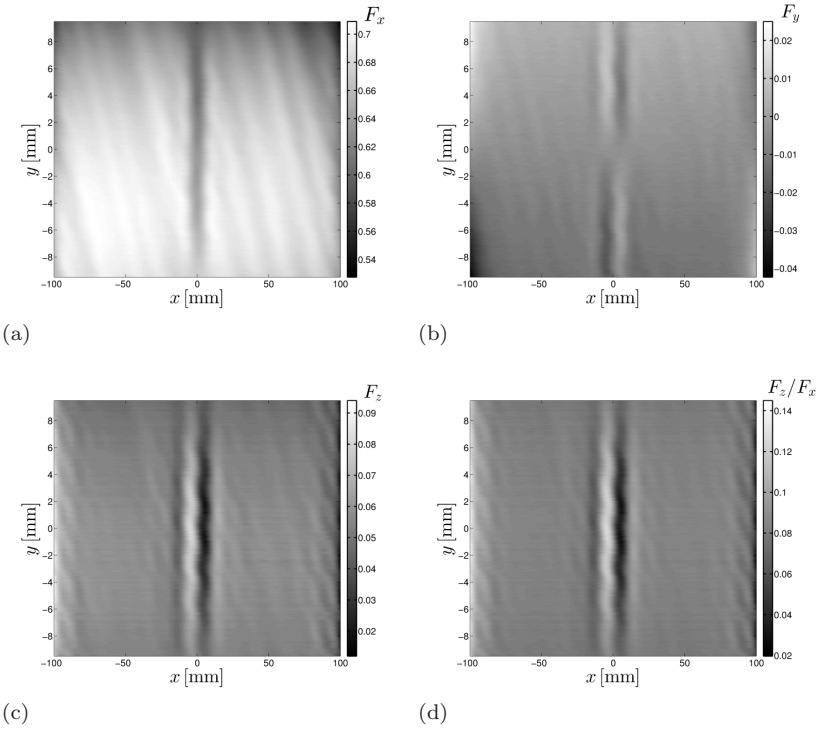

Figure 6.13: Lorentz force components depending on the position of the specimen relatively to the magnet (N38, ø15 × 25 mm^3) at a lift-off distance of $\delta z = 1$ mm and velocity $v = 500$ mm/s, defect depth 2 mm:
(a) Defect long, drag force F_x,
(b) Defect long, lateral force F_y,
(c) Defect long, lift force F_z,
(d) Defect long, lift-to-drag ratio F_z/F_x.

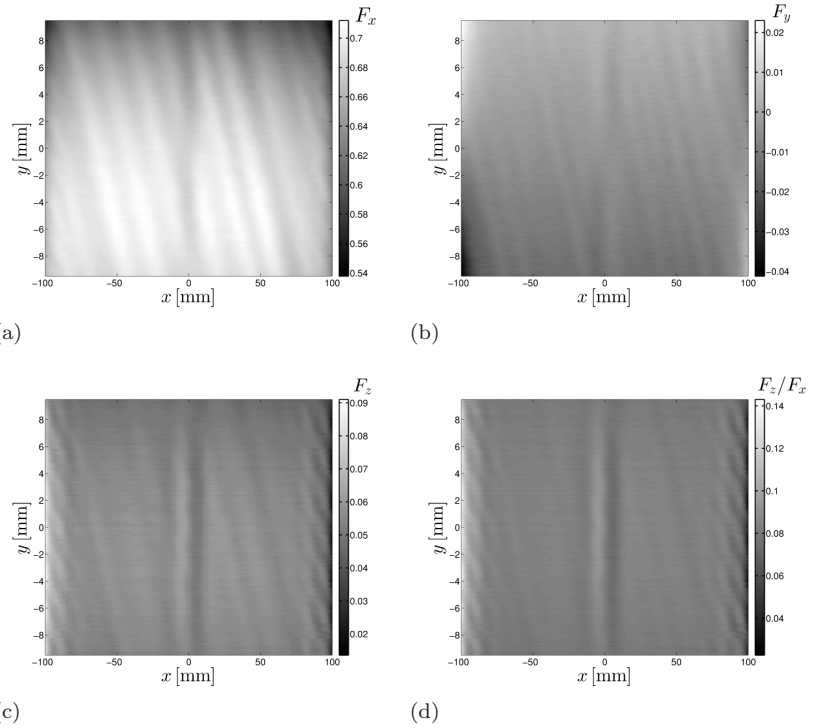

Figure 6.14: Lorentz force components depending on the position of the specimen relatively to the magnet (N38, ø15 × 25 mm^3) at a lift-off distance of $\delta z = 1$ mm and velocity $v = 500$ mm/s, defect depth 6 mm:
(a) Defect long, drag force F_x,
(b) Defect long, lateral force F_y,
(c) Defect long, lift force F_z,
(d) Defect long, lift-to-drag ratio F_z/F_x.

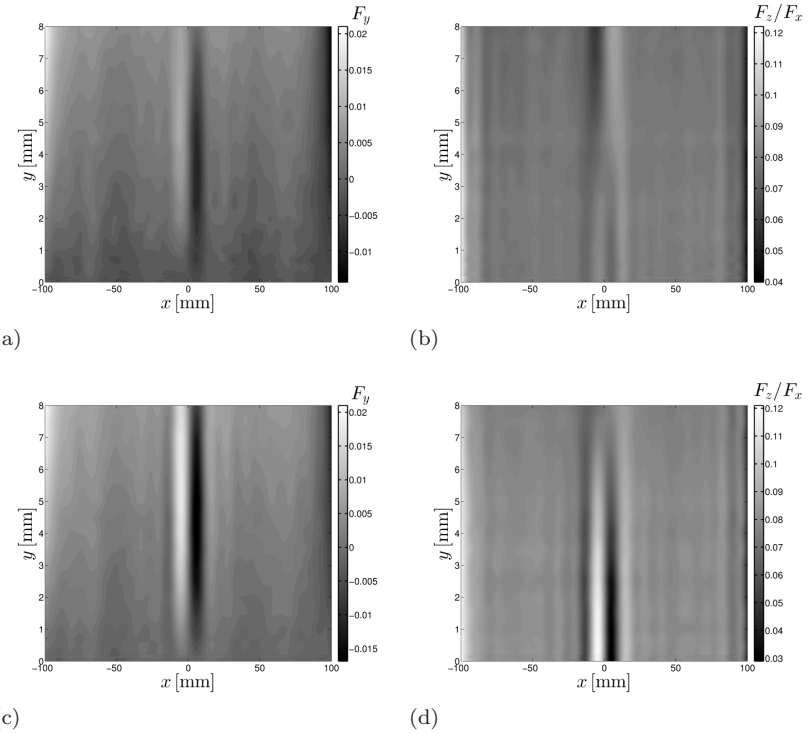

Figure 6.15: Lorentz force components depending on the position of the specimen relatively to the magnet (N38, ø15 × 25 mm^3) at a lift-off distance of $\delta z = 1$ mm and velocity $v = 500$ mm/s, defect depth 2 mm:
(a) Defect wide, lateral force F_y,
(b) Defect wide, lift-to-drag ratio F_z/F_x,
(c) Defect cross, lateral force F_y,
(d) Defect cross, lift-to-drag ratio F_z/F_x.

6.3.2 Solid Specimen

Metal sheet packages cause higher perturbations than solid bodies due to their anisotropic conductivity. That is the reason why two benchmark problems with solid bars have been considered. The validation bar for numerical simulations contains four bore holes of different diameter and depth [9]. The bore holes have been filled with the same material as the bar itself. For that, cylinders have been pressed into the hole (cf. Fig. 6.12f). As can be seen from Fig. 6.16a, all four defects can be detected. Since the sizes of the defects are very different, the smallest defect at $(x, y) = (25\ \text{mm}, 0)$ is difficult to detect visually but there is a clear perturbation when zooming into the area of interest.

Again, with the help of the lateral force component and the lift-to-drag ratio the defects can be localized without doubt. It would be sufficient to provide these two figures. The strong perturbations of the defects which are deep inside the specimen can be explained in the following way: The boundary of the bore hole fillings is covered with a very thin oxide layer and thus, the path of the eddy currents is perturbed which can be understood as a surface breaking defect.

The second validation bar contains four slits. Since the slits go through the whole width of the specimen it is closer to a 2D-problem, from the numerical point of view. The measurements from top and bottom of the specimen can be found in Fig. 6.17.

From the top view (see Figs. 6.17a & 6.17b) one can clearly identify all four slits. The intensity of the perturbation is a measure of their depths, the stronger the perturbation the deeper the defect. This fact is again interesting for the reconstruction and the estimation of the influence of the detected defect on the specimen functionality.

The bottom view (cf. Figs. 6.17c & 6.17d) reveals that the slits which are in this case 44 mm and 48 mm deep cannot be detected. Nevertheless, the slit 10 mm under the surface now can be determined without a well trained eye. Obviously, a slit is a quite big defect and the path of the eddy current is mostly parallel to the transversal slit.

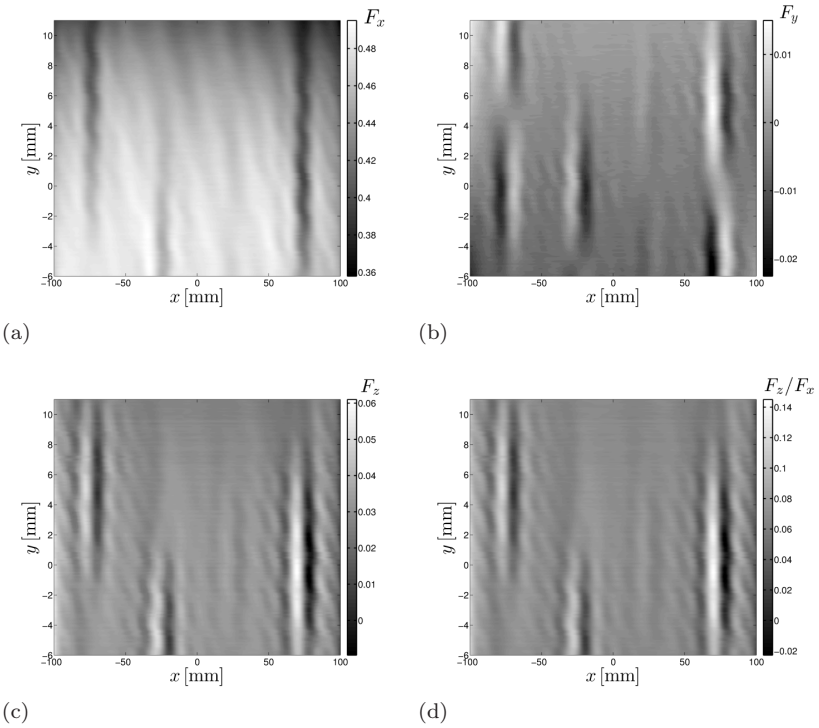

Figure 6.16: Lorentz force components depending on the position of the specimen relatively to the magnet (N38, ø15 × 25 mm^3) at a lift-off distance of $\delta z = 1$ mm and velocity $v = 500$ mm/s:
(a) Hidden defects, drag force F_x,
(b) Hidden defects, lateral force F_y,
(c) Hidden defects, lift force F_z,
(d) Hidden defects, lift-to-drag ratio F_z/F_x.

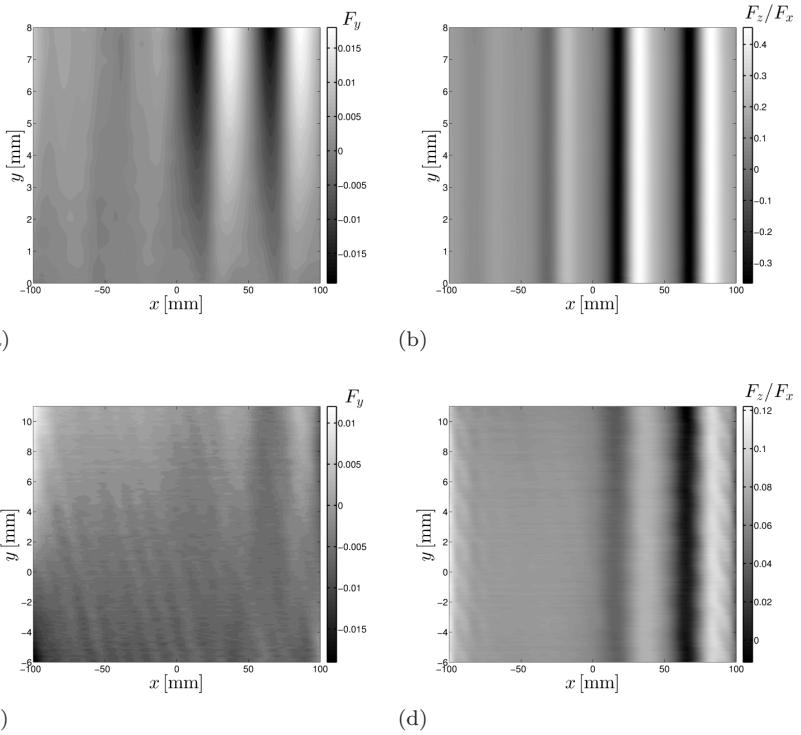

Figure 6.17: Lorentz force components depending on the position of the specimen relatively to the magnet (N38, ø15 × 25 mm^3) at a lift-off distance of $\delta z = 1$ mm and velocity $v = 500$ mm/s:
(a) Slit defects from top, lateral force F_y,
(b) Slit defects from top, lift-to-drag ratio F_z/F_x,
(c) Slit defects from bottom, lateral force F_y,
(d) Slit defects from bottom, lift-to-drag ratio F_z/F_x.

6.4 Limits of the Lorentz Force Eddy Current Testing Measurement Setup

It has been shown in the previous Sec. 6.3 that there are several influences limiting the defect detection in depth even though the calculated motional skin depth allows to draw the conclusion that one could see through the whole bar. Some of the found aspects are summarized in this section.

6.4.1 Signal Quality

The detection of defects with the help of Lorentz force eddy current testing is based on the detection of perturbations in the Lorentz force. Due to the fact that the magnetic field and consequently the eddy currents are attenuating strongly with the distance to the permanent magnet, the response of the secondary magnetic field is the weaker the further away the defect is from the surface. Consequently, the challenge is to detect small force perturbations which are caused by deep lying and very small defects.

The determination of a significant change in the measured signal is described by the signal-to-noise ratio (SNR). In the literature is shown that a SNR = 6 dB (≈ 1.82) is sufficient to detect a deep lying defect using classical eddy current testing [32]. Classical eddy current testing profits strongly from the recent developments in high dynamic and low noise electronics whereas Lorentz force eddy current testing suffers from the poor availability of low noise force sensors which would provide a high resolution.

Despite of the application of an appropriate force sensor, the signal quality can be increased from the constructive point of view. In order to reduce the interference of the environment, it is preferable to apply measures for oscillation reduction, as e. g. isolation and damping.

Furthermore, the SNR can be increased by designing system components with higher natural frequencies than the force sensor has. This, of course, is not always possible.

6.4.2 Force Measurement

The force transducer is of significant importance for the Lorentz force eddy current testing. The applied sensor type influences the dynamics of the force sensor and thus, the capability of defect detection. The described sensor dynamics are characterized by the first natural frequency of 180 ... 60 Hz depending on load. Assuming the model of a single-degree-of-freedom oscillator one can state that responses of signal changes with frequencies higher than $\sqrt{2}$ times the natural frequency are weakened, caused by the effect of oscillation isolation [104].

The corresponding frequencies of the specimen and the investigated defects are presented in Table 6.1. The permanent magnet is assumed to be a magnetic point dipole without spacial expansion. The point spread function of the response on the magnetic field is a Dirac delta function. Fairly spoken, this assumption is far away from reality but provides the worst case scenario. Consequently, the corresponding frequency f_{corr} can be calculated by

$$f_{corr} = \frac{v}{L} \tag{6.12}$$

where L determines the dominant dimension (length) in moving direction. In reality, the point spread function is a complex shaped function which changes with velocity and lift-off distance [51]. It provides a distribution into space due to the fact that the magnetic field of the permanent magnet is neither concentrated in one line nor one point. So, the frequencies are expected to be smaller and though, lower system dynamics than given are necessary. Nevertheless, it is clear that a detection of small defects and/or at high velocities can only be successful when the first natural frequency of the force sensor is sufficiently high.

Table 6.1: Corresponding frequencies according to Eq. (6.12) for the bar specimen and different kinds of defects on the basis of available samples on the object of interest at different velocities.

v	**corresponding frequency**		
	bar	**defect long**	**defect wide**
50 mm/s	0.2 Hz	5 Hz	25 Hz
500 mm/s	2 Hz	50 Hz	250 Hz
1000 mm/s	4 Hz	100 Hz	500 Hz
1500 mm/s	6 Hz	150 Hz	750 Hz
2000 mm/s	8 Hz	200 Hz	1000 Hz
3000 mm/s	12 Hz	300 Hz	1500 Hz
3750 mm/s	15 Hz	375 Hz	1875 Hz

Obviously, the demand on a force sensor with a high natural frequency and a very high resolution states a conflict of objectives. A force can only be detected by its effect on a test body. This effect can be a deformation or an acceleration. The applied indirect force measurement on the basis of strain gauge technology is cost effective. An appropriate deformation body is used to measure the deflection with strain gauges which occurs when a force acts on it. The stiffness of this deformation body has to be reduced in the so-called flexure hinges in order to achieve a measurable deflection in a certain direction.

The stiffness of these flexure hinges is mainly responsible for the first natural frequency of the force sensor. So, for high dynamic measurements, a high stiffness is required. This results in a high first natural frequency but in low strain as well. Consequently, the deformation measurement system is limiting the smallest detectable perturbation in terms of time (small defect) and velocity (low process time) for the applied force measurement principle. Whereas the bar itself can be identified even for high velocities, the detection of the long defect per-

turbation is limited by a velocity of approximately 1.5 m/s and a wide defect already by less than 0.5 m/s for the particular force sensor [92].

6.4.3 Motional Skin Depth

Despite the signal quality and the force measurement system the motional skin depth is limiting the capabilities of the Lorentz force eddy current testing. It has been described already in Sec. 3.2 that due to the motion induced skin effect the magnetic field is expelled from the conductor. At very high velocities the eddy currents are concentrated on the surface of the conductor which results in a reduction of the Lorentz force [62]. Obviously, defects in great depths can only be detected to a certain limit, i. e. while the response of the secondary magnetic field is high enough to be detected. It has been shown that using classical eddy current testing defects in depths of up to three times the skin depth can be detected [32].

Even though there are analytical descriptions of the skin depth in the form of Eq. (3.78) [62, 110], the formulas could not be verified. The motional skin depth should not depend on the dimensions of the specimen since it describes the attenuation of the eddy currents within the specimen. Nevertheless, the motional skin depth is not a limiting factor for the defect detection at the present state.

6.5 Lorentz Force Sigmometry

A further feature of the presented Lorentz force eddy current testing is the ability of nondestructive evaluation of material properties. The goal of this section is to demonstrate that the same Lorentz force that is used in Lorentz force eddy current testing can be exploited for the contactless determination of electrical conductivities.

For the numerical evaluation of absolute force values, the properties of the investigated materials are required to be known. The characteristic material property for any measurement technique using eddy currents and/or electro-magnetic fields is the electrical conductivity of the specimen or fluid under test. Nowadays, there are only a few established measurement techniques that suit the determination of the electrical conductivity. Fluids are usually treated with amperometric and potentiometric measurements (which are basically the same), whereas solid state bodies are treated with impedance spectroscopy and the four-point-method [111–113]. A big disadvantage is, depending on the application, the contact with the specimen, that might be not possible, e.g. in hot metals or if the specimen is moving fast. Contactless methods, as e. g. the eddy current method [112], suffer strongly from deviations in lift-off distance, cover only the subsurface region and cannot provide conductivity measurements deeper within the material due to the skin effect.

The conductivity measurement technique presented here helps to overcome the above-mentioned disadvantages since it provides a contactless measurement deep inside the material, no matter whether it is a fluid or a solid body. Since the internationally widely used Greek symbol for the conductivity is σ and the exploited physical effect is the Lorentz force the method is named "Lorentz force Sigmometry" (LoFoS). The results presented here can be found in [57] in a more comprehensive version.

As a consequence of Eq. (6.5) the conductivity which is assumed to be homogeneous and isotropic, can be described for a constant velocity as

$$\sigma = \alpha_{\mathrm{cal}} \frac{F_z}{F_x}, \tag{6.13}$$

where the calibration coefficient α_{cal} depends on the geometry of the magnet system, on the translational velocity, and (weakly) on the lift-off distance. Since α_{cal} is *a priori* unknown, either a numerical or experimental calibration has to be conducted.

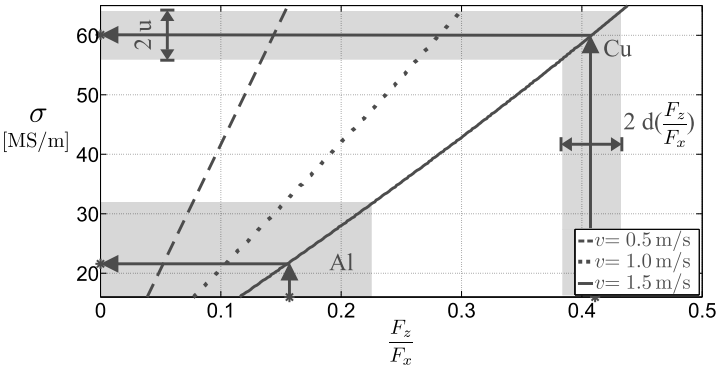

(a)

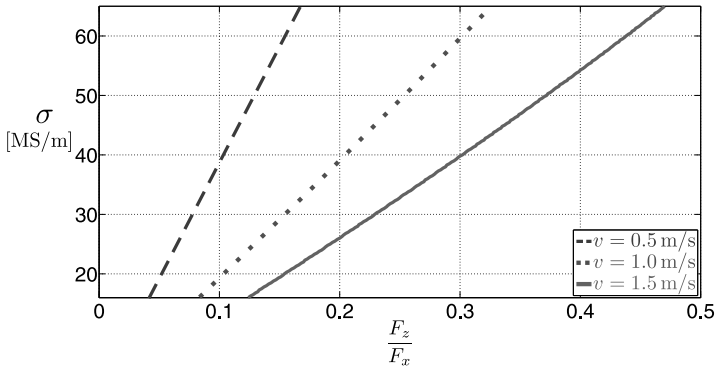

(b)

Figure 6.18: Numerically obtained calibration curves for different velocities for the solid bar specimen ($W \times H \times L = 50 \times 50 \times 250$ mm):
(a) lift-off distance $\delta z = 3$ mm (example from Table 6.3),
(b) lift-off distance $\delta z = 5$ mm.

Table 6.2: Basic linear fitting coefficients for numerical bar calibration

Coeff.	$\delta z = 3\,\mathrm{mm}$			$\delta z = 5\,\mathrm{mm}$		
v [m/s]	0.5	1.0	1.5	0.5	1.0	1.5
α_{cal} [MS/m]	417.91	216.26	151.43	389.46	201.54	140.89
σ_{off} [MS/m]	-0.26	-1.04	-2.18	-0.25	-1.01	-2.10

The numerically obtained calibration curves shown in Fig. 6.18 represent the basis for the implementation of the Lorentz force sigmometry technique. Using the assumption of a linear dependency between conductivity and lift-to-drag ratio (cf. Eq. (6.13)), basic linear fitting has been used to obtain the function in the form

$$\sigma = \alpha_{\mathrm{cal}} \frac{F_z}{F_x} + \sigma_{\mathrm{off}}, \tag{6.14}$$

where σ_{off} is the offset that results from the linear fit at the measurement range between $20 \ldots 60$ MS/m.

The specimen has to be measured with the same velocities as for the calibration. The obtained lift-to-drag ratios have to be marked in the calibration graphs. If more than one velocity is used it is possible to average the obtained conductivity values. The overall measurement error can be calculated by the total derivative of the lift-to-drag ratio

$$d\left(\frac{F_z}{F_x}\right) = \frac{F_x\, dF_z - F_z\, dF_x}{{F_x}^2}, \tag{6.15}$$

where the values denoted by a d are the measurement uncertainties of the applied force sensor ($dF_x = 15$ mN, $dF_x = 50$ mN). The overall measurement uncertainty in electrical conductivity u can be determined by evaluating the linear equation Eq. (6.14)

$$u = \alpha_{\mathrm{cal}}\, d\left(\frac{F_z}{F_x}\right). \tag{6.16}$$

Table 6.3: Conductivity calculation using LoFoS

Parameter	Unit		
Material	-	Al	Cu
v	m/s	1.5	1.5
δz	mm	3	3
F_x	N	0.735	1.92
dF_x	N	0.015	
F_z	N	0.115	0.789
dF_z	N	0.050	
$\frac{F_z}{F_x} \pm d\left(\frac{F_z}{F_x}\right)$	-	0.157 ± 0.065	0.411 ± 0.022
$\sigma \pm u$	MS/m	21.59 ± 9.82	60.08 ± 3.46

The Lorentz forces exerting on two solid bars of known conductivity, namely aluminum and copper, have been measured. For reference, their conductivities have been obtained ($\sigma_{\mathrm{Al}} = 20.4$ MS/m, $\sigma_{\mathrm{Cu}} = 57.92$ MS/m) with the help of an eddy current device *Sigmatest 2.069* (Institut Dr. Foerster GmbH & Co. KG). The measured lift-to-drag ratios have been used to determine the conductivities of these bars. For that, the purely numerically obtained calibration curves in Fig. 6.18 have been used. The measurement uncertainties and the intermediate results are given in Table 6.3. Applying the linear fitting coefficients from Table 6.2 the conductivities of $\sigma_{\mathrm{Al}} = 21.59$ MS/m and $\sigma_{\mathrm{Cu}} = 60.08$ MS/m, respectively, have been obtained. The overall measurement uncertainties of $u_{\mathrm{Al}} = 9.82$ MS/m and $u_{\mathrm{Cu}} = 3.46$ MS/m, respectively, are based on the uncertainty of the force sensor(dF_x, dF_z). They can be reduced when the measurements are repeated several times or by applying a more appropriate force sensor.

7 Summary and Outlook

The focus of the thesis at hand is the proof of principle of the new nondestructive material testing technique "Lorentz force eddy current testing". In this chapter, the main results are summarized and an outlook for further work is given.

7.1 Summary: Lorentz Force Eddy Current Testing

Classical eddy current testing suffers strongly from the frequency-dependent skin effect, which is responsible for the expel of the magnetic field from the electrically conducting specimen. Due to the fact that low frequencies and high spatial resolution lead to a conflict of objectives, compromises have to be made in terms of detection depth and localization. The application of direct magnetic fields (DC magnetic fields) has been claimed to be promising to help to improve some of the limitations of the classical eddy current testing [8]. Thus, the detection of deep lying defects within moving conductors at medium velocity is enabled.

7.1.1 The Prototype Model

The basic principle of Lorentz force eddy current testing has been elucidated using the rather simple academic problem of a permanent magnet falling in an electrically conducting pipe. It has been shown that the model of the "creeping magnet" serves well as a representation of Lorentz force eddy current testing. The presented prototype model

that benefits strongly from the simple geometry demonstrates the basic response of the Lorentz force on the presence of an idealized defect.

Obviously the analytical model suffers from the assumptions and simplifications. The most dominant simplification has been the neglected field decay within the pipe wall which has led to big differences between experiment and analytical solution. Nevertheless, the mathematical model suits well for a low-cost computation of falling time. For different velocity regimes and defect sizes, the narrow defect approximation, the large defect approximation and the complete solution have been demonstrated.

Since the presented Lorentz force eddy current testing problem is crossing different R_m-regimes and geometrical changes have to be taken into account when defects are considered, the application of a 3D transient model is necessary [9, 72]. It has been shown that using time measurement it is possible to distinguish whether there is a defect in the pipe under test or not. Since the cause of the falling time change is a force perturbation, the conclusion is drawn that using force or velocity measurements and appropriate data processing techniques, defects can be localized and identified with higher precision.

The computed falling time differences due to the velocity perturbation caused by exactly one ideal defect have been validated experimentally. Moreover, the linear dependency between falling time difference and the defect size has been proven. As a result, the time measurement in the creeping-magnet problem represents a straight forward inverse problem that can be solved to detect and localize defects.

7.1.2 Measurement Setup

The basic principle of Lorentz force eddy current testing requires a relative motion between the electrically conducting specimen and a permanent magnet which serves as the source of the DC magnetic field. A belt-driven drive is moving the specimen below the magnet with a

controlled velocity of 50 . . . 3750 mm/s. The position of the magnet in the y-z-plane (lateral position and lift-off distance) can be precisely adjusted with a microscopic table.

While the specimen is moving, a 3D force sensor is measuring the three components of the Lorentz force exerting on the magnet with a sampling rate of 10 kHz in real time mode in order to determine the dynamic limitations of the measurement technique. The measurement run has been automated and can serve to scan the specimen which helps to provide necessary data for the forward problem in defect detection.

7.1.3 Signal Quality and Filtering

The signal quality of the measured voltage, which is a measure for the acting force, is a crucial parameter of the Lorentz force eddy current testing. The presence of defects within the specimen leads to perturbations of the eddy current distribution and hence, to perturbations in force. Due to the fact that these perturbations depend strongly on defect size and position within the specimen a high resolution of the measured force signal is preferable. Obviously, the construction of the measurement setup should avoid sources of interference. In order to smooth the measured signal, appropriate filters have to be applied. In the case of many sources of interference, several filters for several frequencies are necessary which reduce the dynamics of the filtered signal.

Reducing mass and increasing the stiffness of the assembly parts increase the first natural frequency of every single part and thus, the motion is no longer forcing amplified natural oscillations. Reducing the number of parts results in a system with a smaller number of degrees of freedom. For the remaining white noise, which is the Gaussian distributed oscillation around a mean value, wavelet filters can be applied to satisfy the need of a high dynamic filter algorithm and a smooth signal.

7.1.4 Methodology

Whenever a new measurement technique is invented, the proof of concept is of eminent importance. In the thesis at hand, the functionality of the measurement setup has been verified with past work, done while investigating magnetic levitation [28, 61, 62]. This work has been available but not designed for this particular purpose. The verification is performed using solid state bars made of two different materials, i. e. aluminum and copper.

Since the detection of defects is the main application of Lorentz force eddy current testing a metal sheet package has been considered. This gives the possibility to vary the depth of different artificial defects within a bar approximation. The measured force components have been compared with these obtained from a metal sheet package without artificial defects.

In order to provide validation experiments and to distinguish differences between the metal sheet package response and the solid bar, validation bars with slit defects and filled bore holes have been considered.

The measurements have been performed at different lateral positions of the magnet to satisfy the need for data for the forward problem of defect reconstruction. Each measurement is summarized in at least two plots in the x-y-plane (F_z/F_x, F_y) where the color of the graph indicates the force magnitude.

7.1.5 Experimental Verification

The experimental results with the solid bars are as expected. While the drag force is rising linearly with increasing velocity the lift force is depending quadratically on the velocity. Especially in the low velocity range of up to 1 m/s, this behavior can be observed. For higher velocities, i. e. higher magnetic Reynolds numbers R_m, the magnetic field is expelled from the conductor due to the motional skin effect which

results in a weaker growth of the force. The high R_m-range, where the drag force is dropping with rising velocity, could not be reached with the current measurement setup.

The variation of the lift-off distance reveals the strong influence of this parameter on the measured force. An increasing lift-off distance leads to lower forces due to the magnetic field attenuation. So, the sensitivity to lift-off changes is the bigger the smaller the lift-off distance is. Consequently, the surface conditions of the specimen influence the force measurement while the lift-off distance is small enough.

Both, the lift and the drag force can be summarized in the lift-to-drag ratio which is linearly dependent on the velocity for a higher range of velocities than the drag force and weakly dependent on the lift-off distance. Evaluating the lift-to-drag ratio provides more stable measurements for undefined surface conditions and velocity deviations than the single force components. Additionally, it is less dependent on the used permanent magnet, i. e. the magnetic field strength.

The force component in lateral direction serves as a measure of alignment quality of the permanent magnet. Without any defect the lateral force is zero in the specimen's line of symmetry. The relative position to the symmetry line can be determined by evaluating the sign of the lateral force due to the fact that there is point symmetry with respect to the origin of the coordinate system. This is a difference to the lift and drag force which are axis symmetric.

7.1.6 Nondestructive Testing

Different artificial defects have been introduced into solid bars and the metal sheet package. The depth has been varied until the force perturbation reached the order of magnitude of the noise. The defect with a size of $L \times W = 10 \times 2\,\mathrm{mm}^2$ has been detected in a depth of 6 mm, while moving with a velocity of 500 mm/s. This result proofs the capability of Lorentz force eddy current testing to detect deep lying

defects in conductors. Depending on the orientation and the size of the defect the detection depth varies.

It has been shown that scanning the specimen leads to a visualization of the force perturbations that can be recognized even by an untrained eye which is important for the applicability of a new testing technique. The lift-to-drag ratio suits the defect detection and the lateral force component serves as an additional information for the localization and reconstruction of the defect (which has not been part of this work).

Nevertheless, there is a lot of work open in order to improve the nondestructive testing technique. Especially the depth of detection can be increased and the dynamics of the system have to be improved. These measures would enable the detection of even smaller defects in greater depth.

7.1.7 Nondestructive Evaluation of Electrical Conductivity

The proposed technique called Lorentz force sigmometry is able to provide the electrical conductivity of a specimen. In a nutshell, Lorentz force sigmometry has the following advantages: (i) it is contactless, (ii) it can be applied continuously during production processes, (iii) it is a method that enables the user to measure conductivity beyond the surface and (iv) the proposed data processing makes the nondestructive evaluation technique resistant to changes in lift-off distance, velocity and strength of the magnetic field source. Lorentz force sigmometry is suitable for specimen of any kind of physical condition. The only limitation is given by the minimal measurable Lorentz force components of the multi-component force sensor.

Due to the fact that LoFoS is a contactless method for conductivity measurements it can be implemented in the production process of any nonmagnetic material (e. g. aluminum, brass). It is possible to mea-

sure the conductivity of hot or aggressive materials. Due to the use of DC magnetic fields LoFoS is not limited by source frequencies like conventional eddy current based techniques. The eddy currents during test are distributed into greater depths than while applying classical eddy current methods which are usually limited to the order of a few micrometers. An additional feature is the easy combination of Lorentz force sigmometry with Lorentz force eddy current testing using the same measurement setup. The conductivity is directly traceable to SI units if the measurement has been calibrated appropriately.

7.2 Outlook: Going Into Deep

One of the goals while investigating Lorentz force eddy current testing has been to overcome the frequency dependent skin depth limitation. It has been shown that with the present measurement setup it is possible to detect defects in a depth of up to 6 mm without any optimization. The limitations of the measurement technique have been discussed and some further work is mentioned that might lead to significant improvements.

7.2.1 Absolute Force Sensor

The applied force sensor is of eminent importance for the Lorentz force eddy current testing. High dynamics, high resolution and a relatively big measurement range are needed for the detection of small and deep lying defects with an absolute force sensor. Since force sensors based on strain gauge technology suffer from their low dynamics and low resolution, they are not the best choice. Investigations on other sensor types should be performed. Especially advances in optical displacement mea-

surements increase the capabilities of deformation bodies with higher stiffness resulting in higher dynamics.

Piezo-electric sensors provide high dynamics and a very high resolution for high forces. Developments in the area of low force sensors (Newton-range) are highly appreciated for Lorentz force eddy current testing. The long-term stability of measured values which is usually a problem of this sensor type, causes no troubles for Lorentz force eddy current testing since the focus is on the detection of perturbations in the force signal.

7.2.2 Differential Force Sensor

A common way of detecting perturbations only is the use of differential sensors. Due to the fact that force cannot be measured directly, a differential effect of the force, e. g. acceleration instead of displacement, can be measured. Acceleration sensors provide high dynamics but are restricted to gravitational acceleration and cannot provide extremely high resolution. Despite of the limitations the acceleration of the permanent magnet should be measurable even on stiff deformation bodies.

Another way to construct a differential sensor is purely electrically. Based on the induction law, a transient change in the magnetic flux induces a voltage in a coil. This technique has been successfully applied to the remote field by [59]. This technique can be applied to the secondary magnetic field and it can be picked up directly at the permanent magnet. The advantage of this technique would be that the measurement instruments for voltage provide excellent dynamics and resolution at low voltages which are expected [9]. Thus, this sensor type would not be a differential force sensor but a differential magnetic field sensor. A further advantage is the capability of examining ferromagnetic materials because no deformation body would be needed which

could be damaged by the high attraction force at low lift-off distances. So, a vast field of applications can be offered.

7.2.3 Comparison with the Classical Approach

In the interests of completeness, a fair comparison with the classical eddy current testing has to be provided. Therefore, comparable measurement conditions have to be considered. The application while the specimen is moving relatively to the nondestructive testing sensor is necessary and appreciated by industry [17]. Due to the fact that the influencing parameters (not counting the source frequency for classical eddy current testing) can be reduced to four under laboratory conditions (lateral position, lift-off distance, velocity, magnetic field), it is rather simple to control them and compare results for several measurement sets with different defects at different depths. Only this comparison can reveal the advantages and disadvantages of both techniques.

Anyway, Lorentz force eddy current testing shall not be understood as an advantageous method in comparison with the classical eddy current testing but as an alternative. It might suit better to several problems which are difficult to address with the classical eddy current testing method.

Bibliography

[1] G. Linß, *Qualitätsmanagement für Ingenieure*. Fachbuchverlag Leipzig, 2005.

[2] NTSB/AAR-89/03, "Aircraft Accident Report–Aloha Airlines, Flight 243, Boeing 737-200, N73711, near Maui, Hawaii, April 28, 1988," National Transportation Safety Board Bureau of Accident Investigation Washington, D.C. 20594, Tech. Rep., 1989. [Online]. Available: http://www.aerohabitat.eu/uploads/media/04-28-88_Aloha_Airlines_01.pdf

[3] A. Dey, H.-M. Thomas, and R. Pohl, "The Important Role Of Eddy Current Testing In Railway Track Maintenance," in *17th World Conference on Nondestructive Testing*, 2008.

[4] T. Aastroem, "From Fifteen To Two Hundred NDT-Methods In Fifty Years," in *17th World Conference on Nondestructive Testing*, 2008.

[5] L. Guohou, H. Pingjie, C. Peihua, H. Dibo, Z. Guangxin, and Z. Zekui, "Application Of Multi-sensor Data Fusion In Defects Evaluation Based On Dempster-Shafer Theory," in *IEEE Instrumentation and Measurement Technology Conference (I2MTC)*, 2011.

[6] M. Kröning, J. Ribeiro, and A. Vidal, "Progress In NDT System Engineering Through Sensor Physics And Integrated Efficient Computing," in *17th World Conference on Nondestructive Testing*, 2008.

[7] "NTB elektronische Geräte GmbH," e-mail: ntb@ntbxray.com. [Online]. Available: http://www.ntbxray.com

[8] H. Brauer and M. Ziolkowski, "Eddy Current Testing of Metallic Sheets with Defects Using Force Measurements," *Serbian Journal of Electrical Engineering*, vol. 5, no. 1, pp. 11–20, 2008.

[9] M. Zec, "Theory and Numerical Modelling of Lorentz Force Eddy Current Testing," Ph.D. dissertation, Ilmenau University of Technology, 2013.

[10] X. Ma, "Electromagnetic NDT and Condition Monitoring - A Personal View," in *Proc. of the 17th International Conference on Automation & Computing*, 2011.

[11] D. C. Jiles, "Review Of Magnetic Methods For Nondestructive Evaluation," *NDT Int.*, vol. 21, no. 5, pp. 311 – 319, 1988.

[12] J. Achenbach, "Quantitative Nondestructive Evaluation," *Int. J. Solids Struct.*, vol. 37, no. 1 – 2, pp. 13 – 27, 2000.

[13] C. J. Hellier, *Handbook Of Nondestructive Evaluation.* McGraw-Hill, 2003.

[14] L. Bettaieb, H. Kokabi, M. Poloujadoff, A. Sentz, and C. Tcharkhtchi, "Fatigue and/or Crack Detection In NDE," *Nondestruct. Test. Eva.*, vol. 25, no. 1, pp. 13 – 24, 2010.

[15] W. Shih and G. Fitzpatrick, "Magneto-Optic Imaging Technology: A New Tool for Aircraft Inspection," *AMPTIAC Newsletter*, vol. 6, no. 3, pp. 17 – 22, 2002. [Online]. Available: http://ammtiac.alionscience.com/pdf/AMPQ6_3ART03.pdf

[16] S. Steeb, *Zerstörungsfreie Werkstück- und Werkstoffprüfung*, W. J. Bartz, H.-J. Mesenholl, and E. Wippler, Eds. expert verlag, 2011.

[17] A. Stüber, M. Waltner, B. Bäcker, H. Jung, H. Schifferl, and I. Steller, "Non-Destructive Testing of Steel Long Products - Current Status (GER)," *Eisen und Stahl*, vol. 131, pp. 73 – 82, 2011.

[18] R. Grimberg, A. Savin, R. Steigmann, A. Bruma, and P. Barsanescu, "Ultrasound And Eddy Current Data Fusion For Evaluation Of Carbon-epoxy Composite Delaminations," *Insight*, vol. 51, no. 1, pp. 25 – 32, 2009.

[19] F. Foucher and S. Lonné, "Modelling NDT for Aircraft industries..." *Cedrat News: Flux Solutions & Mechatronics Products*, vol. 56, pp. 8 – 9, 2008.

[20] V. A. Klimanov, M. Kröning, P. Kröning, F. Mohr, K. M. Reddy, and H. Wolf, "NDT Controlled Production in Steel Industry," in *NDESAI*, 2011.

[21] R. Amineh, N. Nikolova, J. Reilly, and J. Hare, "Characterization of Surface-Breaking Cracks Using One Tangential Component of Magnetic Leakage Field Measurements," *IEEE T. Magn.*, vol. 44, pp. 516 – 524, 2008.

[22] "Institut Dr. Foerster GmbH & Co. KG," e-mail: info@foerstergroup.de. [Online]. Available: http://www.foerstergroup.de

[23] G. Sposito, C. Ward, P. Cawley, P. Nagy, and C. Scruby, "A Review Of Non-destructive Techniques For The Detection Of Creep Damage In Power Plant Steels," *NDT&E Int.*, vol. 43, pp. 555 – 567, 2010.

[24] D. C. Jiles, "Review Of Magnetic Methods For Nondestructive Evaluation (Part 2)," *NDT Int.*, vol. 23, no. 2, pp. 83 – 92, 1990.

[25] D. Hughes, "V. Induction-Balance And Experimental Researches Therewith," *Philosophical Magazine Series 5*, vol. 8, no. 46, pp. 50–56, 1879. [Online]. Available: http://www.tandfonline.com/doi/abs/10.1080/14786447908639649

[26] R. Grimberg, "Electromagnetic Nondestructive Evaluation: Present and Future," *Strojniški vestnik - Journal of Mechanical Engineering*, vol. 57, pp. 204 – 217, 2011.

[27] B. A. Auld and J. C. Moulder, "Review of Advances in Quantitative Eddy Current Nondestructive Evaluation," *J. Nondestruct. Eval.*, vol. 18, no. 1, pp. 3 – 36, 1999.

[28] S.-W. Lee and R. C. Menendez, "Force on Current Coils Moving over a Conducting Sheet with Application to Magnetic Levitation," *Proc. of the IEEE*, vol. 62, no. 5, pp. 567–577, 1974.

[29] A. Savin, R. Grimberg, and O. Mihalache, "Analytical Solutions Describing The Operation Of A Rotating Magnetic Field Transducer," *IEEE T. Magn.*, vol. 33, no. 1, pp. 697 –702, jan 1997.

[30] G. Daalmanns and M. Steck, "Device For Detecting Deep Defects In Electrically Conductive Materials In A Non-destructive Manner," European Patent EP 1 723 409 B1, 2006.

[31] M. v. Kreutzbruck, K. Allweins, and C. Heiden, "Fluxgate-Magnetometer For Detection Of Deep Lying Defects," in *15^{th} World Conference on Nondestructive Testing*, 2000.

[32] G. Mook, O. Hesse, and V. Uchanin, "Deep Penetrating Eddy Currents and Probes," in *9^{th} European Conference on Nondestructive Testing*, 2006.

[33] J. Kawano, S. A. T. Hato, Y. Oshikubo, A. Tsukamoto, and K. Tanabe, "Non-Destructive Evaluation of Deep-Lying Defects in Multilayer Conductors Using HTS SQUID Gradiometer," *IEEE T. Appl. Supercon.*, vol. 21, no. 3, pp. 428 – 431, 2011.

[34] A. Yashan, W. Bisle, and T. Meier, "Inspection of Hidden Defects in Metal-Metal Joints of Aircraft Structures Using Eddy Current Technique with GMR Sensor Array," in *9^{th} European Conference on Nondestructive Testing*, 2006.

[35] S. Udpa and L. Udpa, "Eddy Current Testing - Are we at the Limits?" in *16^{th} World Conference on Nondestructive Testing*, 2004. [Online]. Available: http://www.ndt.net/article/wcndt2004/pdf/eddy_current/776_udpa.pdf

[36] G. Betta, L. Ferrigno, and M. Laracca, "GMR-Based ECT Instrument For Detection and Characterization of Crack on a Pla-

nar Specimen: A Hand-Held Solution," *IEEE T. Instrum. Meas.*, vol. 61, no. 2, pp. 505 – 512, 2012.

[37] T. Chady, P. Baniukiewicz, and R. Sikora, "Analysis of Complex Differential Eddy Current Transducer For Deep Flaws Evaluation," *Nondestruct. Test. Eva.*, vol. 24, no. 1-2, pp. 61 – 68, 2009.

[38] P. Xu, S. Huang, and W. Zhao, "A New Differential Eddy Current Testing Sensor Used For Detecting Crack Extension Direction," *NDT&E Int.*, vol. 44, pp. 339 – 343, 2011.

[39] L. Janousek, Z. Chen, N. Yusa, and K. Miya, "Excitation With Phase Shifted Fields-Enhancing Evaluation Of Deep Cracks In Eddy-Current Testing," *NDT&E Int.*, vol. 38, pp. 508 – 515, 2005.

[40] Y. He, M. Pan, F. Luo, and G. Tian, "Pulsed Eddy Current Imaging And Frequency Spectrum Analysis For Hidden Defect Nondestructive Testing And Evaluation," *NDT&E Int.*, vol. 44, pp. 344 – 352, 2011.

[41] T. P. Sattar and A. Brenner, "Robotic System For Inspection Of Test Objects With Unknown Geometry Using NDT Methods," *Industrial Robot: An International Journal*, vol. 36, no. 4, pp. 340 –343, 2009.

[42] L. Cheng and G. Y. Tian, "Comparison of Nondestructive Testing Methods on Detection of Delaminations in Composites," *Journal of Sensors*, vol. 2012, pp. 1 – 7, 2012.

[43] W. D. Feist, G. Mook, J. H. Hinken, J. Simonin, and H. Wrobel, "Electromagnetic Detection and Characterization of Tungsten Carbide Inclusions in Non-Ferromagnetic Alloys," *Advanced Engineering Materials*, vol. 7, no. 9, pp. 841–846, 2005.

[44] S. Rajesh, L. Udpa, and S. Udpa, "Numerical Model Based Approach For Estimating Probability Of Detection In NDE Appli-

cations," *IEEE T. Magn.*, vol. 29, no. 2, pp. 1857 –1860, mar 1993.

[45] D. L. Atherton, "Remote Field Eddy Current Inspection," *IEEE T. Magn.*, vol. 31, no. 6, pp. 4142 – 4147, 1995.

[46] Y. Sun, W. Lord, and G. Katragadda, "Motion Induced Remote Field Eddy Current Effect in a Magnetostatic Non-Destructive Testing Tool: A Finite Element Prediction," *IEEE T. Magn.*, vol. 30, pp. 3304 – 3307, 1994.

[47] Y. Sun, "Electromagnetic-Field-Focusing Remote-Field Eddy-Current Probe System and Method for Inspecting Anomalies in Conducting Plates," U.S. Patent US 6,002,251, 1999.

[48] Y. Sun and T. Ouyang, "Detection Of Cracks In Multi-Layer Aircraft Structures With Fasteners Using Remote Field Eddy Current Testing Method," Innovative Materials Testing Technologies, Inc., Tech. Rep., 2000.

[49] Y. Sun, T. Ouyang, and S. Udpa, "Multi-Layer Aircraft Structure Inspection Using Super-Sensitive Remote-field Eddy-current System," *AIP Conf. Proc.*, vol. 557, pp. 1906 – 1913, 2001.

[50] G. Mook, F. Michel, and J. Simonin, "Wirbelstrom-Sensorarrays," in *DGZfP-Jahrestagung*, 2009.

[51] G. Mook, F. Michel, and J. Simonin, "Electromagnetic Imaging Using Probe Arrays," *Strojniški vestnik - Journal of Mechanical Engineering*, vol. 3, pp. 227–236, 2011.

[52] M. K. Lim and H. Cao, "Combining Multiple NDT Methods To Improve Testing Effectiveness," *Constr. Build. Mater.*, vol. -, pp. 1 – 6, 2011.

[53] T. Heckel, H.-M. Thomas, M. Kreutzbruck, and S. Rühe, "High Speed Non-Destructive Rail Testing With Advanced Ultrasound And Eddy Current Testing Techniques," in *Proc. of the National*

Seminar & Exhibition on Non-Destructive Testing (NDE 2009), 2009, pp. 261 – 265.

[54] Z. Song, T. Yamada, H. Shitara, and Y. Takemura, "Detection of Damage and Crack in Railhead by Using Eddy Current Testing," *Journal of Electromagnetic Analysis and Applications*, vol. 3, pp. 546 – 550, 2011.

[55] M. Cervantes, C. Enström, H. Kelvesjö, and W. Ohlsson, "Method and Device for Measuring a Parameter of a Metal Bed," World Patent WO 00/58 695, 1999.

[56] I. J. Garshelis, S. P. L. Tollens, R. J. Kari, L. P. Vandenbossche, and L. R. Dupre, "Drag Force Measurement: A Means For Determining Hysteresis Loss," *J. Appl. Phys.*, vol. 99, no. 8, pp. 08D910–1 – 08D910–3, 2006.

[57] R. P. Uhlig, M. Zec, M. Ziolkowski, H. Brauer, and A. Thess, "Lorentz Force Sigmometry: A Contactless Method for Electrical Conductivity Measurements," *J. Appl. Phys.*, vol. 111, no. 9, pp. 094 914–1 – 094 914–7, 2012.

[58] S. Yang, Y. Sun, L. Udpa, S. S. Udpa, and W. Lord, "3D Simulation of Velocity Induced Fields for Nondestructive Evaluation Application," *IEEE T. Magn.*, vol. 35, no. 3, pp. 1754 – 1756, 1999.

[59] Y. Sun, S. Udpa, W. Lord, L. Udpa, and T. Ouyang, "Application Of Motion Induced Remote-field Eddy Current Effect To Online Inspection And Quality Examination Of Rolling Metallic Strips," *AIP Conf. Proc.*, vol. 557, pp. 1541 – 1548, 2001.

[60] H.-W. Lee, K.-C. Kim, and J. Lee, "Review of Maglev Train Technologies," *IEEE T. Magn.*, vol. 42, no. 7, pp. 1917 – 1925, 2006.

[61] J. R. Reitz, "Forces on Moving Magnets due to Eddy Currents," *J. Appl. Phys.*, vol. 41, no. 5, pp. 2067–2071, 1970.

[62] J. R. Reitz and L. C. Davis, "Force on a Rectangular Coil Moving above a Conducting Slab," *J. Appl. Phys.*, vol. 43, no. 4, pp. 1547–1553, 1972.

[63] J. Bennett, T. Gora, P. J. Kemmey, and W. J. Kolkert, "Electromagnetic Braking of a Metallic Projectile in Flight," *IEEE T. Magn.*, vol. Mag-21, no. 3, pp. 1250–1253, 1985.

[64] I. J. Garshelis and S. P. I. Tollens, "Non-Destructive Evaluation Via Measurement of Magnetic Drag-Force," World Patent WO 2007/053 519 A2, 2007.

[65] L. Vandenbossche, I. Garshelis, S. Tollens, L. Dupre, and P. Sergeant, "Magnetic Nondestructive Evaluation of Bending Fatigue Damage Using the Drag Force Method," *IEEE T. Magn.*, vol. 43, no. 6, pp. 2746 –2748, June 2007.

[66] I. J. Garshelis, S. P. L. Tollens, M. E. Hollander, R. J. Kari, and J. M. Cuseo, "Assessment Of Shot Peening Uniformity By Magnetic Drag Force Measurements," *J. Appl. Phys.*, vol. 105, no. 7, pp. 07E711 –07E711–3, 2009.

[67] P. Sergeant, L. Dupre, L. Vandenbossche, I. Garshelis, and S. Tollens, "Numerical Model for the Drag Force Method to Evaluate Hysteresis Loss," *IEEE T. Magn.*, vol. 44, no. 6, pp. 842 –845, 2008.

[68] B. Petkovič, J. Haueisen, M. Zec, R. P. Uhlig, H. Brauer, and M. Ziolkowski, "An Approximation Method for Crack Reconstruction in Lorentz Force Eddy Current Testing," in *XII-th International Workshop on Optimization and Inverse Problems in Electromagnetism (OIPE)*, 2012.

[69] M. Kirpo, S. Tympel, T. Boeck, D. Krasnov, and A. Thess, "Electromagnetic Drag On A Magnetic Dipole Near A Translating Conducting Bar," *J. Appl. Phys.*, vol. 109, no. 11, pp. 113 921–1–113 921–11, 2011.

[70] R. P. Uhlig, M. Zec, M. Ziolkowski, and H. Brauer, "Lorentz Force Eddy Current Testing: Validation of Numerical Results," in *Proceedings of Electrotechnical Institute*, vol. 251, 2011. [Online]. Available: http://bambus.iel.waw.pl/pliki/ogolne/prace%20IEL/251/12.pdf

[71] M. Zec, R. P. Uhlig, M. Ziolkowski, and H. Brauer, "Lorentz Force Eddy Current Testing: Two-Dimensional Numerical Study," in *Proceedings of Electrotechnical Institute*, vol. 252, 2011. [Online]. Available: http://bambus.iel.waw.pl/pliki/ogolne/prace%20IEL/252/04.pdf

[72] M. Zec, R. P. Uhlig, M. Ziolkowski, and H. Brauer, "Finite Element Analysis of Eddy Current Problems with Moving Parts," *IEEE T. Magn.*, 2012, accepted for publication.

[73] A. Thess, E. V. Votyakov, and Y. Kolesnikov, "Lorentz Force Velocimetry," *Phys. Rev. Lett.*, vol. 96, no. 16, pp. 164 501–1–164 501–4, 2006.

[74] A. Thess, E. V. Votyakov, B. Knaepen, and O. Zikanov, "Theory Of The Lorentz Force Flowmeter," *New. J. Phys.*, vol. 9, p. 299, 2007.

[75] A. Wegfrass, C. Diethold, M. Werner, T. Fröhlich, B. Halbedel, F. Hilbrunner, C. Resagk, and A. Thess, "A Universal Noncontact Flowmeter For Liquids," *Appl. Phys. Lett.*, vol. 100, no. 19, p. 194103, 2012.

[76] R. P. Uhlig, M. Zec, H. Brauer, and A. Thess, "Lorentz Force Eddy Current Testing: a Prototype Model," *J. Nondestruct. Eval.*, vol. 31, no. 4, pp. 357–372, 2012.

[77] N. Derby and S. Olbert, "Cylindrical Magnets And Ideal Solenoids," *Am. J. Phys.*, vol. 78, no. 3, pp. 229–235, 2010.

[78] D. Amrani and P. Paradis, "Faraday's Law Of Induction Gets Free-falling Magnet Treatment," *Phys. Educ.*, vol. 40, no. 4, pp. 313–314, 2005.

[79] K. D. Hahn, E. Johnson, A. Brokken, and S. Baldwin, "Eddy Current Damping Of A Magnet Moving Through A Pipe," *Am. J. Phys.*, vol. 66, no. 12, pp. 1066–1076, 1998.

[80] J. A. M. Clack and T. P. Toepker, "Magnetic Induction Experiment," *Phys. Teach.*, vol. 28, no. 4, pp. 236–238, 1990.

[81] D. J. Griffiths, *Introduction to Electrodynamics*. Pearson, 2008.

[82] Y. Levin, F. L. de Silveira, and F. Rizzato, "Electromagnetic Braking: A Simple Quantitative Model," *Am. J. Phys.*, vol. 74, no. 9, pp. 815–817, 2006.

[83] J. D. Jackson, *Classical Electrodynamics*. Cambridge University Press, 1998.

[84] I. Newton, *Philosophiae naturalis principia mathematica*. Harvard University Press, 1687.

[85] H. K. Khalil, *Nonlinear Systems*, 2nd ed. Upper Saddle River, NJ: Prentice Hall, 1996.

[86] BIPM, Ed., *Evaluation Of Measurement Data - Guide To The Expression Of Uncertainty In Measurement*. Joint Committee for Guides in Metrology, 2008. [Online]. Available: http://www.bipm.org/utils/common/documents/jcgm/JCGM_100_2008_E.pdf

[87] P. A. Davidson, *An Introduction to Magnetohydrodynamics*. Cambridge University Press, 2001.

[88] U. Christensen and A. Tilgner, "Der Geodynamo," *Physik Journal*, vol. 1, no. 10, pp. 41 – 47, 2002.

[89] M. Assing, "Konstruktive Überarbeitung, Aufbau und Test eines Lorentzkraft-Wirbelstrom-Messplatzes," Master's thesis, Ilmenau University of Technology, 2012.

[90] A. Schöne, *Meßtechnik*. Springer, 1997.

[91] P. Profos and T. Pfeifer, Eds., *Grundlagen der Meßtechnik*. Oldenbourg Verlag München Wien, 1997.

[92] *Mehrachsen-Kraftsensor K3D40*. [Online]. Available: http://www.me-systeme.de/de/datasheets/k3d40.pdf

[93] H. Nyquist, "Certain Topics in Telegraph Transmission Theory," *Proc. of the IEEE*, vol. 90, no. 2, pp. 280 – 305, 2002.

[94] C. E. Shannon, "Communication in the Presence of Noise," *Proc. of the IEEE*, vol. 86, no. 2, pp. 447 – 457, 1998.

[95] P. Murrell, *Introduction to Data Technologies*. Chapman and Hall/CRC, 2009. [Online]. Available: http://www.stat.auckland.ac.nz/~paul/ItDT/itdt-2008-09-29.pdf

[96] H. Inoue, "Force Feedback in Precise Assembly Tasks," Massachusetts Institute of Technology, Artificial Intelligence Laboratory, Tech. Rep., 1974.

[97] S. Mallat, *A Wavelet Tour of Signal Processing - The Sparse Way*. Elsevier, 2009.

[98] F. Harris, "On The Use Of Windows For Harmonic Analysis With The Discrete Fourier Transform," *Proc. of the IEEE*, vol. 66, no. 1, pp. 51 – 83, 1978.

[99] I. Daubechies, "The Wavelet Transform, Time-Frequency Localization and Signal Analysis," *IEEE T. Inform. Theory*, vol. 36, pp. 961 – 1005, 1990.

[100] H. Dresig and F. Holzweißig, *Maschinendynamik*. Springer-Verlag, 2009.

[101] R. Jürgler, *Maschinendynamik*. Springer-Verlag, 2004.

[102] L. Frýba, *Vibration of Solids and Structures under Moving Loads*. Thomas Telford, 1972.

[103] S. G. Kelly, *Fundamentals Of Mechanical Vibrations*. McGraw-Hill, 2000.

[104] P. L. Gatti and V. Ferrari, *Applied Structural And Mechanical Vibrations*. E & FN Spon, 1999.

[105] L. Yang, X. Zhao, F. Hui, and X. Shi, "An Improved Wavelet Filtering Algorithm and Its FPGA Implementation," *International Journal of Information Technology and Computer Science*, vol. 2, pp. 17 – 24, 2010.

[106] S. Niikura and A. Kameari, "Analysis Of Eddy Current And Force In Conductors With Motion," *IEEE T. Magn.*, vol. 28, no. 2, pp. 1450 – 1453, 1992.

[107] T. Takahashi and K. Kurita, "Computation Of Eddy Currents Induced In A Conducting Sheet Under Moving Magnets," *IEEE T. Magn.*, vol. 24, no. 1, pp. 197 – 200, 1988.

[108] *SIGMATEST® 2.069*. [Online]. Available: http://www.mp-ndt.de/EN/sales/sigmatest2.069_electrical_conductivity_measurement.pdf

[109] R. P. Uhlig, M. Zec, and H. Brauer, "Lorentz Force Eddy Current Testing: Force Dependency In Respect To The Lift-Off Distance - Computation & Validation," in *IET 8th International Conference on Computation in Electromagnetics (CEM 2011)*, 2011.

[110] H. de Gersem, "Spectral-Element Method For High-Speed Rotating Cylinders," *COMPEL - The International Journal for Computation and Mathematics in Electrical and Electronic Engineering*, vol. 28, no. 3, pp. 730 – 740, 2009.

[111] L. J. van der Pauw, "A Method of Measuring Specific Resistivity and Hall Effect of Discs of Arbitrary Shape," *Philips Research Reports*, vol. 13, no. 1, pp. 1–9, 1958.

[112] J. A. Delaney and A. B. Pippard, "Electrodeless Methods for Conductivity Measurement in Metals," *Rep. Prog. Phys.*, vol. 35, no. 2, pp. 677–715, 1972.

[113] R. P. Suvarna, K. R. Rao, and K. Subbarangaiah, "A Simple Technique for A.C. Conductivity Measurements," *Bull. Mater. Sci.*, vol. 25, no. 7, pp. 647–651, 2002.